Synthesis and Modeling of Poly(L-lysine) Based Biomaterials for Regenerative Medicine

by

Mohamed Farag A. Eldessouki

A dissertation submitted to the Graduate Faculty of
Auburn University
in partial fulfillment of the
requirements for the Degree of
Doctor of Philosophy

Auburn, Alabama
May 9, 2011

Keywords: Biomaterials, Scaffolds, Tissue Engineering, Nanocomposite, Branched and Crosslinked Polymers, Molecular Modeling

Approved by

Yasser Gowayed, Chair, Professor of Polymer and Fiber Engineering
Gisela Buschle-Diller, Professor of Polymer and Fiber Engineering
Peter Schwartz, Department Head of Polymer and Fiber Engineering
Orlando Acevedo, Assistant Professor of Chemistry and Biochemistry

Abstract

The need for tissue engineered scaffolds is growing due to the shortage in organ donation, the immunoreactions to allotransplants, and the high cost associated with transplantation. This work focuses on the material selection and processing which are keys for a successful design of any tissue engineered structure. Poly(L-lysine) (PLL) was selected in this work as a base for developing scaffolds due to its biocombatability and bioabsorbability. PLL, on the other hand, has limitations in use due to its hydrophilicity that weakens its structures in aqueous and physiological conditions. To overcome these limitations, two hypotheses are suggested in this dissertation; the first hypothesis is that a micro-scale composite of PLL with a high crystalline material can enhance the final properties of PLL. The second hypothesis is that the properties of PLL structures can be controlled by forming a molecular-scale composite with another crosslinked bioresorbable polymer.

To attest these hypotheses, nanocomposite materials from PLL and microcrystalline cellulose (MCC) were produced and processed in different ways. Also, molecular-scale composites of PLL and networked structure of poly(L-lactide) (PLA) were produced. The experimental results for the synthesized PLA were then compared to the data obtained from molecular modeling techniques.

Results of PLL with MCC show intimate composite structures with attractive electrostatic forces between the components. Processing condition of PLL was found to affect its secondary structure with α-helix secondary structure for samples prepared at pH 7. Inclusion of

hydrolyzed MCC particles resulted in increasing the crystallinity of the semi-crystalline PLL which enhanced the swelling properties of the produced scaffolds.

To produce branched PLA, a novel solution-based ring opening polymerization method was introduced and the properties of the produced polymers were studied. Thermal properties of PLA indicated a double melting behavior which was shown to be a result of the concurrence of crystallization and melting of the polymer chains. Chemical neutralization of PLL salt was able to dissolve PLL in organic solvent where the branched PLA was crosslinked.

The structure and energy of lactide were predicted using electronic modeling techniques and results matched to a reasonable extent the experimental values obtained from X-ray single crystallography. The path of the ring opening polymerization (ROP) of PLA was modeled and its activation energy was calculated. Molecular dynamic (MD) simulation was able to predict the glass transition temperature of PLA with about 3 ˚C margin of error.

Acknowledgments

I thank Allah, the Almighty God, for His guidance and the path He has led me on. Allah's words in the Quran were inspiring and encouraged me to continuously seek knowledge.

Although my name is written on the cover of this dissertation, the material inside represents a distillation of the scientific literature in the broad field of polymer engineering. Hence, acknowledgement goes first to those people whose ideas and results were the topics of investigation in this work. This work might not be possible without the collaboration and the support I received from many people around me. Among those, I would like to thank:

- My advisor, Dr. Yasser Gowayed, for his continuous support. His door was always open to me and he was willing to listen and discuss my work at anytime.
- The members of my advisory committee; Dr. Buschle-Diller, Dr. Shwartz, and Dr. Acevedo, for providing constructive discussions and help all the time.
- My parents for raising me responsibly and my brothers and sister for their support.
- My wife, Mayza Ibrahim, for devoting endless effort taking care of my lovely kids (Gehad, Omar, and Nada) while I was working in the lab.
- The faculty, staff, and my colleague students at the Department of Polymer and Fiber Engineering who were, indeed, my second family.
- The following special people who contributed in some way to this work: Dr. Sherif Hammad, for helping in NMR and chemical synthesis; Dr. Brian Little and Dr. John Gorden for the XRD testing; Dr. Roy Broughton and Dr. Maria Auad, for the productive discussions; Dr. Ramsis Farag, for the fruitful discussions and innovative ideas.

Table of Contents

List of Tables

List of Figures

List of Abbreviations

B3LYP	Beck3-Lee–Yang–Parr functional for exchange-correlation energy
CHARMM	Chemistry at Harvard using Molecular Mechanics
DCM	Dichloromethane
DFT	Density functional theory
DMAP	4-(dimethylamino)pyridine
DMF	Dimethylformamide
DSC	Differential scanning calorimetry
FH	Flory-Huggins thermodynamic model
FTIR	Fourier transform infrared spectroscopy
GPC	Gel permeation chromatography
HDI	Hexamethylene diisocyanate
HF	Hartree-Fock calculations
HMCC	Hydrolyzed microcrystalline cellulose
HMCC-NS	Hydrolyzed microcrystalline cellulose with no sonication (mild-condition hydrolysis)
IRC	Intrinsic reaction coordinate
KS	Kohn-Sham calculations
MCC	Microcrystalline cellulose
MD	Molecular dynamic

NMR	Nuclear magnetic resonance
PDI	Polydispersity index
PES	Potential energy surface
PLA	Poly(L-lactide)
PLC??	Composite of poly(L-lysine) and microcrystalline cellulose with concentration by weight represented in the next numbers (??). For example, PLC15 means a composite of PLL with 15% MCC.
PLHC??	Composite of poly(L-lysine) and hydrolyzed microcrystalline cellulose with concentration by weight represented in the next numbers (??)
PLL	Poly(L-lysine)
RMSE	Root mean square error
ROP	Ring opening polymerization
T_g	Glass transition temperature
TGA	Thermal gravimetric analysis
TIPS	Thermally induced phase separation
TS	Transition structure
WAXD	Wide-angle X-ray diffraction
ZPE	Zero point energy

Chapter I: Introduction

According to the statistics given by the Health Resources and Services Administration, U.S. Department of Health & Human Services, there are about 109,292 patients on the waiting list of organ donation while the number of transplants in the first half of the year 2010 is almost double the donated organs (16,779 vs 8,477 as of 10/22/2010) [1]. These numbers may increase when the matching between the donor and the recipient is considered in terms of how the immune system of the patient may response to the new tissue. Based on these facts, there is a growing research in the field of regenerative medicine, or tissue engineering, to find alternative ways to restore, maintain, or enhance damaged or diseased organs [2].

Scaffold formation is one of the key elements for regenerative medicine where a bioresorbable material is implanted in the body to form a three dimensional template for cell adhesion [3]. Scaffolds also provide the temporal mechanical support needed during cell growth [4]. The ideal scaffold design should integrate the following characteristics [5, 6]: a) A highly porous structure with interconnected pores to allow cell growth and flow transport of nutrients and metabolic waste [7]; b) A biocompatible and bioresorbable material with controlled rates of degradation and resorption to match cell and tissue growth; c) proper surface chemistry for cell attachment, proliferation, and differentiation, and d) mechanical properties to match those of the tissues at the site of implantation.

One of the promising polymeric biomaterials is poly (L-lysine) (PLL) which is a biocompatible polymer since its lysine repeating units are essential building blocks of proteins in

mammals. PLL is bioresorbable and it metabolizes to produce acetyl-coenzyme A which is important in many of the body's biochemical reactions [8]. PLL behaves like a smart material [9] since it is able to change its bulk properties according to the surrounding stimulants such as temperature [10], pH [11-13], incident light [14], and molecular weight [15]. As a polycation under biological conditions [16], PLL can support the negatively charged cells of the body to attach to its surface [17, 18] which makes it a good choice as a scaffold material [19-21].

The cationic surface charge of PLL has special importance and it was utilized in many applications such as self assembling [22-25] and biomaterial coating applications [18] since it allows the development of electrostatic interactions between the primary amines of the polymer and the phosphates in the DNA [26]. For example, the amount of immobilized DNA was found to increase after coating membranes of poly(2-hydroxyethyl methacrylate) (pHEMA) with a layer of PLL [18] that was applied in the therapy of autoimmune diseases involving the removal of anti-DNA antibodies from plasma and led to clinical treatment improvements [27]. PLL is the most widely studied polycation for alginate bead coating used to stabilize and control the molecular weight cut-off of its microcapsule membranes [28]. The modification of the surface of these microcapsules is required to overcome the immunogenic effect of PLL at certain concentrations [29, 30]. PLL was copolymerized with poly(lactic acid) (PLA) that formed an interactive biomaterial to control the cell behavior *in vitro* [31] and provided the sites of ligand grafting by presenting the peptides on the transient surface as the material degrades [19]. For selective cell adhesion, PLL blends and copolymers are modified through the derivatization of arginine - glycine - aspartic acid (RGD) motifs which are ligands for integrin cell adhesion receptors [32].

Although PLL has potential advantages for tissue engineering materials, its application has been limited to surface property enhancements of scaffolds made from other polymers [33-35]. This limitation might be attributed to the relatively weak structure of PLL and its hydrophilic properties that weaken the structure when placed in aqueous environment. Hence, this work aims to investigate the possibility of reinforcing PLL based on the following hypotheses:

- Increasing the crystallinity of the semi-crystalline PLL may lead to an increase in the physical integrity of PLL in aqueous media and restrain its dissolution.
- Introducing a networked structure of another polymer may lead to an enhancement in the PLL properties and may not allow the phase separation to take place between the two polymers.

These hypotheses were studied against a set of produced PLL-based multi-scale composite structures. Microcrystalline cellulose (MCC) was considered as a strong polysaccharide that can form a micro-scale composite with PLL. The system of PLL with MCC was studied and discussed in chapter II. The other composite material was produced from networked structures of poly(L-lactide) (PLA) which is a biocompatible polymer and can be mixed on the molecular-scale with PLL. The system of PLL with PLA was introduced as the topic of chapter III. The experimental results for PLA analysis and PLA ring opening reaction were studied using electronic modeling techniques and a macroscopic property for PLA was studied using molecular dynamic simulation. The molecular modeling of PLA was studied with comparison to experiments in chapter IV of this study.

Chapter II: PLL Micro-Scale Composite with MCC

Abstract

This chapter investigates the possibility of reinforcing a weak polypeptide (poly(L-lysine)) with a stronger polysaccharide (cellulose) and processing the resulting composite into a porous structure. As the main processing parameters, the effect of pH on the secondary structure of the polypeptide and the effect of the hydrolysis conditions on the properties of commercially available microcrystalline cellulose (MCC) were studied. The significance of the cellulose content as well as the scaffold fabrication conditions on the properties of the composite system were assessed. Overall, PLL/MCC composites showed a lower crystallinity compared to the PLL alone while further hydrolyzed MCC particles (HMCC) showed surface erosion and resulted in a crystallinity increase when incorporated into a composite structure.

1. Introduction

Previous attempts to form composite structures based on poly(L-lysine) include reinforcing PLL in a nano-composite form by including nano-clays [11, 36], carbon nano-tubes [37, 38], and bioceramic particles of hydroxyapatite [39]. Systems of polypeptides with cellulose were described in literature [40] where different proteins, including PLL, were used as thin laminating layers for cellulosic paper films to enhance their wet strength because the fibers showed swelling and loss of adhesive contact. The optimum wet strength was achieved in samples with highest contents of lysine and arginine, and for samples that were processed at elevated temperature which provided an opportunity for covalent bond formation between cellulose and peptide. The biocompatibility of cellulose is well-known and microcrystalline cellulose (MCC) particles are inherently fairly stiff and could act as reinforcement for the PLL matrix. A hypothetically perfect crystalline phase of MCC has an estimated modulus of approximately 150 GPa [41].

This research focuses on the possibility of reducing the hydrophilicity of PLL and creating a tissue engineered scaffold with reasonable swelling capabilities by incorporating MCC particles. Although osteoconductive, cellulose by itself does not stimulate cell growth and would need a compound such as PLL to synergistically recruit cells while keeping the scaffold sufficiently stable. The presented work mainly focuses on the effect of processing conditions on both MCC and PLL as the crystallinity level of the MCC is changed through hydrolysis, and by altering the pH of the PLL solution. The MCC content was also varied to study its correlation with the properties of the scaffold.

There is a variety of methods to fabricate scaffolds such as salt leaching, membrane lamination, super critical-fluid foaming, solid free form fabrication, and thermally induced phase separation (TIPS) [5]. Each of these methods has its own advantages and limitations, in regard to the resulting geometry of the pores, the pore structure or the overall homogeneity of the scaffold [42, 43]. For this work, TIPS was employed and the impact of the freezing temperature on the scaffold porosity and pore size distribution was evaluated.

2. Materials and methods

2.1 Materials

Microcrystalline cellulose (MCC) and poly(L-lysine-hydrobromide) (PLL) were purchased from Sigma-Aldrich. The chemical structure of PLL is shown in Figure 1 and has an average molecular weight of 150 kD as provided by the supplier. All other chemicals were obtained from Fisher Chemicals.

2.2. Sample preparation

Samples were prepared at pH 7 and 11.6 by dissolving a 100 mg PLL in 250 mL 0.1 M buffer solution with overnight stirring followed by sonication for 5 min in a bath sonicator, Branson 3510. The samples were casted on a Teflon® plate and dried in an oven at 60°C for 48 h to produce a film. The buffer solutions were prepared using a 0.1 M solution of monobasic potassium phosphate (KH_2PO_4) titrated to pH 7 and pH 11.6, respectively, with a 0.1 M potassium hydroxide (KOH) solution.

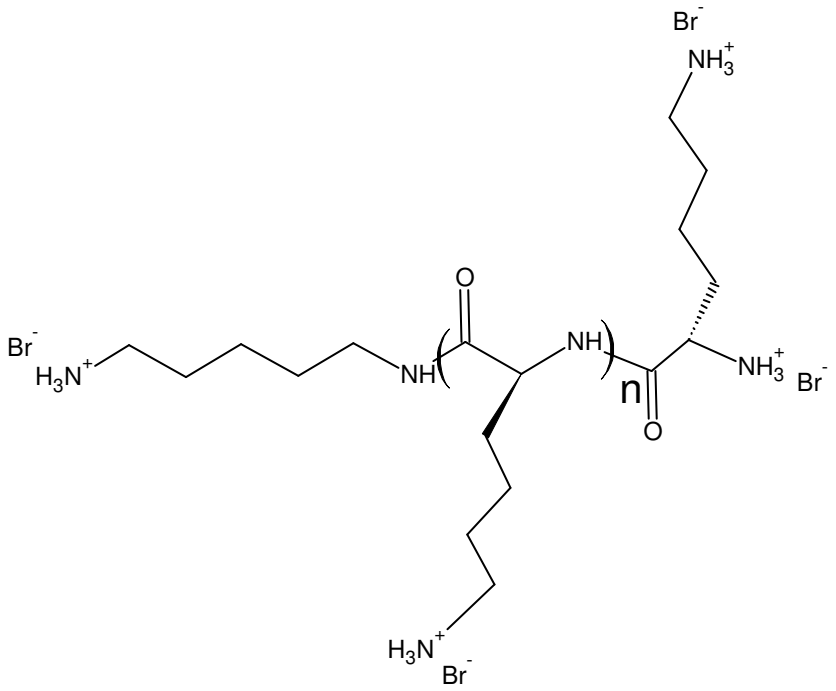

Figure 1. Chemical structure of poly(L-lysine-hydrobromide)

2.2.1. Cellulose hydrolysis

Microcrystalline cellulose (MCC) was dispersed in a 50% sulfuric acid at a ratio of MCC:H_2SO_4 1:8.75 [44]. The dispersion was equilibrated in an oil bath at 45˚C with vigorous stirring for 2 h. One set of samples (HMCC) was sonicated using a tip sonicator for 5 min at 30% amplitude with 30 s intervals and 5 s pausing; a second set (HMCC-NS) was directly washed without sonication. During sonication, a thermostated water bath was used to avoid the removal of sulfate groups on the surface of MCC by accidental overheating [45]. After sonication the sample was centrifuged at 6700 rpm for 10 min and washed repeatedly with deionized water until the pH of the solution became 5.

2.2.2. PLL/MCC and HMCC composite preparation

MCC and HMCC particles were dispersed in 25 mL of deionized water (pH 7) at various concentrations (see Table 1). The dispersion was placed in a bath sonicator for 20 min with a bath temperature of 25˚C. Measured amounts of PLL were added to each container, then sonicated for 30 min at the same temperature. The sonicator was turned to the degas mode for 10 min to remove air bubbles from the solution.

Table 1. Sample designation

Sample designation	MCC (%)	HMCC (%)	Preparation
PLC00	0	0	Dissolved in water (pH 7)
PLC02	2	0	Dissolved in water (pH 7)
PLC05	5	0	Dissolved in water (pH 7)
PLC10	10	0	Dissolved in water (pH 7)
PLC15	15	0	Dissolved in water (pH 7)
PLHC05	0	5	Sonication during hydrolysis
PLHC05-NS	0	5	No sonication during hydrolysis

2.2.3. Scaffold fabrication

The composite solutions prepared in the previous step were pre-frozen at temperatures of -23˚C for 3 h to solidify at a cooling rate of 1˚C/min by placing the container in a circulator chiller (60:40 vol% ethylene glycol:water coolant mixture). The solvent was removed from the samples by sublimation through lyophylization in a Labconco freeze drier at 7 mtorr (*ca.* 0.9 Pa) for 48 h. Samples were cooled at a constant rate of approximately 1˚C/min to produce homogeneous pore sizes throughout the structure. Some scaffolds were produced in tubular shape (suitable for vasculature scaffold applications) by casting the solution in concentric tubes before solidification. Disc shape samples of about 25 mm diameter were also produced and used for characterization.

2.3. Characterization

2.3.1. Fourier transform infrared spectroscopy (FTIR)

Samples were characterized with a Nicolet 6700 FT-IR spectrometer (Thermo Electron Corp.) using attenuated total reflectance (ATR) sampling mode and the spectra were processed using OMNIC 7.3 software package. A total of 98 scans with a resolution of 4 cm^{-1} were averaged for each sample.

2.3.2. Particle size distribution and surface zeta potential

Particle size distribution was measured for MCC and HMCC samples using NICOMP™ 380 ZLS (Particle Sizing Systems) based on multi-angle dynamic light scattering of the particles in water at 23˚C. The wavelength of the laser was 639.0 nm and the water viscosity was set to 0.933 cPoise with refractive index of 1.333, as recommended by the manufacturer for water solutions at 23˚C. Three samples were measured with 10 min scanning time and the results were analyzed using CW388 software where the volume weighted distribution was considered for the sample particle size after fitting to a Gaussian curve.

The same instrument was also used to measure the surface zeta potential (ζ-potential) of MCC, HMCC, PLL, MCC/PLL and HMCC/PLL, dispersed in deionized water at pH 7 with a scattering angle of 14.7˚ and a scan time of 2 min/run. Five replicate measurements were performed for each sample. The dielectric constant of 78.5 for water at 23 ˚C, and an electric field strength of 3.5 V/CM were set.

2.3.3. Scaffold density and volumetric porosity

The density and the porosity of the prepared scaffolds were measured by volume displacement, as schematically shown in Figure 2. A weighed sample of the scaffold was placed in a non-solvent (hexane) that does not swell the polymer. The initial volume of the hexane (V_1) was measured in a narrow test tube (to maximize the liquid displacement), then the sample was immersed in hexane and gently compressed to fill the air-pockets in the structure with the liquid. The sample was left for 5 min to equilibrate and the total volume was measured (V_2). Then the sample was removed and the volume of the remaining hexane was determined (V_3). The volumetric porosity (ε) can be calculated as the volume ratio of the air pockets and the total volume of the scaffold [46]:

$$\varepsilon = \frac{V_1 - V_3}{V_2 - V_3} \qquad (1)$$

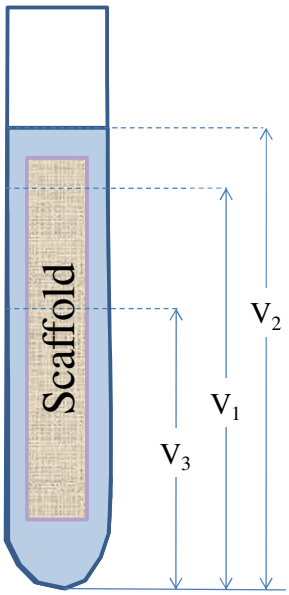

Figure 2. Measurement of the volumetric porosity and the density of the scaffolds

The density (ρ) of the scaffold can be calculated as follows:

$$\rho = \frac{m}{V_2 - V_3} \quad (2)$$

where m is the mass of the scaffold sample. The measured porosity is expected to be the minimum porosity of the sample with the assumption that part of the hexane may not penetrate through the scaffold or be removed from the sample before taking its weight.

2.3.4. Swelling

Scaffold samples were first conditioned at an ASTM standard laboratory atmosphere [47] at a temperature of 21±1˚C and a relative humidity of 65±2% for one week. Swelling was determined by placing a few drops of deionized water to cover a sample with mass m_1. After 15 min the sample was weighed and the mass recorded as m_2. Percent swelling was calculated based on the water uptake of the sample as:

$$S(\%) = \frac{m_2 - m_1}{m_1} * 100 \quad (3)$$

2.3.5. Crystallinity

The crystallinity of the samples was measured using Rigaku MiniFlex™ bench-top powder X-ray diffractometer (XRD) equipped with a nickel filtered Cu radiation with a wavelength of λ = 1.541 Å. The tube output voltage was 30 KV and the current was 15 mA. MCC containing samples were placed in a zero background holder and scanned at 2θ = 4˚ to 30˚

at 0.02˚ increments and a scanning rate of 0.1˚/min. HMCC and their composites were scanned at 2θ = 5˚ to 60˚, to accommodate for the crystallinity peaks of cellulose. To calculate the crystallinity index of a sample, the area under peaks assigned to reflect crystallinity were integrated, then summed and divided by the total area [44].

2.3.6. Surface morphology

Scanning electron microscopy (SEM) was used to observe the surface morphology of selected samples using a Zeiss EVO 50 scanning electron microscope. The micrographs of MCC and HMCC particles as well as the scaffold samples fabricated at -23˚C were characterized with a digital imaging and energy dispersive spectroscopy (EDS) system (Carl Zeiss SMT Inc.). The dried samples were mounted on an aluminum stub using a carbon double-sided tape, then sputter-coated with gold using EMS 550X auto sputter coating device (Electron Microscopy Sciences).

2.3.7. Statistical analysis:

The descriptive statistics for the resulting data were obtained using a probability value of 95% ($p<0.05$) to determine the significance. One-way analysis of variance (ANOVA) test was performed to compare groups of data.

3. Results and Discussion

3.1. Secondary structure of PLL

PLL was dissolved at pH 7 and 11.6. These pH values were selected because of the physiological pH being about 7.35 at a body temperature of 37.5˚C [48] and the pK_a value of PLL being 10.54 [10]. FTIR was used to study the secondary structure of PLL at these pH values where the amide I band is located between 1610 and 1690 cm^{-1} [49]. Figure 3 shows the section of the IR spectra that is relevant to this region for as-received PLL and PLL dissolved in pH 7 and 11.6 buffer solutions.

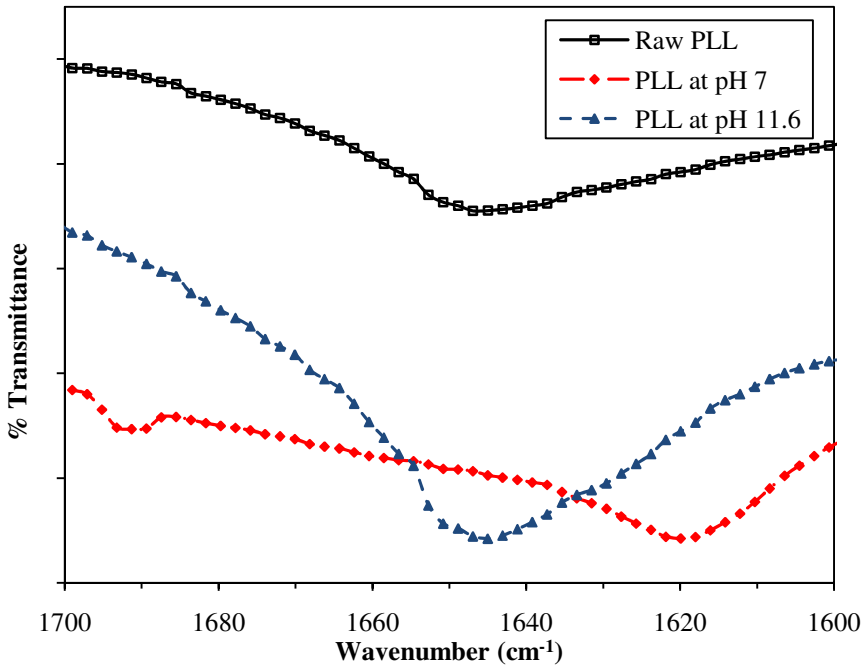

Figure 3. FTIR spectra for as-received PLL and for PLL dissolved at pH 7 and pH 11.6

PLL as-received as well as the sample prepared at pH 11.6 showed a band at 1650 cm^{-1}. In contrast, the spectrum of the sample at pH 7 showed two peaks at about 1620 and 1690 cm^{-1}. The band at 1650 cm^{-1} can be ascribed to the α-helix secondary structure while the peaks at 1620 and 1690 cm^{-1} can be assigned to β-platelet sheet secondary structure. The weak peak at 1690 cm^{-1} is attributed to the anti-parallel conformation of the β-sheet and commonly found in synthetically prepared polypeptides [10].

These results suggested α-helix secondary structure for the as-received PLL which remained in this conformation after dissolved in solutions at pH levels higher than its pK_a value. The polymer assumed β-sheet conformation at neutral pH and in solutions below its pK_a. Besides the pH, the secondary structure is also a strong function of the molecular weight of the PLL [50]. The high molecular weight (150 kD) of PLL used in this study was expected to result in higher transformation from α-helix to β-sheet conformation. The secondary structure of polypeptides is driven by the minimization of the conformational free energy due to hydrogen bonding, the electrostatic interactions, and the van der Waals forces [51]. Therefore, the polymer will be protonated at pH 7 and some cationic charges will develop on the polymer chain that will generate electrostatic repulsive forces. These forces can result in the breaking of the intrachain hydrogen bonds existing in the α-helix conformation and support the transformation to β-sheet structure in order to minimize the conformational energy of the polypeptide.

3.2.Cellulose hydrolysis

The surface morphology of MCC and HMCC particles is given in Figure 4. In the case of MCC with an aspect ratio that varied between 2 to 10, a fairly rough surface was observed. After hydrolysis, the particles look smaller and seem to have a flake-like surface.

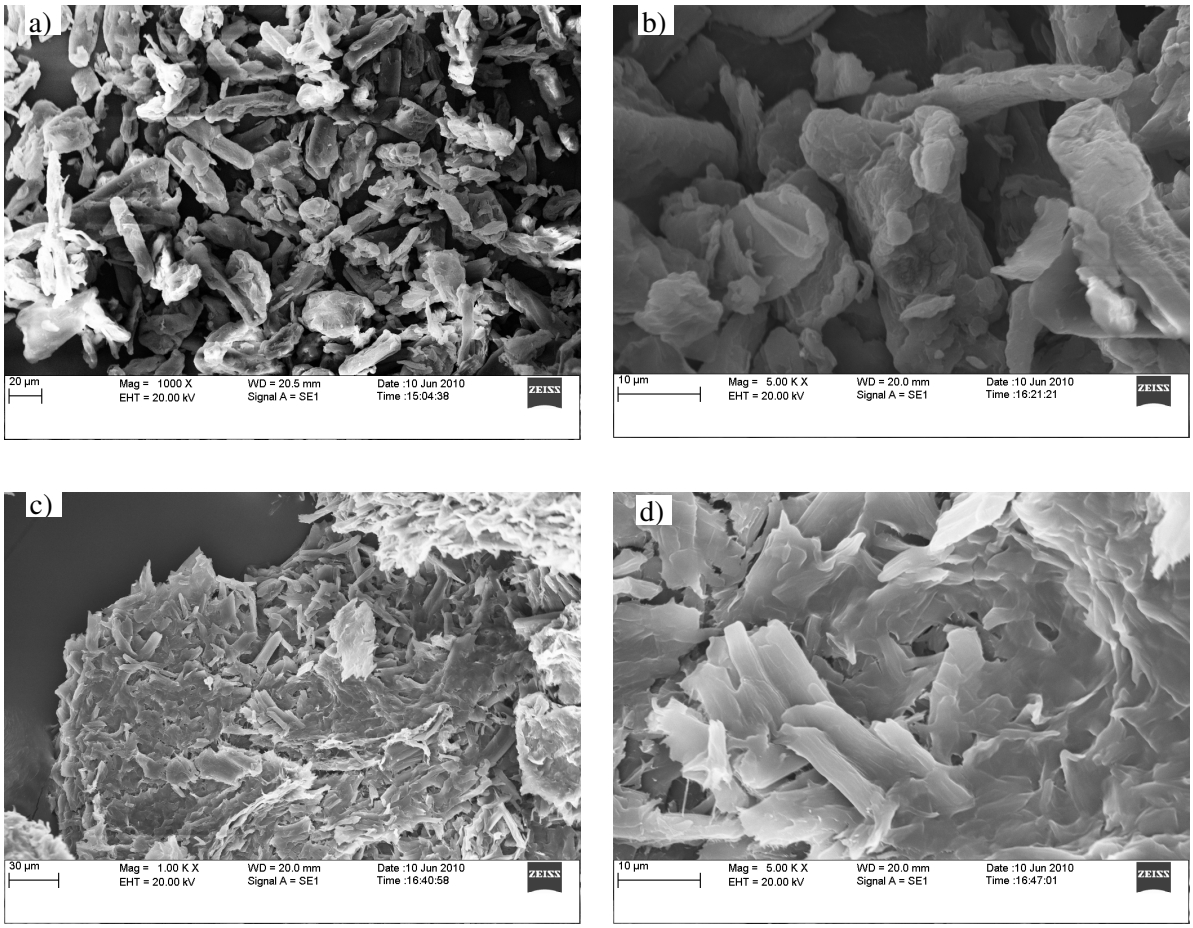

Figure 4. SEM micrographs for MCC (top) and HMCC (bottom) at different magnifications (a and c at 1 KX and b and d at 5 KX)

The x-ray diffractograms of the MCC and HMCC samples are displayed in Figure 5. The X-ray crystallinity results agreed reasonably well with the reported 50 to 70 % crystallinity ranges for MCC depending on the source of the cellulose [52]. Both hydrolysis methods resulted in about 25% increase in the crystallinity of the particles. The average particle sizes and particle size distributions were determined for the untreated MCC and the hydrolyzed samples and the results are listed in Table 2.

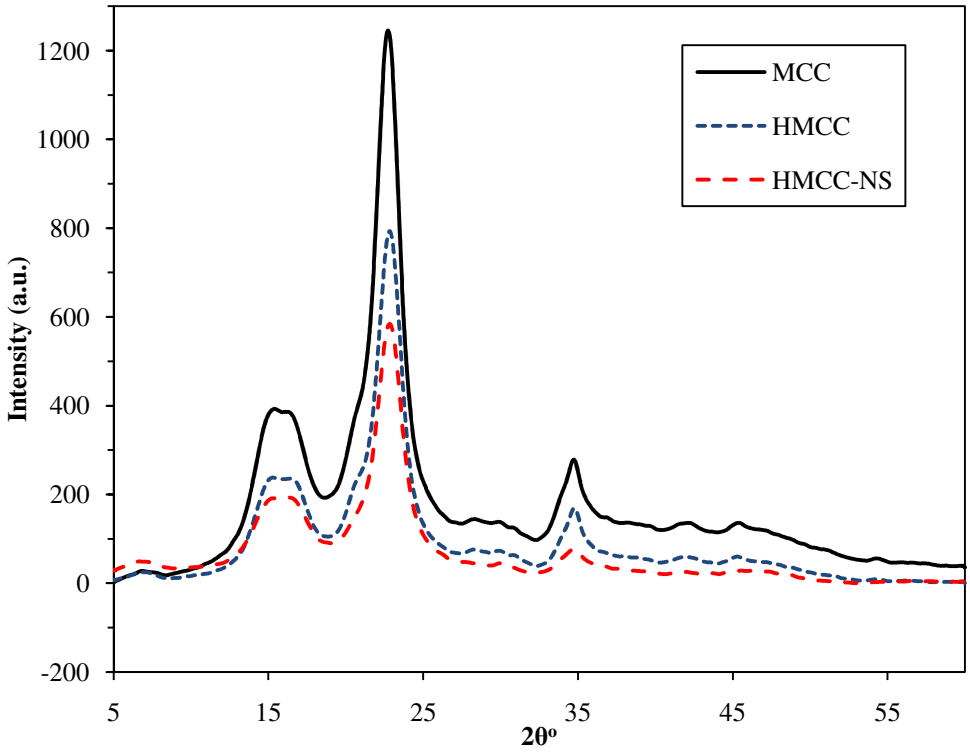

Figure 5. The XRD diffractograms for MCC, HMCC and HMCC-NS

Table 2. Measured particle size and zeta potential for cellulose particles

	particle size			ζ-potential	
	Average volume weight (μm)	Coefficient of variation	χ^2	ζ-potential (mV)	standard deviation (mV)
MCC	12	0.527	1.16	-33.55	1.28
HMCC	0.217	0.561	34.6	– 8.13	4.05
HMCC-NS	27.4	0.801	0.336	-7.56	8.24

The hydrolysis of MCC affected particle dimensions and surface ζ-potential by decreasing the average size of the particles to the nanometer range (about 200 nm) due to the removal of amorphous regions. When sonication was applied during the hydrolysis process, the resulting particles were relatively well dispersed and fairly small while the average particle size was higher (even higher than the original MCC particles) without sonication. It is possible that without sonication, particle aggregates were formed and resulted in the observed increase in size of the particles.

3.3. PLL/cellulose composites

The conformation of PLL/MCC composite was determined from the FTIR spectra presented in Figure 6. All samples had been prepared at pH 7 and formed into porous structures by freeze-drying. Only one band at 1650 cm^{-1} was observed for all these samples which indicated α-helical structure regardless of pH, composition, or processing method. Obviously, the β-sheet

conformation could not form under any of these conditions. It is possible that the temperature decrease during the freezing step is responsible for the observed conformation and the formation of hydrogen bonding between the polymer chains which would restrict β-sheet formation regardless of the pH value [53].

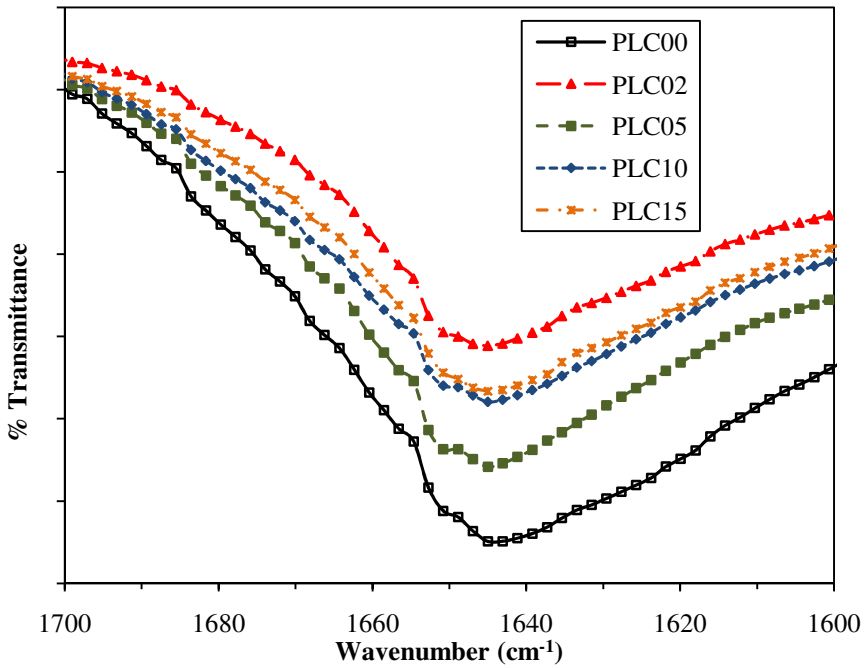

Figure 6. FTIR spectra for scaffolds with different concentrations of MCC

The ζ-potential for aqueous solution of PLL was found to be 102.34±22.74 mV and 59.98±14.18 mV for a solution with equal amounts of MCC and PLL. These results indicate a decrease in the positive surface potential of PLL with an amount closer to the negative value of MCC ζ-potential. This may imply an electrostatic interaction between the two components of the mixture that can help in a better integration of MCC particles in the PLL matrix.

The as-received PLL sample showed a small peak characteristic for the semi-crystalline PLL [10], as indicated in Figure 7, and its calculated crystallinity index was approximately 24%. X-ray crystallinity results for selected PLL/MCC and PLL/HMCC composite samples are also shown in Figure 7. The diffractograms for all PLL/MCC composites showed an additional shoulder that had developed after lyophylization. However, the overall crystallinity indices dropped to about 18% on the average which was surprising. The need for incorporating the hydrolyzed MCC into the PLL matrix seemed to be the logical consequence of this finding.

HMCC was incorporated into the PLL in place of MCC at a concentration of 5 wt.%. The crystallinity increased from 29% for the PLC05 sample to 33.5% for PLHC05 and to 44% for PLHC05-NS. The x-ray diffraction patterns of these samples are shown in Figure 7. The crystallinity of the PLL/MCC composites was lower than the crystallinity of the original PLL sample while an increase in the crystallinity was noticed in the samples with HMCC. As expected, the higher crystallinity of HMCC compared to MCC as well as the smaller size of HMCC particles with higher surface area might have improved the interaction between the cellulose particles and the PLL matrix. The increase in crystallinity was found to correlate with a decrease in the swelling of the composite samples.

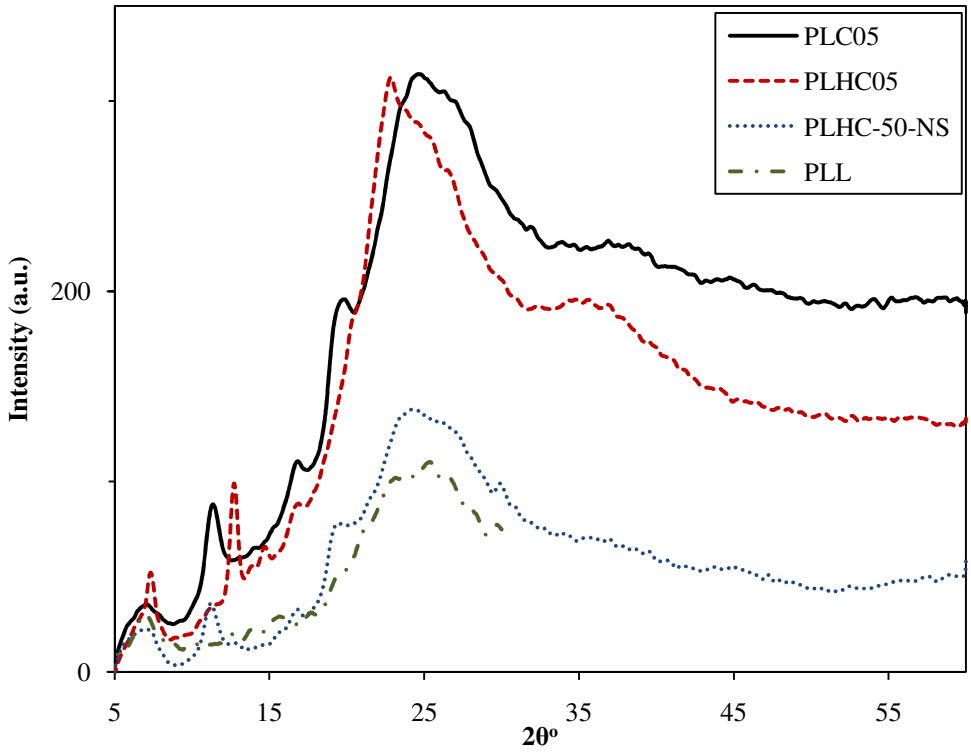

Figure 7. X-ray diffraction patterns for PLC05, PLHC05, PLHC05-NS, and PLL

3.4. Scaffold fabrication

In order to produce a scaffold that is sufficiently porous, prepared aqueous solutions for PLL and MCC were pre-frozen at -23˚C prior to lyophylization and porous structures were created. The effect of freezing temperature on the pore size and porosity of the produced scaffolds is driven by the thermodynamics of the polymer solution where phase separation takes place during freezing. The scaffold samples prepared by freezing at -23˚C have separate phases of solidified solvent and polymer which were then exposed to a high vacuum (7 mtorr) during lyophylization. Sublimation of the solvent left voids which became a continuous network of pores, a characteristic for the temperature induced phase separation (TIPS) process.

Table 3. Volumetric porosity, density, and swelling for scaffolds prepared at different conditions

	Volumetric porosity (%)	**Density (g/cm^3)**	**Swelling percentage (%)**
PLC00	81.31	0.0945	3428.6
PLC02	92.31	0.0816	1546.3
PLC05	93.83	0.0818	747.0
PLC10	88.57	0.0869	697.5
PLC15	87.34	0.0789	296.6
PLHC05	85.43	0.0748	208.2
PLHC05-NS	86.92	0.0954	102.6

The density and volumetric porosity for scaffolds are listed in Table 3 which shows the impact of processing parameters on the properties of the produced scaffolds. An increase in the volumetric porosity, for example, is expected to result in a decrease of the structure density due to the increase in the void volume. Accordingly, an increase in crystallinity leads to an increase in density of the scaffold structure and decrease the swelling of the sample. Swelling of the scaffold in connection to crystallinity had to be used to express the improved physical stability of the composite samples since the mechanical properties could not be measured and no conclusive results were obtained.

Conclusions

The basic hypothesis behind this work was that introducing microcrystalline cellulose (MCC) into poly(L-lysine) (PLL) composite structures may lead to enhanced mechanical properties of PLL. This hypothesis was investigated by studying the conformation of PLL in different pH, modifying the crystallinity of MCC through hydrolysis, including MCC in different proportions, and forming porous structures suitable for scaffold application. Results showed the formation of a composite structure with attractive electrostatic forces between the components and a higher crystallinity if MCC was further hydrolyzed. The secondary structure of PLL was found to be affected by the micro-environmental as well as the processing conditions during freeze-drying. It was observed that the hydrolysis conditions of the MCC particles were crucial in regard to the morphology and the crystallinity of HMCC with a slightly higher crystallization produced at mild hydrolysis condition. The studied samples showed that the inclusion of HMCC particles resulted in an increase of the crystallinity of the PLL composite while MCC particles without further hydrolysis decreased the degree of its crystallinity. Crystallinity and swelling were used as indirect indicators for the mechanical stability of the scaffold.

Chapter III: PLL/PLA Molecular-Scale Composite with Networked PLA Structures

Abstract

This chapter investigates the possibility of molecular level mixing of poly(L-lysine) and a networked structure of poly(L-lactide) (PLA) to form a composite. The core efforts in this part focus on: 1) synthesizing branched PLA that can be subsequently crosslinked, and 2) forming a homogenous solution of PLL and the branched PLA in the same solvent. A novel solution-based polymerization method was applied to overcome the problems associated with the common bulk polymerization of branched PLA. The method also utilizes organocatalyst during the reaction to avoid the toxicity side effects of the common organometallic catalysts in biomedical applications. Different samples of linear and branched PLA were produced in solution and their properties were analyzed using FTIR, NMR, GPC, and DSC. One of the main findings during the thermal analysis of linear PLA samples was the crystallization of the sample that was observed at two temperatures during heating cycles. The double peak melting of the samples was investigated by modulated-DSC to be a result of the crystallization that takes place simultaneously with melting. The branched PLA was crosslinked in a homogeneous solution with Poly(L-lysine) after it was recovered from its salt form. The crosslinking reaction was monitored using FTIR and the conversion of the reactants was calculated. The solution-based method introduced in this work could open the door for more branched PLA reactions with better controlled conditions.

1. Introduction

Poly (L-lactide) is a biocompatible and bioresorbable polyester that is widely used in biomedical applications [54] as a homopolymer or in a mix with other polymers. These biomedical applications extend from orthopedic fixation devices [55], wound resorbable sutures [56], artificial skin [57], stents [58], controlled drug delivery [59], to tissue engineering [60-63]. Polymerization can be achieved by a lactic acid poly-condensation reaction; however, difficulties in removing the condensed water during the reaction lead to products with low molecular weight [64, 65]. This explains the advantages of producing PLA through ring opening polymerization (ROP) of lactide monomers where no water removal is required during the reaction. The relief of the conformation strains in the cyclic monomers is the driving force for ROP which is thermodynamically favorable since it results in reducing the total free energy of the molecule [66]. To complete the ROP process, a catalyst is required and coordination-insertion mechanism takes place [54, 64, 65]. The catalysts usually used for these purposes are organometallic catalysts with zinc (II), titanium (IV), aluminum (III), and tin (II) as shown in Figure 8-a.

a) Organometallic catalysts

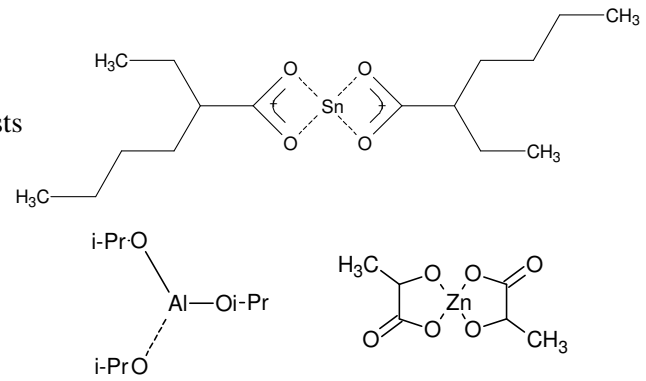

b) Organocatalysts

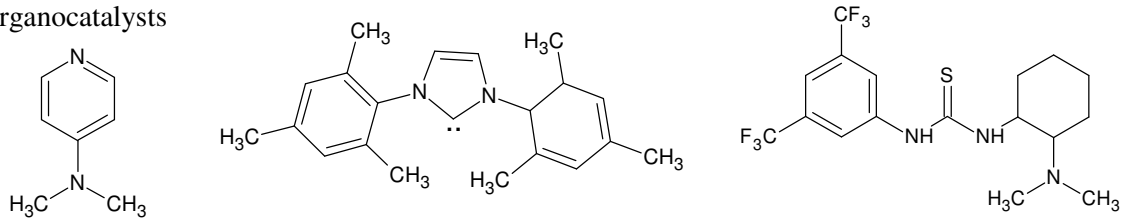

DMAP NHC TA

Figure 8; a) Structure of organometallic catalysts: tin(II) octanoate [$Sn(Oct)_2$], aluminum(III) isopropoxide [$Al(Oi\text{-}Pr)_3$], and zinc(II) lactate [$Zn(Lact)_2$]. b) Structure of organocatalysts.

The metal of the catalyst should be removed from the product after reaction since they may have side effects on the properties of the polymeric product. For example, tin (commonly used in ROP of lactides) residues remaining in products from some ring opening polymerization reactions were determined to have a concentration more than 300 ppm and can have a toxic effect in biomedical applications [54]. Therefore, organocatalysts, as shown in Figure 8-b, were introduced to replace the organometallic catalysts in ROP [67]. Examples of these catalysts are 4-(dimethylamino)pyridine (DMAP), N-heterocyclic carbene (NHC), and thiourea-amine (TA), which proved to be effective in producing high molecular weight living polymers at high conversion rates [65, 68, 69]. In a recent study, Kadota *et al* [70] used DMAP together with its protonated form (DMAP.HX) as organocatalysts with both basic and acidic sites. The study

proved that this combination was more effective than DMAP alone in ROP of PLA. On the other hand, the protonated form of DMAP alone as a catalyst was not able to activate the reaction.

The ROP also requires an initiator besides the catalyst for the reaction to proceed. Nucleophilic initiators are used for this purpose and the number of active sites on the initiator determines the architecture of the produced polymers. Nucleophiles with one active site (e.g. ethanol) result in linear PLA [66, 67, 71] while using multi-ol compounds (e.g. pentaerythritol) as initiators yield branched chains of PLA [54, 68, 72, 73].

The common methods for PLA ring opening polymerization are bulk and solution methods. Solution reactions are mainly applied for the production of linear PLA at low temperatures [74] while bulk polymerization is commonly used with branched PLA. The reason that solution polymerization is not used for most PLA branched archetictures is the low solubility of the initiators. These initiators are usually highly polar, have high melting points, and do not easily dissolve in common solvents together with lactide monomer and polymers [75].

Two problems are typically encountered with bulk polymerization of branched PLA. In bulk polymerization, the reacting monomer, initiator, and catalyst as well as the produced polymer will be present in the bulk and the polymer might be soluble in the monomer. However, the viscosity of the reaction mixture increases as more polymer is produced which makes it difficult to remove traces of the nonreacted components after polymerization due to diffusion limitations [76]. The reaction rates in bulk polymerization are not easily controlled because of the heat of polymerization and the development of hot spots that usually lead to the autoacceleration or the Trommsdorff effect [76, 77].

The specific problem of bulk polymerization with the current system of branched PLA can be demonstrated by working at the polymerization temperatures reported in the literature which ranges between 130 ˚C and 180 ˚C, where the later is used more frequently. These temperatures may not be suitable for processing lactide monomer as it can decompose at these relatively high temperatures.

The described problems of bulk polymerization can be overcome by using solution polymerization which allows more thermal control over the reaction by dissipating the heat of polymerization through the greater mass of the solvent and limiting the viscosity increase in the reactor [76]. The goals of this work were to first introduce a new solution-based method for polymerizing the branched PLA and to deal with the solubility issue of the polyol initiator (pentaerythritol) in a common solvent in presence of the other reactants (monomer, and catalyst). Secondly, an attempt was made to form a homogeneous solution of both poly(L-lysine) and the branched PLA to perform the PLA crosslinking reaction. PLL in form of a salt allows the dissolution in aqueous media but not in organic solvents. However, organic media are required for the crosslinking reaction which includes isocyanate components that are very sensitive to water residues in the reaction and the reaction should therefore be conducted in anhydrous conditions. In this work, two procedures are investigated to encounter this problem. In one, the poly(L-lysine.hydrobromide) was neutralized using a base at a pH higher than the pKa of the polymer, and in the other an ion exchange resin was used to recover only the poly(L-lysine). The produced samples were studied for their chemical structure and physical properties. The poly(L-lysine) was recovered in a form suitable for dissolution in a common solvent with the branched PLA. Then, PLA crosslinking reaction was performed while PLL was present indication the possible formation of a semi-interpenetrating polymer network.

2. Materials and Methods

2.1. Materials

(3S)-cis-3,6-dimethyl-1,4-dioxane-2,5-dione (L-lactide monomer) with a purity of 98%, 4-(dimethylamino)pyridine (DMAP catalyst) with a purity of ≥99%, 2,2-bis(hydroxymethyl) 1,3-propanediol (pentaerythritol), and hexamethylene diisocyanate (HDI) were ordered from Sigma-Aldrich Co. Dimethylformamide (DMF) was purchased from Fisher Scientific and used as a solvent during the synthesis of the branched polymers while dichloromethane (DCM) was used with linear polymers and it was obtained with a tetrahydrofuran (THF) that was stabilized for use in GPC from Mallinckrodt Baker Inc. During the characterization, a commercial sample of PLA (purchased from Druect Corp., Pelham, AL) was used as a reference.

2.2. Synthesis

2.2.1. Synthesis of branched PLA

The L-lactide monomer was dissolved in DMF with the catalyst and the pentaerythritol initiator in a well sealed rounded-bottom flask. The reaction took place at constant temperature (60 ˚C) in an oil-bath. The DMF was dried from water residues by mixing with anhydrous sodium sulfate and 3Å molecular sieves at least 24 hours before use. The experimental details of the reactions are listed in Table 4, and the schematic representation for the reaction is illustrated in Figure 9.

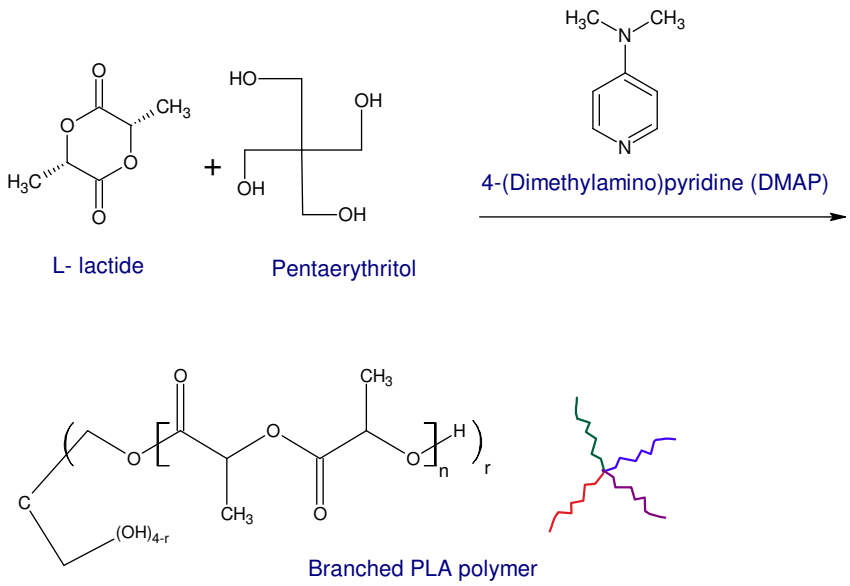

Figure 9. Schematic representation for the branched polymer synthesis

Table 4. Reaction conditions to synthesize branched and linear PLA samples

	Sample ID	Initiator	Catalyst/ Initiator (eq.)	Monomer/ Initiator (eq.)	Temperature (˚C)
Branched PLA	PLA030-B	PET-ol	4	30	60
	PLA300-B	PET-ol	10	300	60
	PLA600-B	PET-ol	10	600	60
	PLA900-B	PET-ol	10	900	60
Linear PLA	PLA030-LE	Eth-ol	4	30	35
	PLA300-LE	Eth-ol	10	300	35
	PLA600-LE	Eth-ol	10	600	35
	PLA030-L	m-cresol	9	30	35
	PLA250-L	m-cresol	16	250	35
	PLA300-L	m-cresol	16	300	35
	PLA900-L	m-cresol	16	900	35

2.2.2. Synthesis of linear PLA

Control samples of linear PLA were synthesized using the procedure outlined by Nederberg *et al.* [67] by dissolving predetermined amounts of L-lactide monomer, DMAP catalyst, and an anhydrous ethanol or m-cresol as initiators. The components were added in different ratios of the initiator: catalyst: monomer as indicated in Table 4. Samples with low monomer concentrations were synthesized with small amount of the catalyst (4:1 equivalent as measured by the ratio of amines in the catalyst to the hydroxyl groups in the initiator). The catalyst was then increased to enhance the kinetics of the reaction since slow reactions were observed, in this work as well as in Nederberg's work, during the use of higher monomer: initiator ratios. Reactions were equilibrated in an oil bath at 35 ˚C and performed in dichloromethane (DCM) which is known as a good solvent for both the monomer and the produced polymer. The solvent was dried by mixing with anhydrous sodium sulfate and 3Å molecular sieves at least one day before the use in the reaction.

For all samples, the solution of the produced polymer was extracted using 0.5N HCl and DCM as the organic phase. The polymer was extracted from the top aqueous layer three times using DCM, then the extracted organic solution was washed three more times with deionized water. To facilitate the extraction and avoid the formation of an emulsion, a small amount of brine solution was added. The collected organic phase was dried using magnesium sulfate then it was filtered under vacuum. The transparent filtrate solution was placed in the oven at 60 ˚C to evaporate the solvent and collect the polymer product. For branched PLA samples, the above extraction procedure was followed but with more separation steps using DCM to extract the polymer. Excess amounts of water were added to the solution during the extraction to remove DMF which is miscible in water.

2.3. PLL inclusion in the PLA networked structure

2.3.1. PLL neutralization

A sample of poly(L-lysine.hydrobromide) salt was dissolved in water. The resulting pH was 5.55. The solution was placed in a separation funnel and methylene chloride was added to form the organic layer during the extraction. 0.1N sodium hydroxide (NaOH) was added until a pH of 11.9 was measured. The mixture formed an emulsion with a white gel material that was collected by filtration and was identified to be the PLL using FTIR.

Alternatively, PLL was recovered by placing the aqueous solution of PLL salt over the particles of Amberlite® IRA-400, chloride form, as ion exchange resin. The sample was left on the resin bed overnight with stirring and the obtained solution had a pH of 9.5. The PLL solution was then filtered and the solvent was evaporated by placing in the oven at 60 ˚C for three hours.

2.3.2. PLA crosslinking

The recovered solid PLL sample was dissolved in anhydrous DCM and mixed with the synthesized branched PLA. Hexamethylene diisocyanate (HDI) was used as a crosslinker and 5 μL were added with DMAP catalyst to the reactor which was sealed and equilibrated at 35 ˚C for five hours with stirring. To monitor the reaction, a few drops of the solution were placed on a special polyethylene card that is used for FTIR. The card was scanned as a background at the beginning of the reaction, then it was scanned on time intervals of three minutes during the initial phases of the reaction and every ten minutes after about 40 minutes.

2.4. Characterization

2.4.1. Fourier transform infrared spectroscopy (FTIR)

Samples were tested with Nicolet 6700 FT-IR spectrometer (Thermo Electron Corp., Madison, WI) using attenuated total reflectance (ATR) sampling mode and the spectra were processed using OMNIC 7.3 software package. Results were recorded for the samples with 98 scans, a resolution of 4 cm^{-1}, data spacing of 1.928 cm^{-1}, and KBr beam-splitter was used.

2.4.2. Nuclear magnetic resonance (NMR)

^{1}H NMR was performed on the samples using 400 MHz Varian NMR spectrometer system (Varian Inc., Palo Alto, CA) and data were analyzed using ACD/NMR Processor (Advanced Chemistry Development Inc., Toronto, Ontario – Canada). Polymer samples were dissolved in deuterated chloroform ($CDCl_3$) at 26 ˚C and the chemical shifts (δ) were expressed in ppm with respect to the signal of tetramethylsilane (TMS) which was used as an internal reference. Both the monomer (lactide) and the pentaerythritol were dissolved and tested in deuterated dimethyl sulfoxide (DMSO).

2.4.3. Gel permeation chromatography (GPC)

Molecular weights were measured on a Viscotek system (Model 270 Series from Viscotek Co., Houston, TX) equipped with GMHHR-M column and triple detectors for refractive index (RI), light scattering (right angle light scattering RALS and low angle light scattering LALS), and viscometer. The system was calibrated using a standard polystyrene sample (PolyCal® TDS-PS-N) and the multi-detector – homopolymer method was used for calculation. The calculation method was then recalibrated using a commercial PLA sample with a molecular weight of 12.3 KD. PLA samples were dissolved in THF with concentrations in the

range of 1.2 mg/mL to 3.5 mg/mL and filtered during injection with 0.2 μm PTFE membrane filter (Whatman®, Maidstone, England). The flow rate of the mobile phase in the system was 1 mL/min and the loop size for injection was 100 μL.

2.4.4. Thermal gravimetric analysis (TGA)

Thermal gravimetric analysis (TGA) was performed using Q500 TGA (TA Instruments, New Castle, DE) by placing the sample in a platinum pan and purging with nitrogen at a rate of 60.0 mL/min. The instrument was calibrated using calcium oxalate monohydrate standard using the procedure provided by the instrument manufacturer. Samples were tested by taking the mass reading from the micro-balance during the temperature ramping to 500 °C at a rate of 10 °C/min. The results were plotted and analyzed using TA Instruments Universal Analysis package (Version 4.3A).

2.4.5. Differential scanning calorimetry (DSC)

Samples were analyzed for their thermal transitions using Q2000 differential scanning calorimetry (DSC) (TA Instruments, New Castle, DE). Samples were placed in standard aluminum pans under a nitrogen environment with a flow rate of 50.0 ml/min. The temperature of the sample was decreased to -5 °C at a rate of 10 °C/min then ramped up to 200 °C at the same rate, then the same procedure was repeated two times for each sample. Modulated experiments were performed at a slower rate of 1 ˚C/min and amplitude of 0.7 ˚C in a period of 60 seconds. The results were analyzed using TA Instruments Universal Analysis package (Version 4.3A).

3. Results and Discussion

3.1. Branched PLA

The branched samples were synthesized according to the core-first approach [78, 79] which allows a control of the structure and the length for each arm more than the arm-first approach [80]. In this approach, linear PLA chains are joined together with a proper coupling agent or terminator that reacts with the functionalized end groups of the linear chains for creating branched polymers. During the first experiments for adjusting the reaction conditions, the amount of catalyst was varied and it was found that it did not affect the molecular weight of the produced polymer. Only the ratio of the monomer to the initiator was found to be an effective determinant factor. Similar results for the amount of catalyst were reported in the literature [81].

First attempts to synthesize branched PLA using bulk polymerization at different temperatures between 130 ˚C to 180 ˚C were used. These experiments were not successful as the lactide monomer was found to decompose and leave black residues in the reactor. This observation was further investigated using thermal gravimetric analysis (TGA) for the reactants. TGA results showed that an early decomposition of lactide has occurred. A weight loss of about 10% was observed when reaching a temperature of 120 ˚C as shown in Figure 10. On the other hand, pentaerythritol maintained it structural integrity and did not disintegrate at higher temperatures. A weight loss of about 10% for pentaerythritol due to decomposition was observed at temperature of about 250 ˚C. This explains the reason for using high temperatures in bulk polymerization which are required to melt the pentaerythritol, however, these high temperatures are not suitable for the lactide monomer.

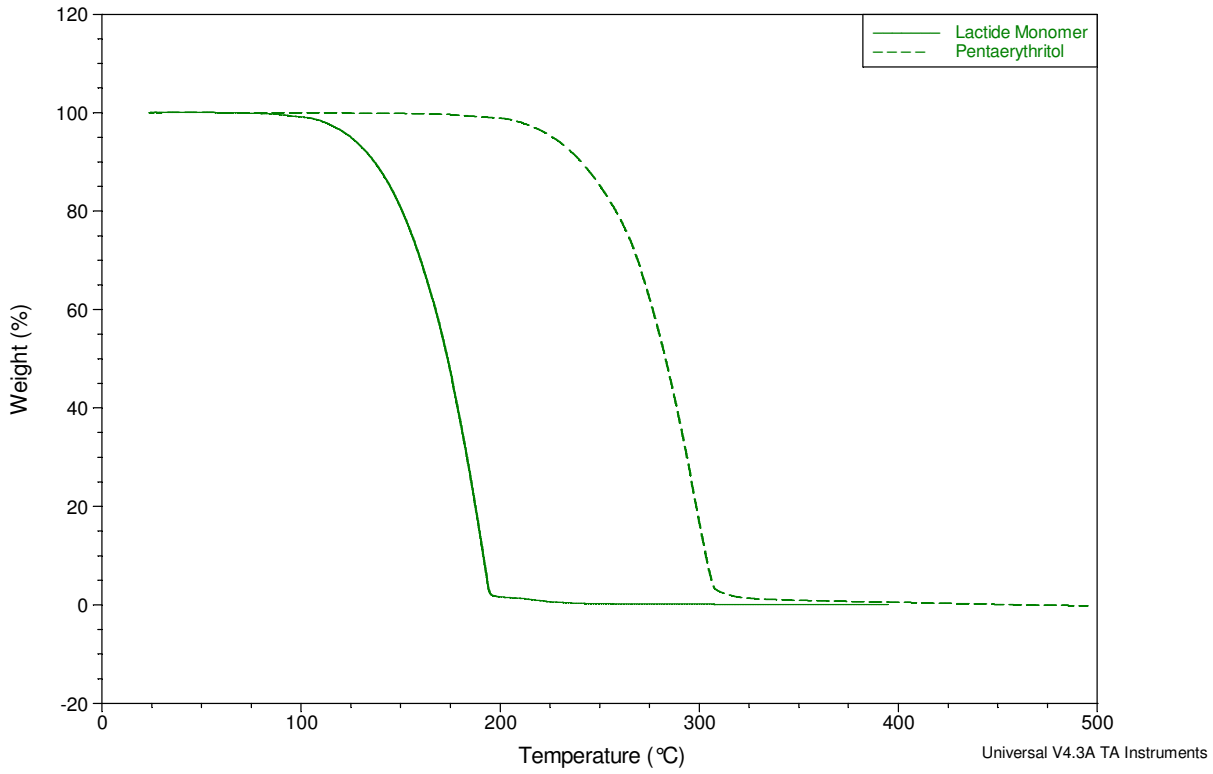

Figure 10. TGA results for the lactide (monomer) and the pentaerythritol (initiator)

Solution-based polymerization was investigated to overcome the decomposition problem in the system and the other problems mentioned before with bulk polymerization. Different solvents were applied to dissolve the reactants, especially those solvents that are known to dissolve the lactide monomer; however pentaerythritol (the initiator) was hard to dissolve in many of them due to its high polarity and the strong attractive hydrogen bonds between the molecules. Dimethylformamide (DMF) was found to be able to dissolve pentaerythritol at temperatures above 50 ˚C as well as to dissolve the other reactants to allow homogenous solution for the reaction. To verify the progress of the reaction, the chemical composition of the reactants as well as the produced samples were analyzed using ^{1}H NMR.

The monomer showed two characteristic peaks on the ^{1}H NMR spectrum as indicated in Figure 11 with the doublet at $\delta \approx 1.66$ ppm corresponding to the protons on the methyl group and the quartet at $\delta \approx 5.10$ ppm corresponding to the protons on the carbon attached to it. The results of integration for these peaks matched the number of the six protons on the methyl groups and the two protons bonded to the carbon atoms number 2 and 5 on the graph.

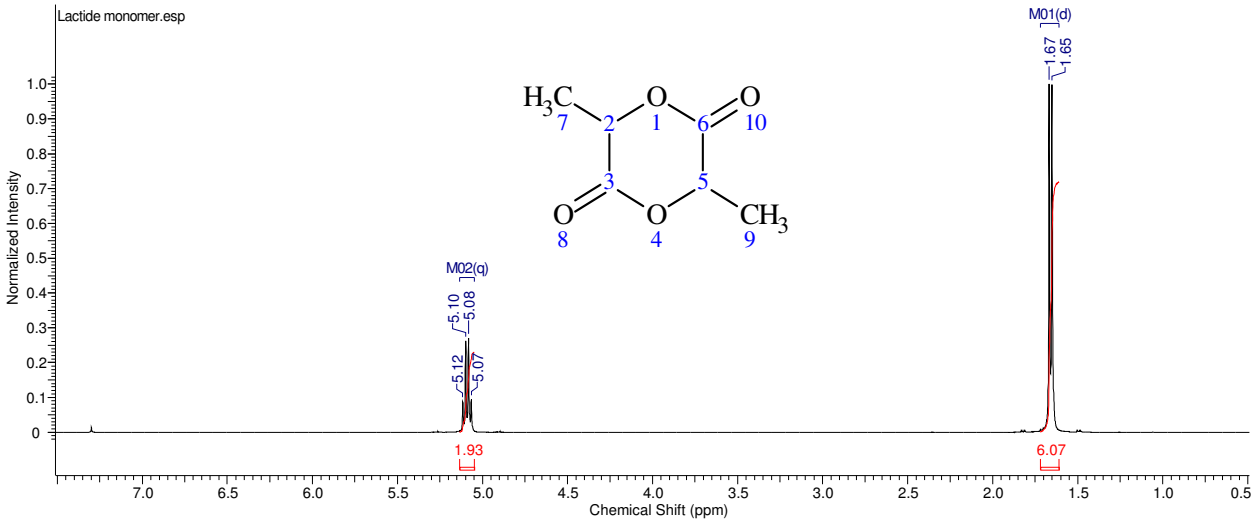

Figure 11. ^{1}H NMR spectrum for the lactide monomer (400 MHz, CHLOROFORM-d) δ ppm 1.66 (d, J=6.82 Hz, 6 H) 5.09 (q, J=6.57 Hz, 2 H)

The ^{1}H NMR spectrum for the pentaerythritol shown in Figure 12 demonstrates the peaks for the two proton types in the methylene and the hydroxyl groups. The M01 doublet at $\delta \approx 3.36$ ppm corresponds to the protons in the methylene group while the M02 triplet at $\delta \approx 4.21$ ppm corresponds to the protons in the hydroxyl groups. The integration of these peaks results in the ratio of 2:1 which is the same ratio between the eight protons in methylene groups to the four protons in the hydroxyl groups of the pentaerythritol. The other two marked peaks on the spectrum correspond to the DMSO solvent at $\delta \approx 2.51$ ppm, and water residues at $\delta \approx 3.43$ ppm.

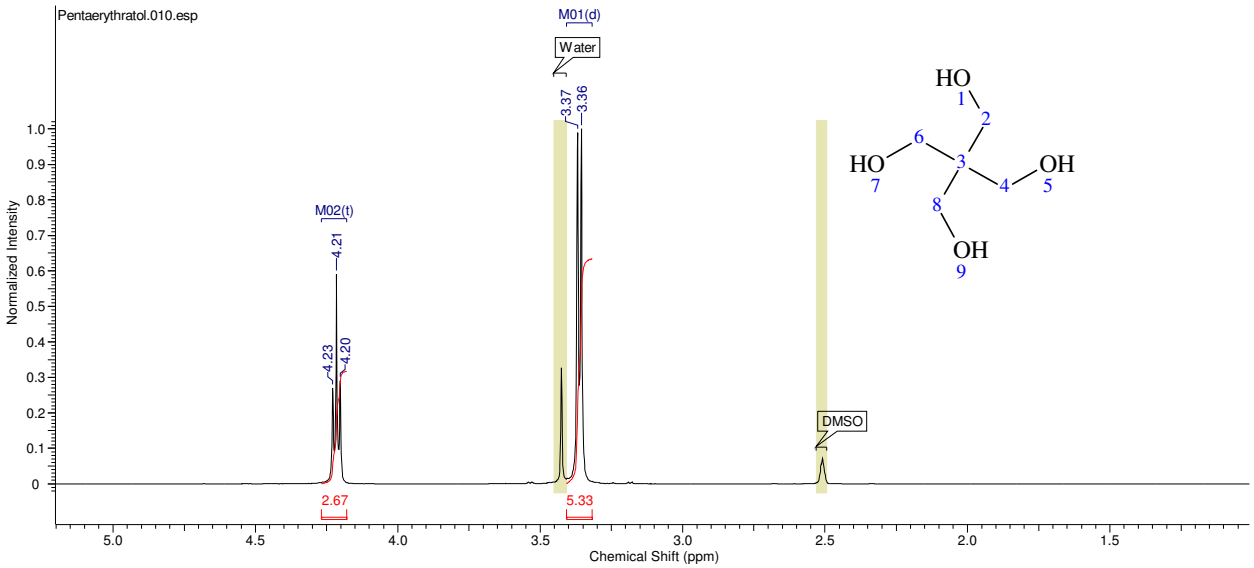

Figure 12. ^{1}H NMR spectrum for the pentaerythritol (400 MHz, DMSO-d6) δ ppm 3.36 (d, J=5.16 Hz, 5 H) 4.22 (t, J=5.41 Hz, 3 H)

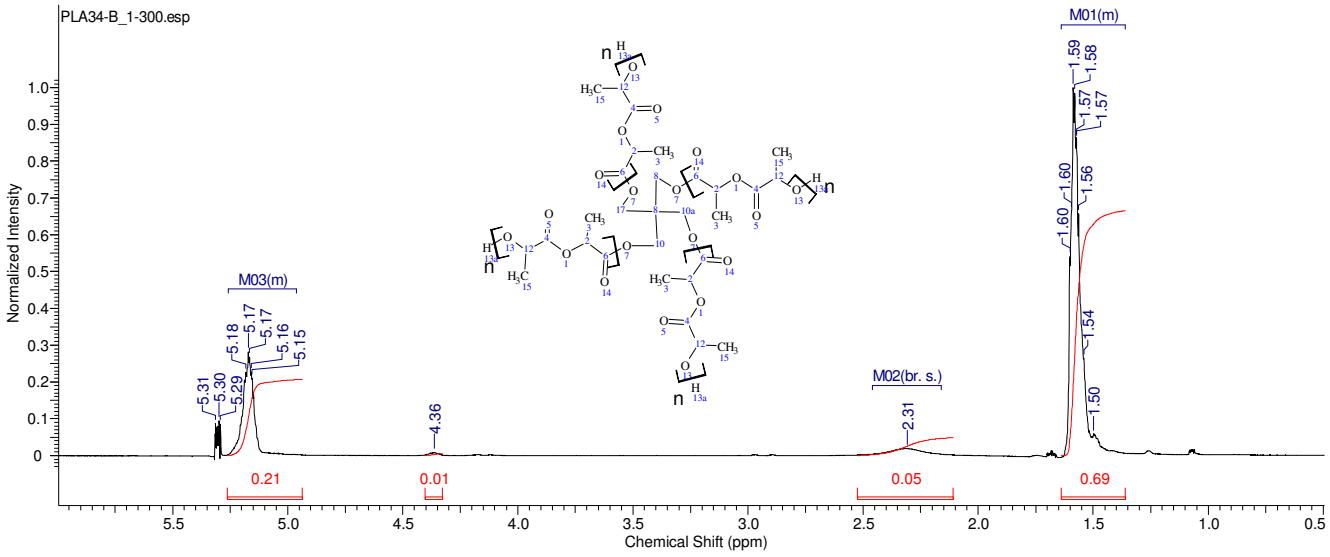

Figure 13. ^{1}H NMR spectrum for a branched PLA sample (400MHz, CHLOROFORM-d) δ = 4.96 - 5.26 (7H, m, M03), 2.31 (2H, br. s., M02), 1.36 - 1.64 (23H, m, M01)

The ^{1}H NMR spectrum of a branched sample is shown in Figure 13 with the M01 multiplet at $\delta \approx$ 1.57 ppm corresponding to the methyl pendent groups (numbers 3 and 15 shown on the structure), the broad singlet M2 at $\delta \approx$ 2.31 ppm corresponding to the hydroxyl end groups [82], and the M3 multiplet at $\delta \approx$ 5.17 ppm corresponding to the hydrogen atoms attached to the alpha carbons (numbers 2 and 12 illustrated on the structure). The signal at $\delta \approx$ 4.36 ppm corresponds to the methylene groups in the pentaerythritol (assigned numbers 10, 10a, 8, and 17). The absence of peaks in the chemical shift region between $\delta = 3$ and 4 indicates the absence of the hydroxyl groups at the ends of the pentaerythritol [82, 83] which could imply the growth of an arm at each end and the formation of a branched PLA.

3.2. Linear PLA

Linear PLA samples were produced in DCM solutions at relatively low temperatures (35 ˚C) and initiated with ethanol and m-cresol as two different initiators. M-cresol was chosen for two reasons; the first is its high boiling temperature which allows the initiator (about 5µl) to remain in the reactor at elevated temperatures. The second reason is the inductive effect of the methyl group which is attached to the benzene ring that allows the delocalization of the negative charge by resonance on the oxygen atom [84]. This results in increasing the reactivity of the m-cresol as a nucleophile. The monomer-activated mechanism [67] is suggested for the current linear ROP reaction where the nucleophilic attack takes place between the alcohol and the monomer-DMAP complex as illustrated in Figure 14. The reaction proceeds when the terminal hydroxyl of the opened dimer acts as a nucleophilic center that helps the chain to grow by attacking a new monomer complex. This mechanism has the features of living polymerization reactions where the polymer chain continues to grow as long as monomer exists in the reactor [64].

The chemical structure of the linear PLA samples was tested using ^{1}H NMR and FTIR. The ^{1}H NMR spectrum for a linear PLA sample is illustrated in Figure 15 which shows the chemical shift of the protons on the methyl groups at the multiplet M02 at $\delta \approx$ 1.56 ppm, corresponding to the methyl groups in the main chain and the doublet M03 at $\delta \approx$ 1.69 ppm corresponding to the methyl group closer to the chains ends and deshielded by the hydroxyl end group. The quartet M05 at $\delta \approx$ 5.16 ppm corresponds to the protons on the alpha carbons on the polymer backbone. The peaks at the aromatic region with chemical shifts between $\delta \approx 7$ to 8 ppm correspond to the protons on the m-cresol initiator. These peaks are small because of the low concentration of the initiator in the reaction.

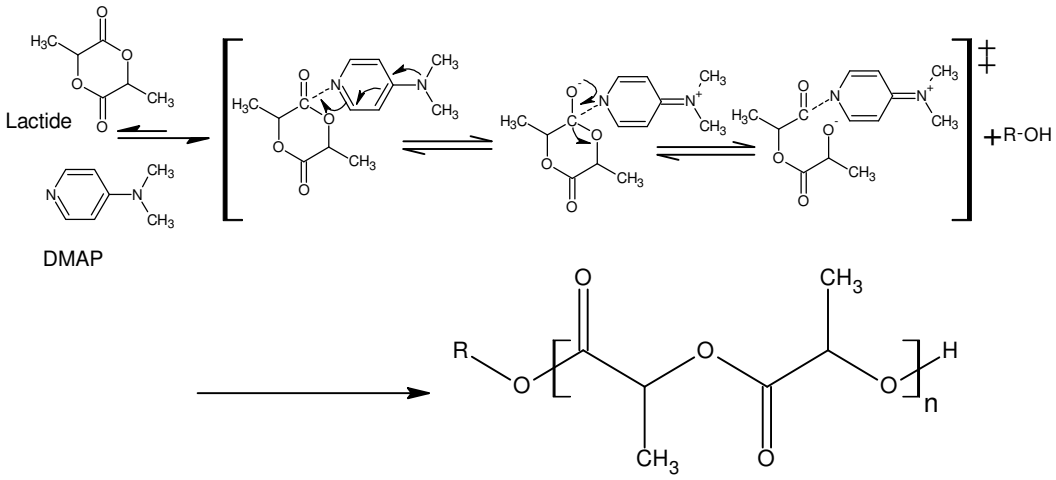

Figure 14. A possible polymerization pathway suggested by Nederberg et al. [67]

FTIR spectrum of a linear PLA sample is shown in Figure 16 and the assignments for its peaks are reported in Table 5 with a comparison for the assignments reported in the literature [85]. The calculated root mean square error (RMSE) for the experimental and the literature peak vibration values is 3.652 cm^{-1} which indicates a reasonable matching factor for the experiments.

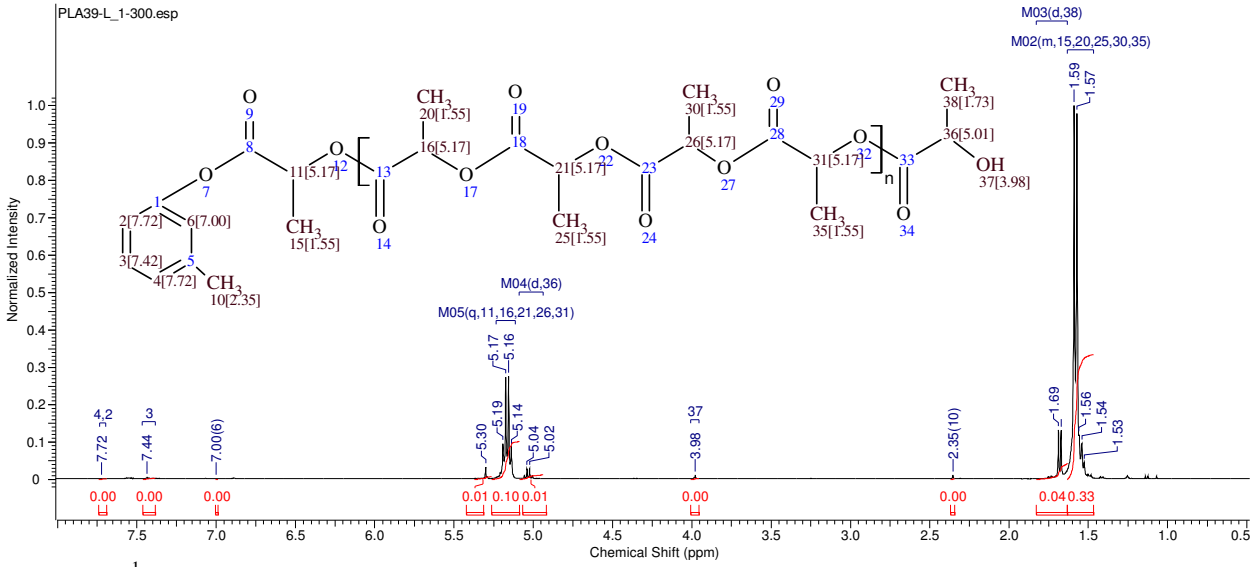

Figure 15. ^{1}H NMR spectrum for PLA linear sample (PLA300-L) (400MHz, CHLOROFORM-d) δ = 5.16 (6H, q, J = 6.9 Hz, H-11, 16, 21, 26, 31), 5.03 (1H, d, J = 6.7 Hz, H-36), 1.68 (3H, d, J = 6.7 Hz, H-38), 1.47 - 1.63 (21H, m, H-15, 20, 25, 30, 35)

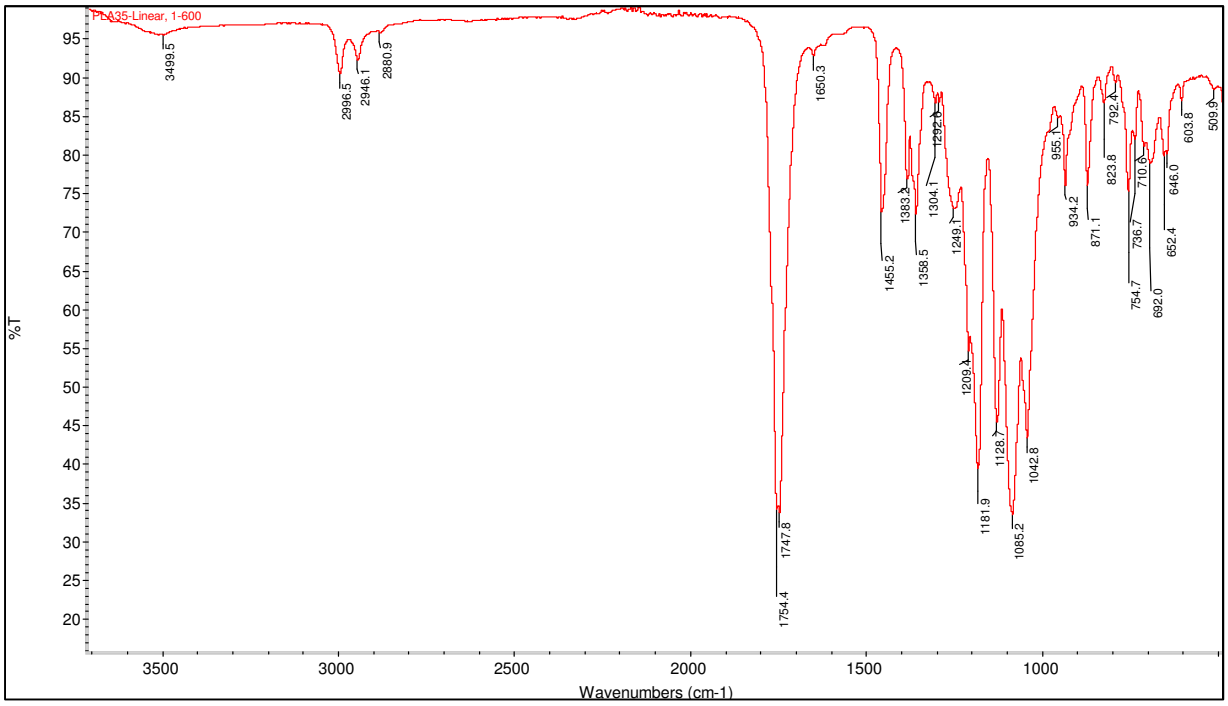

Figure 16. FTIR spectrum for a linear PLA sample

Table 5. Spectral assignment for linear PLA sample based on the literature [85] compared to the experimental values (calculated RMSE= 3.652 cm^{-1})

Assignment	Literature Frequency (cm^{-1})	Experimental Frequency (cm^{-1})
Skeletal vibration	755	754.7
O–H deformation	870	871.1
Symmetric C–O stretch (ether)	1,048	1042.8
Asymmetric C–O stretch (ether)	1,092	1085.2
Symmetric C–O stretch (ester)	1,132	1128.7
Asymmetric C–O stretch (ester)	1,184	1181.9
CH3 symmetric deformation	1,384	1385.5
CH3 asymmetric deformation	1,456	1455.2
C=O stretch	1,759	1754.4
CH3 symmetric stretch	2,881	2880.9
CH3 asymmetric stretch	2,948	2946.1
CH3 asymmetric stretch	2,997	2996.5
O–H stretch (acid terminator)	3,506	3499.5

The molecular weights of the produced linear samples were evaluated using GPC and the results are shown in Table 6 and Figure 17. Sample PLA030-L could not be tested because of the relatively small molecular weight compared to the exclusion limit of the column which is 10^6 Da. Results showed a relatively small polydispersity index (PDI) for the samples and range from 1.07 to 1.133 which was lower than the PDI for PLA polymers that are synthesized with step-growth polymerization methods [65]. The measured molecular weights matched the theoretically predicted molecular weights to a reasonable extent.

Table 6. Molecular weights of linear PLA samples as measured by GPC

	PLA250-L	PLA300-L	PLA900-L
Peak RV - (ml)	7.340	7.213	7.073
Mn - (Daltons)	35,748	43,744	138,057
Mw - (Daltons)	39,463	49,553	148,497
Mz - (Daltons)	46,545	61,939	168,668
Mp - (Daltons)	32,048	38,552	117,417
Mw / Mn	1.104	1.133	1.076
Theoretical Mn	36,033	43,239	129,717

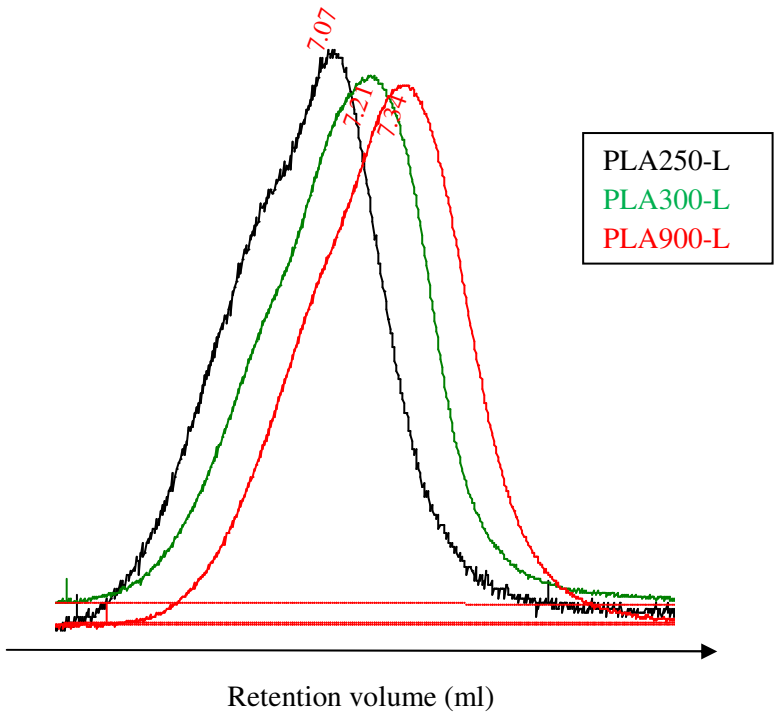

Figure 17. GPC results for PLA linear samples with different molecular weights

Molecular weights of PLA samples prepared with ethanol as an initiator are listed in Table 7. The measured molecular weight was observed to be lower than the theoretically expected value and the PDI is generally higher than its counterpart in samples prepared from m-cresol as initiator. There is a possibility that side and transestrification reactions may have caused these high values of PDI.

Table 7. GPC results for linear PLA samples prepared with ethanol initiator

	PLA030-LE	**PLA300-LE**	**PLA600-LE**
Peak RV - (mL)	10.267	7.853	7.403
M_n - (Daltons)	2,548	31,368	61,054
M_w - (Daltons)	4,589	37,136	213,716
M_z - (Daltons)	7,892	48,801	323,252
M_p - (Daltons)	3,801	28,718	14,295
M_w / M_n	1.801	1.184	3.500
Theoretical M_n	4,320	43,200	86,400

Thermal properties of the linear samples were determined using the DSC and are shown in Figure 18 to Figure 20. A summery for the transitions is listed in Table 8. The crystallinity of the polymer (X_c) was estimated by calculating the ratio of the melting energy (ΔH) to the enthalpy of fusion for a theoretically perfect PLA (ΔH_f) with the value of – 93.7 J/g [86].

The DSC results for these samples showed two unexpected peaks in the spectrum where a shoulder before the melting as well as a double melting peak were consistently observed in all samples. Since no crystallization peaks were obtained for the samples during their cooling cycles, the shoulder before the melting could possibly be attributed to the crystallization of the

sample. Similar crystallization peaks were reported in the literature for PLA [87, 88]. To support this explanation, the integrated areas under the curve at these humps were compared to the area of the melting peaks. Results of the integration showed close values for these peaks. It could therefore be hypothesized that crystals were formed during the sample heating.

Another unexpected result in the DSC spectra was the bimodal melting peak which occurred in all the samples. In some cases this double melting was observed during the first heating cycle, then reversed to a single peak in the second cycle and *vice versa*. This melting behavior was reported for PLA and other semi-crystalline polymers, especially for PLA samples prepared by solvent evaporation method [89]. These double endothermic peaks were explained by the simultaneous melting and recrystallization that takes place during melting [90]. The recrystallization was studied by wide-angle X-ray diffraction (WAXD) on poly(butylene naphthalate) as reported by Yasunaua et al [91] who conducted a similar study on PLA.

Table 8. Summary of DSC results for PLA linear samples

	PLA030-L	**PLA250-L**	**PLA300-L**	**PLA900-L**
Glass transition temperature (˚C)	37.75	55.6	50.60	50.92
Melting temperature (˚C)	140.82	148.36	148.42	151.63
Crystallization temperature (˚C)	94.38	116.91	124.41	102.21
Crystallization energy J/g	33.70	40.68	19.89	37.90
Melting energy J/g	33.78	40.41	20.41	38.65
Estimated crystallinity (Xc)	36.05	43.13	21.78	41.25

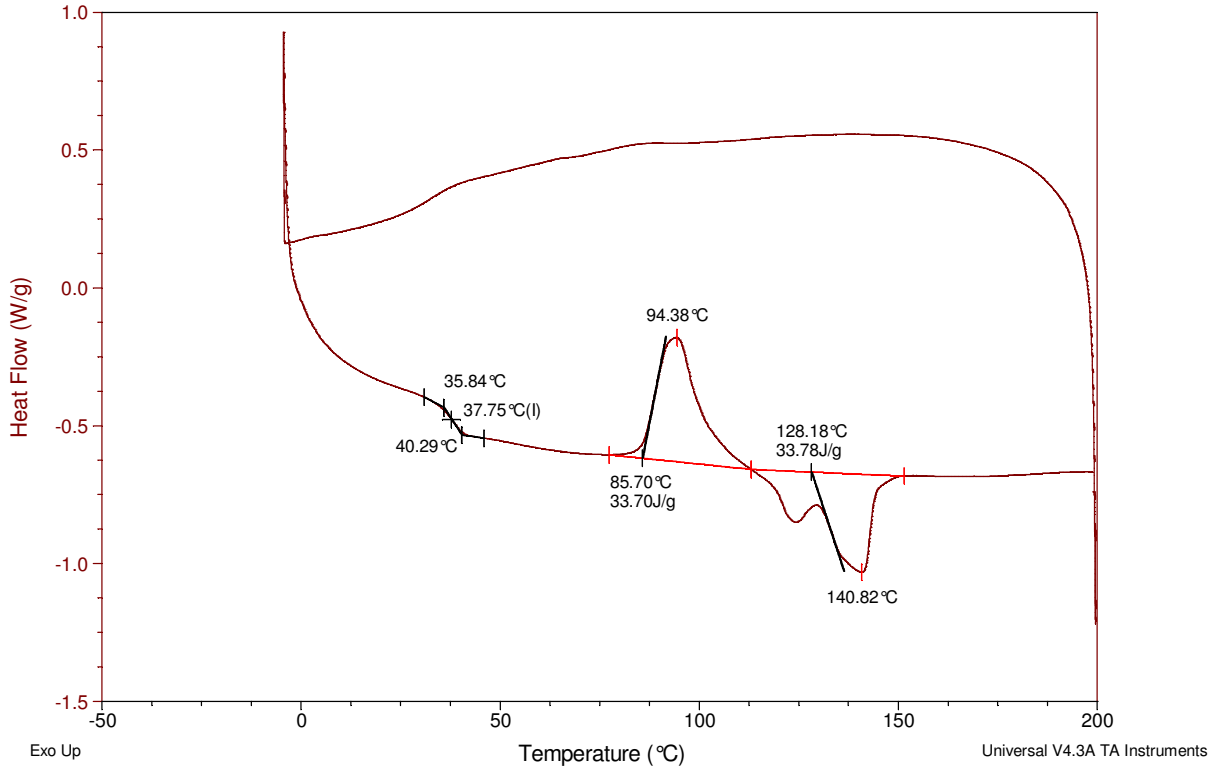

Figure 18. DSC spectrum for the sample PLA030-L

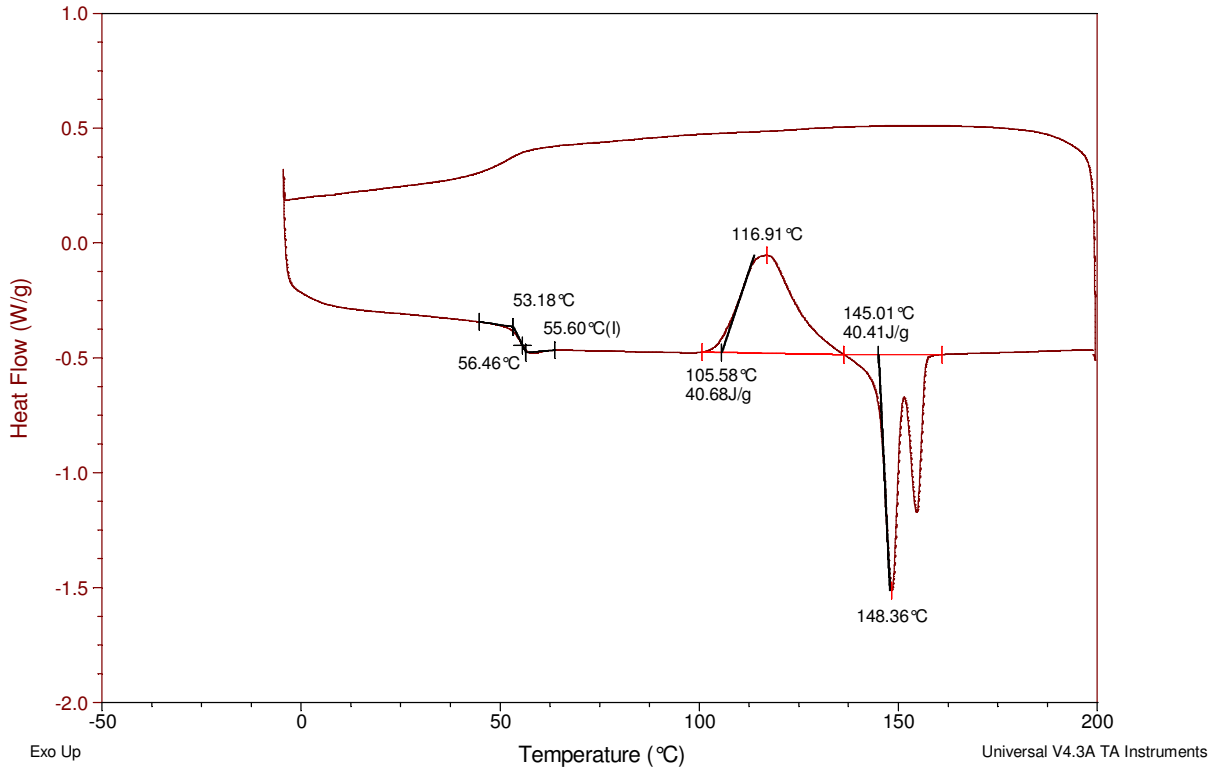

Figure 19. DSC spectrum for the sample PLA250-L

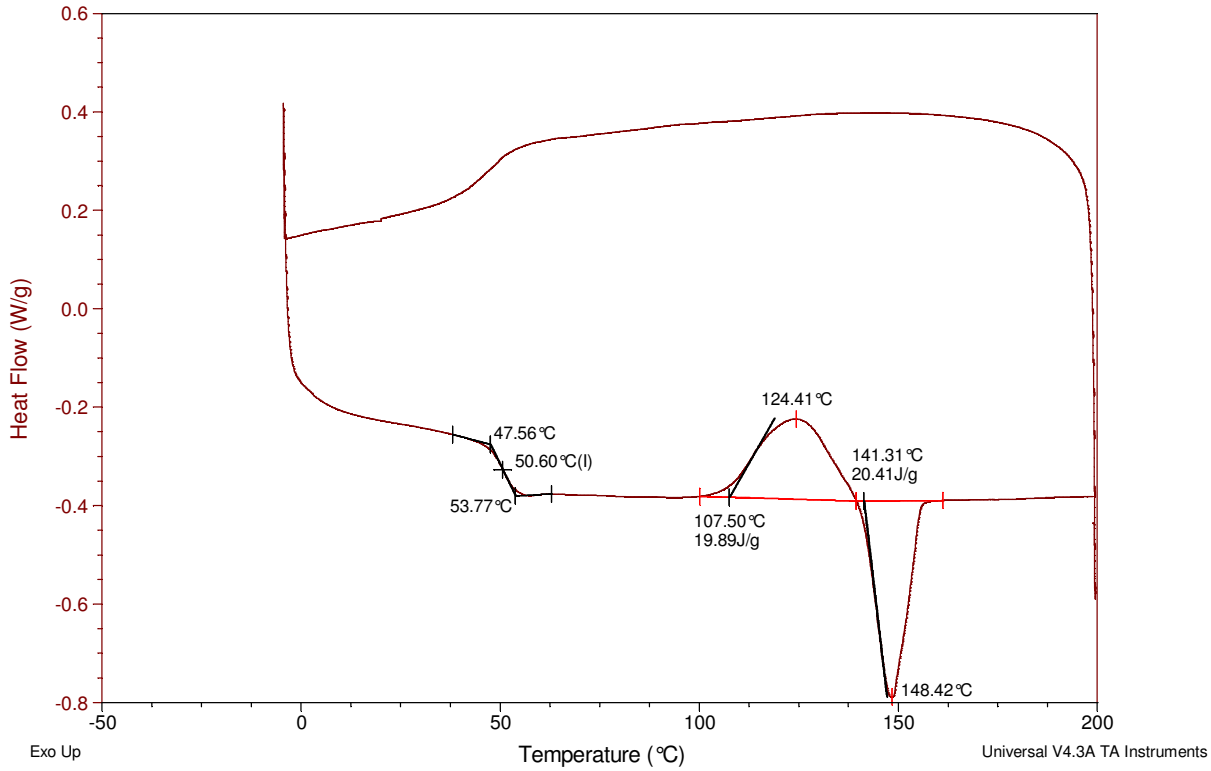

Figure 20. DSC spectrum for the sample PLA300-L

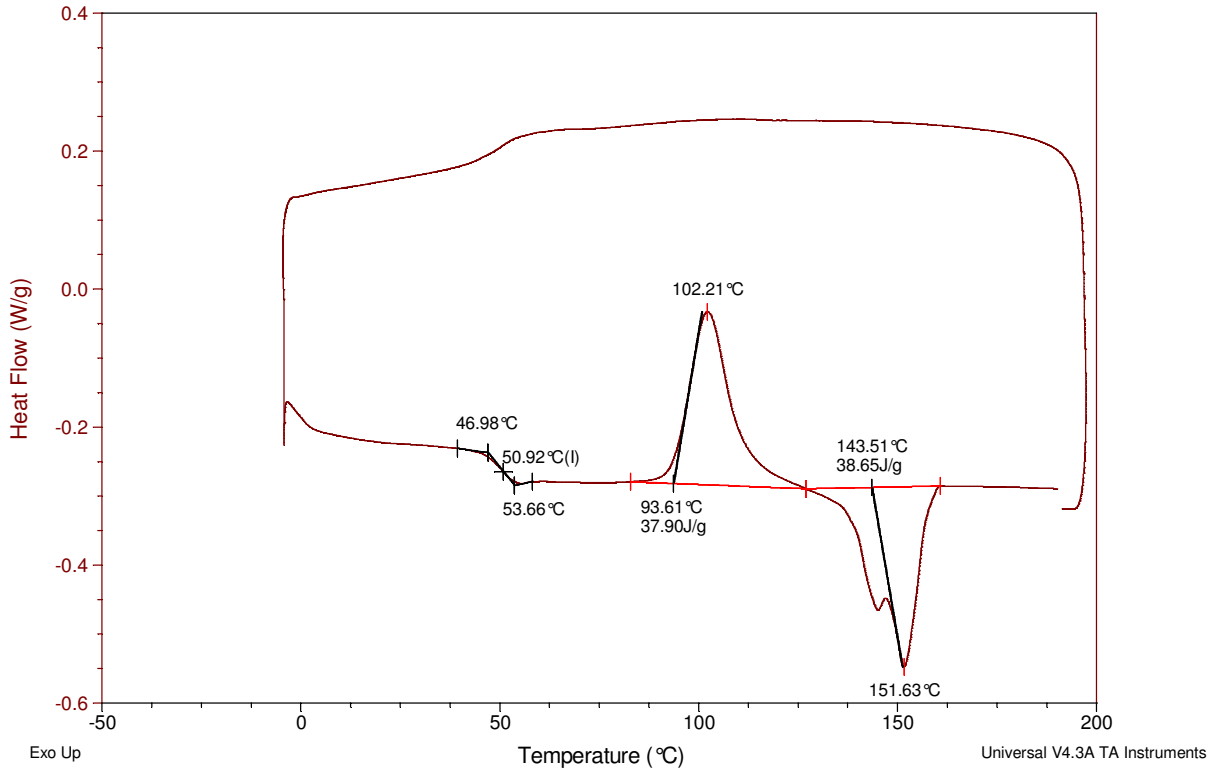

Figure 21. DSC spectrum for the sample PLA900-L

By comparing the spectra in Figures 23 to 26 to the spectrum of a commercial PLA sample, shown in Figure 22, a crystallinity peak appeared during the cooling cycle and no shoulder was observed in the heating cycle for the commercial sample. The double melting peak was observed in the second heating cycle for the commercial sample which implied that the polymer started to form well defined crystals which then melted and were not able to completely recrystallize as indicated by the energy difference between the two peaks. The remaining crystalline part could possibly be recrystallized simultaneously during melting on the second heating cycle. This could have produced the observed double melting behavior. If this was the case, the suggested reasoning behind this bimodal melting for the synthesized samples would be a likely explanation.

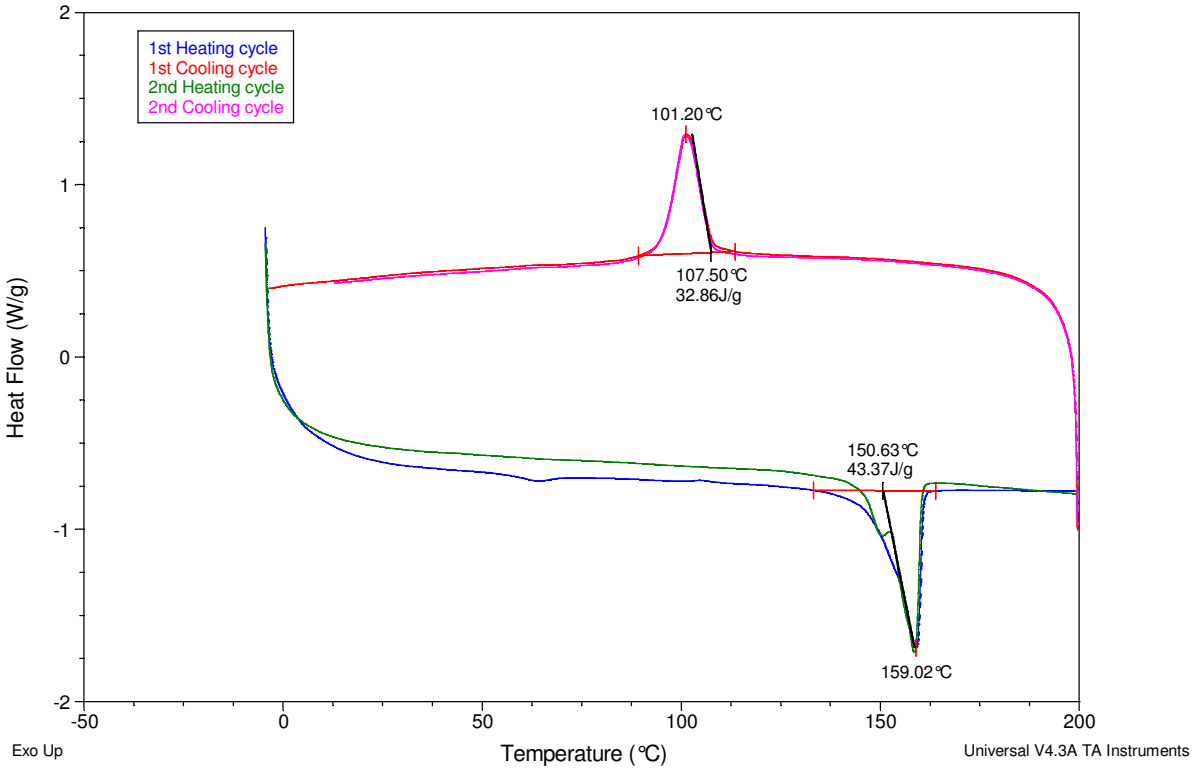

Figure 22. DSC scpectrum for a commercial linear PLA sample

Modulated DSC was performed to further investigate the occurrence of the double melting peak and the shoulder during heating for the semi-crystalline PLA. Modulated DSC allows the separation of reversing and nonreversing phenomena in the sample. Glass transition and melting are reversible events and will be expected to appear on the reversible heat flow curve while the relaxation and recrystallization are nonreversing events and will be expected to appear on the nonreversing heat flow curve [88]. To conduct this experiment sample PLA300-L was thermally tested using modulated DSC at slow rate of 1 ˚C/min as shown in Figure 23. The glass transition temperature of the sample can easily be seen on the reversible heat flow curve indicated in Figure 24 at about 50 ˚C and the melting of the sample is around 153 ˚C which is located within the reported T_m range of 130-180 ºC for PLA [68].

The slow rate of testing allows the crystallization of the sample to take place during its cooling as indicated by the crystallinty peak at around 109 ˚C in the heat flow curve as well as in the nonreversing heat flow curve in Figure 25. The sample continued to crystallize during the second heating cycle with a small shoulder indicated on the graph and double melting was observed again in the sample. The modulated-DSC results provided reasonable evidence for the occurrence of crystallization of the samples where the shoulders were observed in the heating cycles and simultaneous crystallization and melting took place.

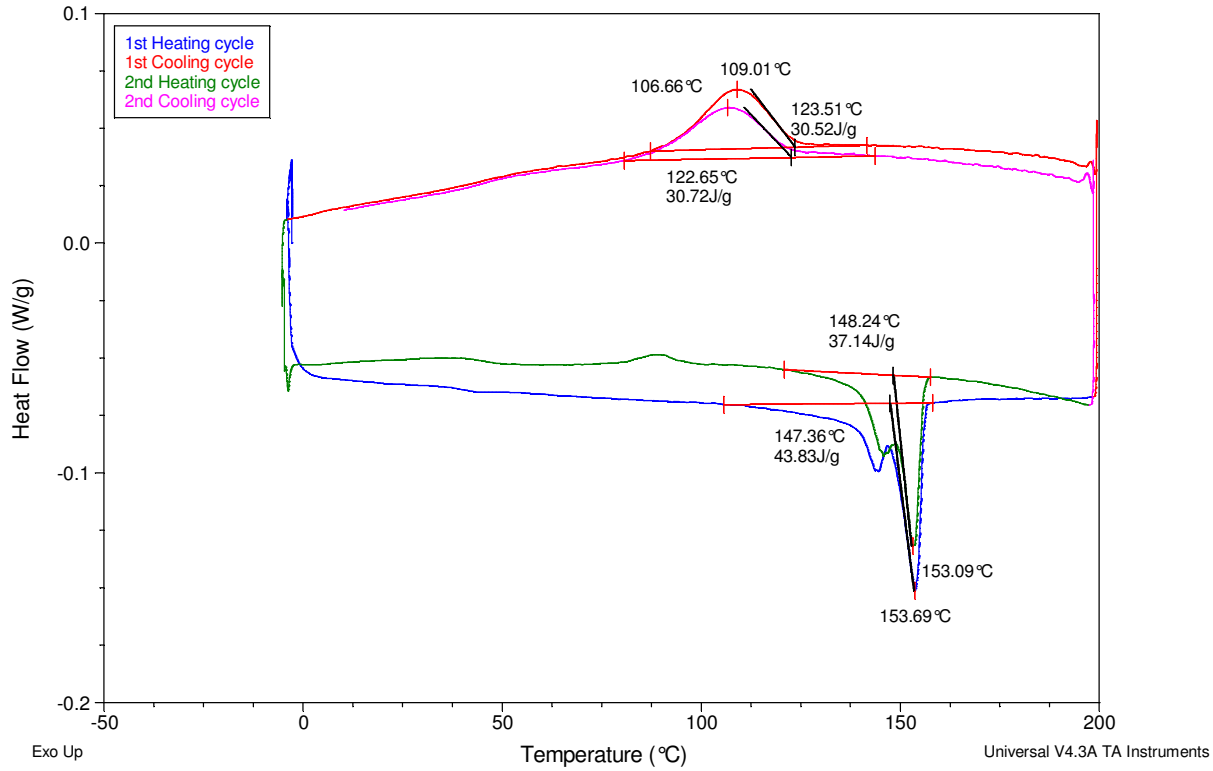

Figure 23. DSC spectrum for sample PLA300-L at slow rate of 1 ˚C/min

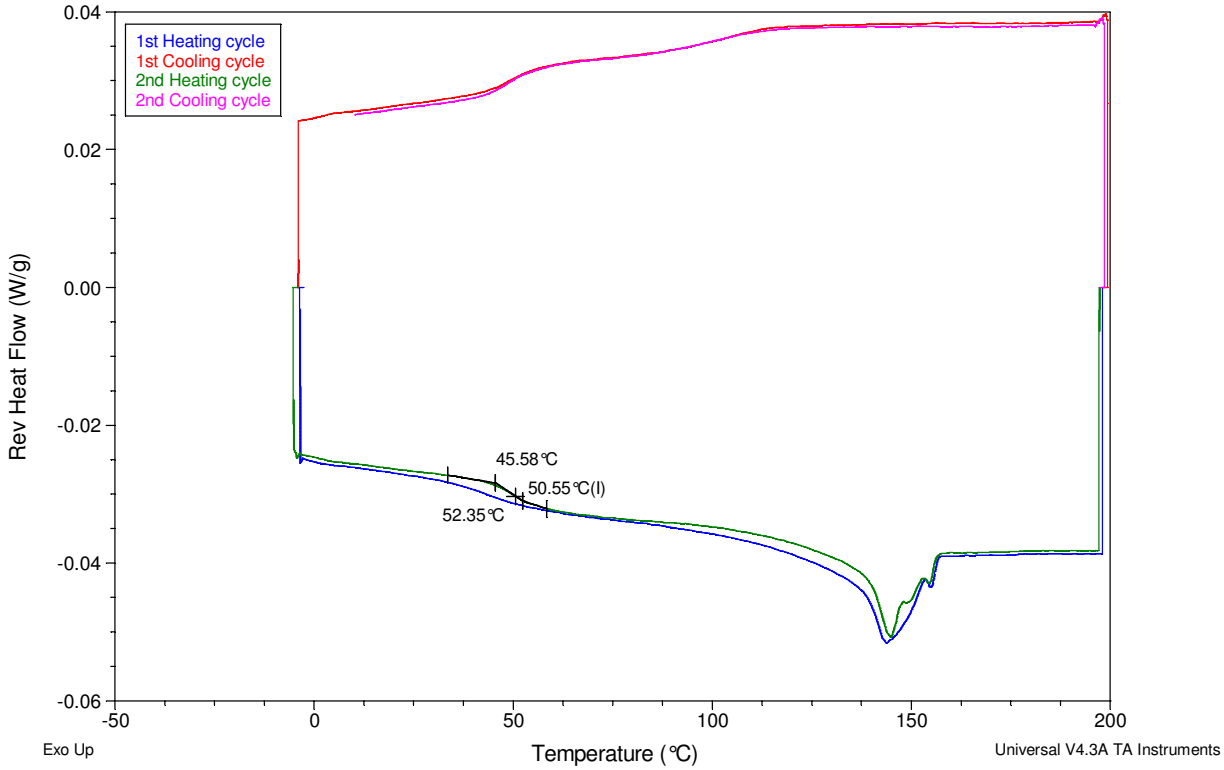

Figure 24. Reversible heat flow spectrum for the sample PLA300-L at slow rate of 1 ˚C/min

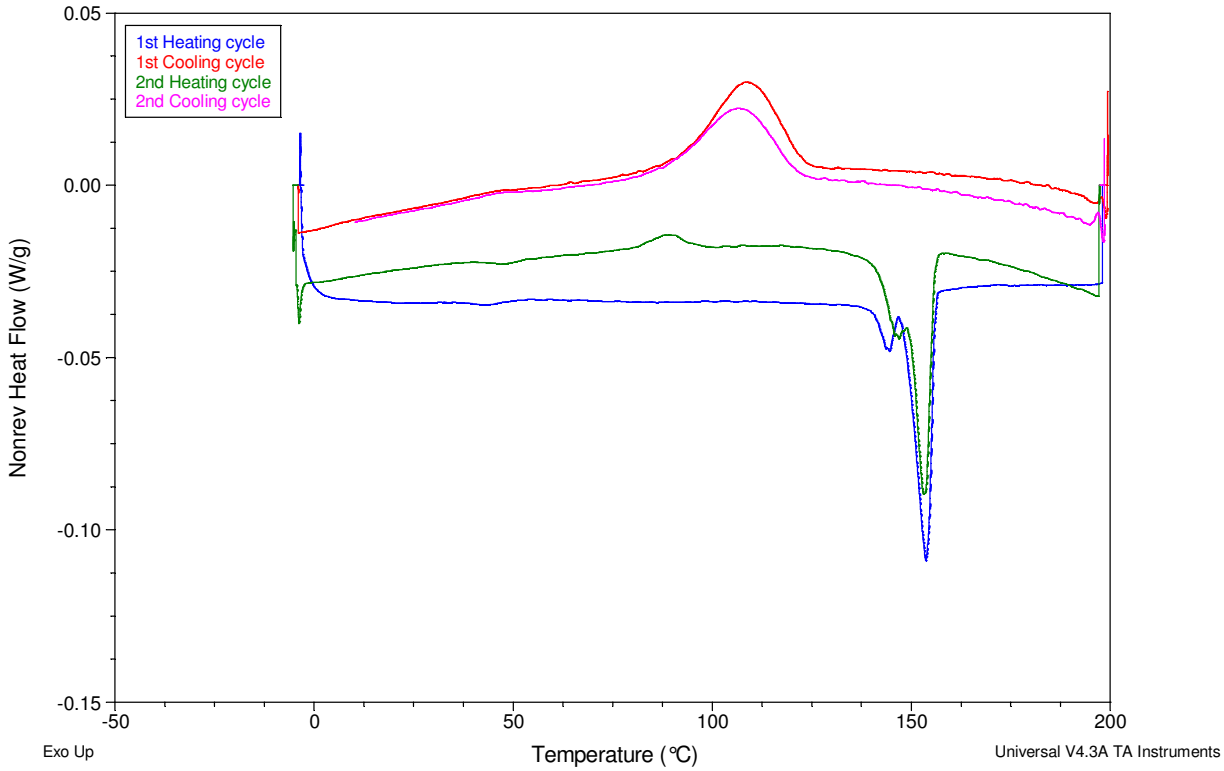

Figure 25. Non-reversible heat flow spectrum for the sample PLA300-L at slow rate of 1 ˚C/min

3.3. PLL inclusion in the PLA networked structure

Crosslinking of PLA in the presence of PLL introduces physical mobility constraints by forming networked structure that will restrict phase separation in the final system [92]. Poly(L-lysine) was recovered from its poly(L-lysine hydrobromide) salt form by neutralizing the ionic charges on the polymer with a base (sodium hydroxide). The extracted solid was tested on FTIR and found to have the characteristic peaks of the PLL. The alternative procedure for extracting PLL using an ion exchange resin was also successful but the yield of recovered product from this procedure was less than that obtained from neutralization.

The obtained PLL was dissolved in methylene chloride and added to a solution of branched PLA to form a homogenous solution of the two polymers. The HDI crosslinker was added to react with the hydroxyl end groups of the PLA forming a network as illustrated in Figure 26.

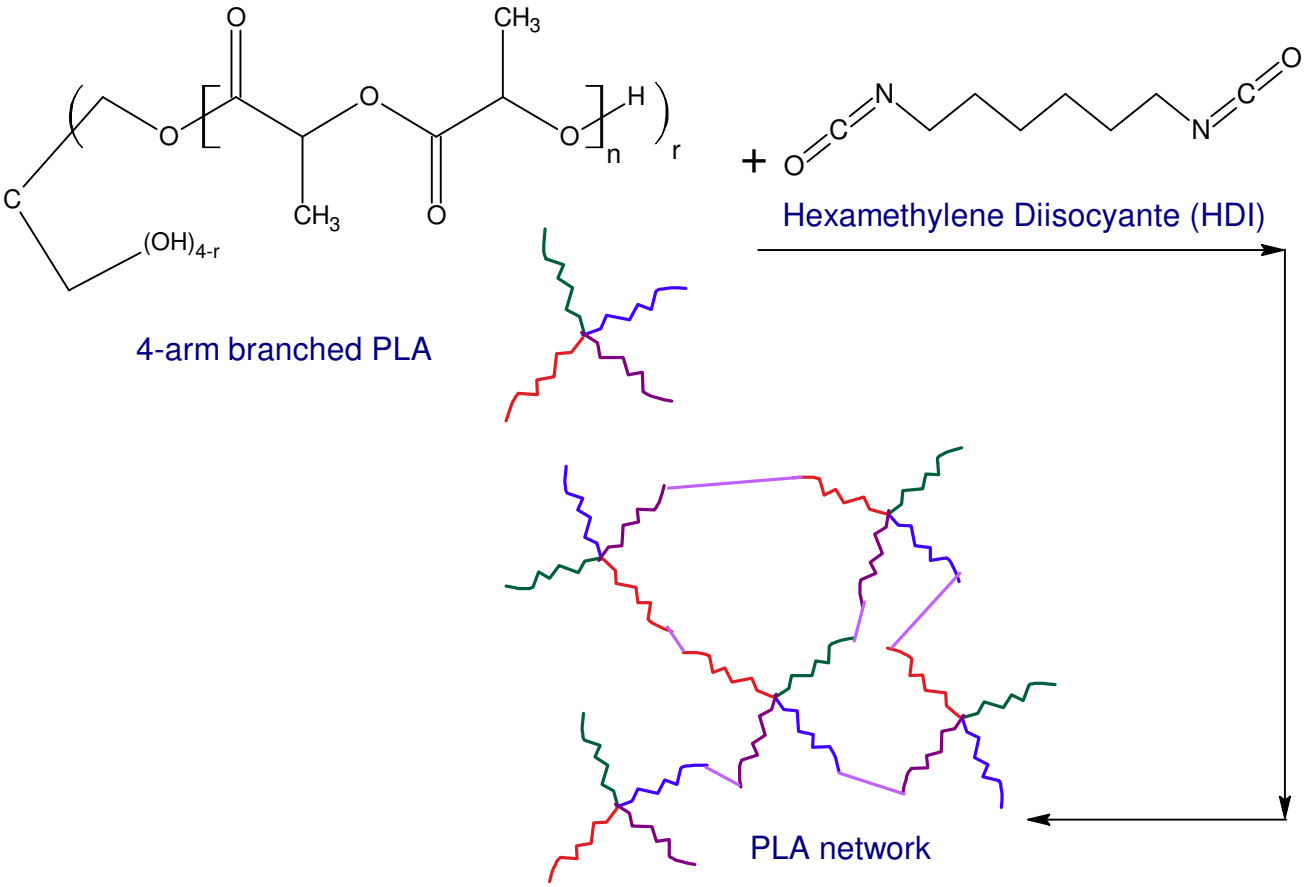

Figure 26. Schematic representation of PLA crosslinking reaction and network formation

The IR vibration of isocyanate group (N=C=O) falls in the range 2300-2270 cm^{-1} [93] and the peak at about 2284 cm^{-1} [94] usually disappears during urethane forming and a new peak around 1700 cm^{-1} begins to form [94]. The crosslinking reaction was monitored by FTIR and the peak formation at 2280 cm^{-1} was observed with time because its strength is proportional to the concentration of the crosslinker in the reactor. Figure 27 shows this peak for the reaction and indicates the consumption of isocyanate in the reaction with time which implies its reaction. Since oxygen is more electronegative than nitrogen, the reaction of isocyanate with hydroxyl end-groups of PLA will occur much faster than the reaction with amine end-groups of PLL and the networked structure will most likely to be PLA rather PLL.

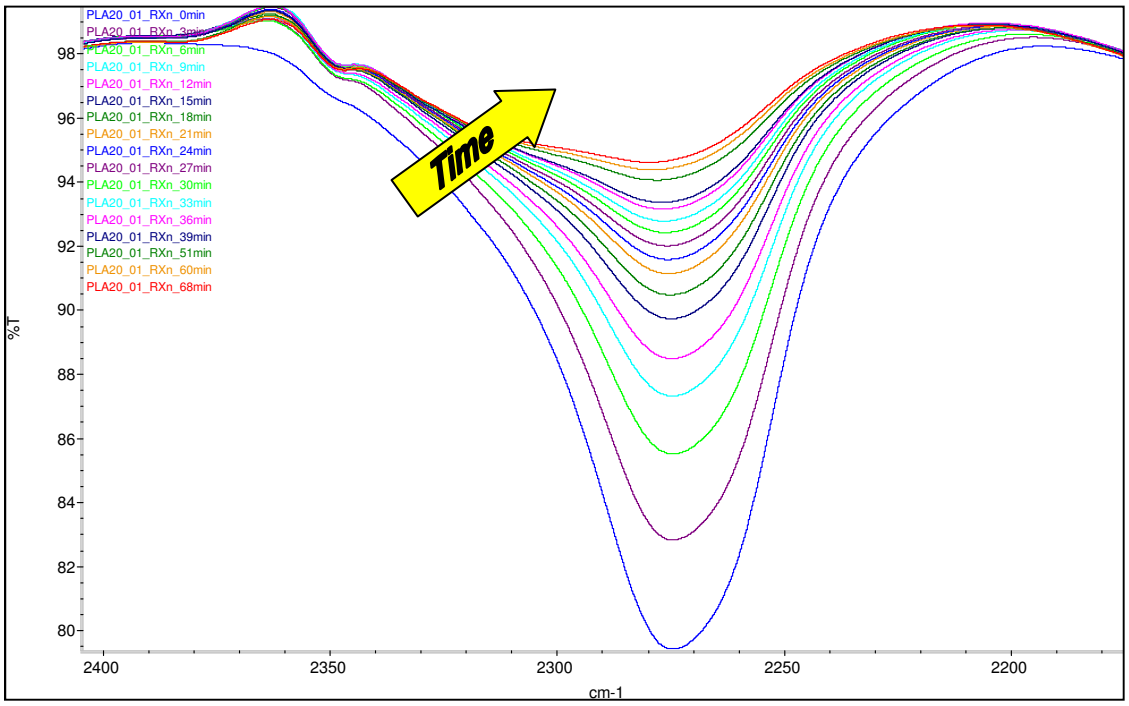

Figure 27. The isocyanate peak as monitored decreasing with time on the FTIR

The peak was noticed to decrease with time in a nonlinear fashion with an initially rapid decrease, slowing with time. Using these spectra, the areas under the peaks were integrated and plotted versus time as shown in Figure 28. The conversion of the reaction (p) was calculated according to the relation:

$$p = \frac{C_A^0 - C_A}{C_A^0}$$

Where C_A^0 is the concentration of the HDI crosslinker at the beginning of the reaction (time = 0 min) and C_A is the concentration of the HDI at a specified time. The calculated conversion after about an hour was 72.25% which implied that running the reaction for about five hours was reasonable to achieve the required crosslinking.

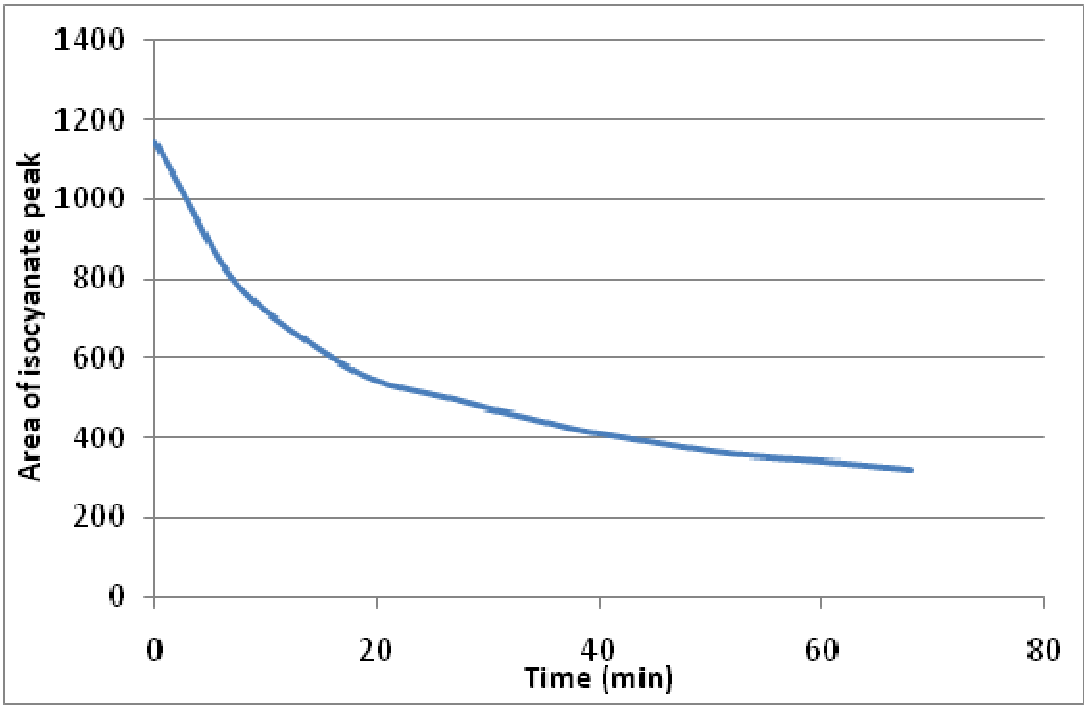

Figure 28. The change in area under the isocyanate peaks with time

4. Conclusion

Samples of PLA were produced in different architectures (linear and branched) using solution-based ring opening polymerization with the use of an organocatalyst. DMF was found to be able to dissolve pentaerythritol initiator at temperatures above 50 ˚C which provided the medium for polymerization to form branched PLA in solution. Application of different initiators to form linear PLA showed that m-cresol was more effective in preparation of PLA with lower dispersity index. The thermal properties of PLA were studied and the crystallization of the polymer chains as investigated by using modulated-DSC showed to occur simultaneously with melting. Neutralization of poly(L-lysine . hydrobromide) salt using a base was found to be effective in recovery of the pure form of PLL and enabled it to dissolve in organic solvents. Monitoring the crosslinking reaction with FTIR indicates the formation of networks from the branched PLA. Finally, although the branching in PLA was directly investigated using ^{1}H NMR, other indirect characterization methods may be required to further investigate the degree of branching and to reveal its effect on the properties of products as well as of subsequently formed crosslinked blends.

Chapter IV: Molecular Modeling for PLA Reaction and Properties

Abstract

The modeling and simulation presented in this chapter aimed to provide a means for predicting the macroscopic properties of polymers based only on their chemical structures. This will help in designing new materials for different applications without the need to synthesize and test these materials. Simulations were performed at electronic and atomistic scales by implementing different methods that represent multiple levels of the theory. Comparing the simulation results with the experimental data obtained from X-ray single crystallography showed that low level methods such as Hartree-Fock (HF) were able to optimize and predict the geometry of molecules with accuracy higher than that obtained with density functional theory (DFT) methods which performed better in predicting the energy and the spectroscopic (IR and NMR) properties for the structures. Increasing the size of the basis sets with DFT did not show much improvement in the prediction accuracy beyond a certain limit and B3LYP/6-311+G(2d,p) method was found to be sufficient for the calculation. The ring opining polymerization reaction for lactide was studied with the goal of predicting the reaction path and calculating its activation energy. Molecular dynamic (MD) simulation was utilized to predict the glass transition temperature (T_g) as a macroscopic property of poly(L-lactide) (PLA) and results showed shifts in the calculated values higher than the experiment. Increasing the simulation time resulted in decreasing the gap between the prediction and the experiment to about 3 ˚C.

1. Introduction

Multiscale modeling and simulation is widely applied for polymeric systems to predict many of their properties based on the knowledge of the chemical structure only [95]. Multiscale methods [96-100] range from electronic/quantum scale [101-103], atomistic/molecular scale [104, 105], meso/micro scale [100], and continuum/macro scale [106]. The advantage of using the electronic (e.g. *ab initio*, density functional theory) and molecular (e.g., molecular dynamics, Monte Carlo) molecular modeling scales is that they provide the ability to understand the behavior of the material bottom-up through the primitive and basic elements of the material [98]. Also, some of these methods do not need any input from experiments to predict material properties [102], and they allow the simulation for systems under controlled and/or inaccessible conditions [97].

The electronic/quantum scale simulation including *ab initio* and density functional theory (DFT) methods was implemented in the literature to study different structural properties of polymers. For example, quantum-based methods were used to study the mechanisms of free radical polymerization and to calculate the kinetics of the reaction with determination of the reaction rates for individual reaction steps [107]. DFT-based calculations were used to trace the changes in the surface electronic structure and energy of fuel cell components [108]. They were used to study the geometric and electronic properties of polyacetylene molecule in different ionic states (neutral, cationic, and anionic) with the influence of external electric field [109].

Atomistic models implementing molecular dynamic (MD) simulation are widely used in studying polymeric systems to predict some of their macroscopic properties such as glass transition temperatures [95], density and solubility parameters of ionic liquids [110], elastic properties [111], gas permeability in amorphous polymers [112]. They were also applied with

branched polymers to determine the effect of modifying the terminal group on the solution properties of the dendrimers [113]. MD simulation was used to study the local and chain dynamics of a polymer melt as well as its thermodynamic and static properties [114], and some other properties such as shear yielding, creep, physical aging, strain hardening and crazing [115].

This work aims at implementing the principles of molecular modeling to theoretically study and model some of the polymeric systems introduced in the previous chapters and to compare theoretical results with the experiments. Geometry optimization and energy calculation of lactide monomer and oligomer was performed using electronic simulation methods. Spectroscopic properties (IR and NMR) were also predicted and compared with the experiments. The ring opining polymerization reaction for poly(L-lactide) (PLA) was studied to understand its steps, determine its pathway, and to calculate its activation energy. The atomistic modeling was then used to predict the glass transition temperature of PLA using MD simulation with different simulation times.

2. Methods

2.1. Electronic modeling

2.1.1. Systems of study

The electronic modeling calculations were performed to study two systems of the lactide monomer (molecular weight of 144.13 g/mole) and the oligomers with two open lactide rings. The oligomer consists of four repeat units with a total molecular weight of 334.32 g/mol after the addition of the ethanol to the beginning of the chain as it initiates the ring opening. The electronic simulations were performed using the Hartree-Fock (HF) method [116] as well as the

density functional theory where different levels of the theory were applied. All electronic modeling calculations were performed using Gaussian 09 software [117].

2.1.2. Hartree-Fock calculations

Based on the principles of quantum mechanics, the energy and other related properties of a molecule may be obtained by solving the Schrödinger equation:

$$\widehat{\mathcal{H}}\Psi = E\Psi$$

Where: Ψ is the wavefunction, $\widehat{\mathcal{H}}$ is the Hamiltonian operator that can be expressed as:

$$\widehat{\mathcal{H}} = \sum_{i=1}^{2n} -\frac{1}{2}\nabla_i^2 - \sum_{\text{all } \mu,i} \frac{Z_\mu}{r_{\mu i}} + \sum_{\text{all } i,j} \frac{1}{r_{ij}}$$

Which represents the summations of (from left to right) electron kinetic energy terms, nucleus-electron attraction potential energy terms, and electron–electron repulsion potential energy terms. The energy levels of the molecule *E* can be calculated by finding the eignvalues of the system as:

$$E = \frac{\int \Psi^* \widehat{\mathcal{H}} \Psi \, d\tau}{\int \Psi^* \Psi \, d\tau}$$

The Hartree-Fock (HF) method can computationally solve this equation which can turn, after some tedious algebraic manipulations, to the following expression:

$$E = 2\sum_{i=1}^{n} H_{ii} + \sum_{i=1}^{n}\sum_{j=1}^{n}(2J_{ij} - K_{ij})$$

With; H_{ii} representing the electronic energy (including the $\widehat{H}^{core}$ operator), J_{ij} the coulomb integral, and K_{ij} the exchange integral. To use this method to solve the Schrödinger

equation for molecules, basis functions are required to mathematically represent the molecular orbitals within a molecule. The size of the applied basis sets determines the accuracy of this mathematical representation as well as the resources required to solve the problem. In this work, different basis sets were applied during the simulation where the 6-31G(d) basis set was used for the HF low level calculations. This basis set includes six primitive base functions of Gaussian type that were used with a double zeta split on the valence shell and with polarized basis set of d type applied for every heavy atom [118].

Hartree-Fock method was applied to optimize the structures of the lactide monomer and the PLA oliogmer. Frequency analysis was then performed on the optimized structures to obtain their IR spectra, zero point energy (ZPE), and to check the state of the optimized structures to determine if they are minimum points on the potential energy surface (PES) or they are saddle points [119]. Finally, NMR calculation procedure was applied on the optimized structures to produce their NMR spectra.

2.1.3. Density functional theory

In the previously described Hartree-Fock and other *ab initio* methods, most of the calculations are required to determine the wavefunctions for the molecules while these wavefunctions neither exist physically nor can be measured. Therefore, density functional theory (DFT) was introduced based on the electron probability density function $\rho(x, y, z)$ which can be measured using X-ray or electron diffractions [120]. DFT provides the results quality for some computationally expensive *ab initio* methods with the low resources required for HF method [120, 121]. The method of Kohn-Sham (KS) self consistent equations [122] is implemented in the DFT calculations and can be expressed as:

$$\left[-\frac{1}{2}\nabla_{\mathrm{i}}^{2}-\sum_{\text{nuclei A}}\frac{Z_A}{r_{1A}}+\int\frac{\rho(r_2)}{r_{12}}\,dr_2+\upsilon_{XC}(1)\right]\Psi_i^{KS}(1)=\epsilon_i^{KS}\Psi_i^{KS}(1)$$

Where Ψ^{KS} is the KS spatial orbitals, and $v_{xc}(r)$ is the exchange correlation potential which can be expressed as:

$$\upsilon_{XC}(r)=\frac{\delta\,E_{XC}[\rho(r)]}{\delta\,\rho(r)}$$

The exchange-correlation energy functional $E_{xc}[\rho(r)]$ has different forms, among them is the B3LYP which includes Beck3 exchange function with the Lee–Yang–Parr (LYP) correlation function (hence, assigned the name B3LYP) [123]. B3LYB is a hybrid functional with terms calculated from the HF theory and others based on the DFT and can be expressed as:

$$E_{XC}^{B3LYP}=(1-a_0-a_x)E_X^{LSDA}+a_0E_X^{HF}+a_xE_X^{B88}+(1-a_c)E_c^{VWN}+a_cE_c^{LYP}$$

In the current work, a sequence of optimization, frequency analysis, and NMR analysis was performed on the lactide monomers and oligomers using the DFT higher level calculations. Three basis sets were applied during the calculations where 6-311G(d) basis set was applied (calculations were assigned the name DFT-1) with triple split in the valence shell. The second basis set (assigned the name DFT-2) was the 6-311+G(2d,p) where diffusion functions were applied on heavy atoms and two polarized functions of d type were applied on heavy atoms and one polarized function of p type was applied on hydrogen atoms of the simulated structure. The third (assigned the name DFT-3) basis set was the 6-311++G(3df,3pd) where extra diffusion and polarization were considered for hydrogen atoms [118].

2.1.4. Reaction mechanism

To understand the mechanism of the ring opening polymerization reaction, the reactants and the products were optimized using the HF/6-31G(d) method. A search for the transition structure (TS) was then applied by providing the optimized reactants and products as well as a starting guess for the TS to the procedure. The intrinsic reaction coordinate (IRC) procedure was then applied by starting from the obtained TS toward the suggested optimized reactants and products to verify the reaction pathway, find the reaction coordinate, and to determine the activation energy of the reaction.

2.1.5. X-ray single crystallography

To measure the exact geometry of the lactide monomer for comparing with the geometries obtained from the simulations, X-ray single crystallography was conducted on a Bruker SMART APEX diffractometer. The instrument is a charge-coupled device (CCD) with area-detector equipped with monochromated Mo Ka, with a wave length λ = 0.71073 Å and operated at 2 KW power (50 kV, 40 mA). The X-ray intensities were measured at temperature of 273(2) K. The unit cell parameters were adjusted to have orthorhombic cell, space group P21. Cell dimensions were a = 9.2653(6) Å, b = 13.4991(8) Å, c = 16.7023(10) Å, angles were set to $\alpha = \beta = \gamma = 90^{\circ}$, volume = 2089.0(2) $Å^3$, and Z = 12. The absorption correction coefficient μ = 0.117 mm^{-1}. A total of 5,172 frames were collected during the sample run. The structure was solved by direct methods and the subsequent difference Fourier syntheses on SHELXS-97 and refined with the SHELXL-97 software package.

2.2. Atomistic modeling

The focus in the electronic modeling methods was on calculating the properties of the molecule based on the study of the energy levels and movement of electrons in the structure. Atomistic modeling, on the other hand, deals with the whole atoms as balls (particles) that are connected with springs (bonds) and the study focuses on a scale larger than that considered in electronic modeling.

Molecular dynamics simulation was applied in this work to study glass transition as a macroscopic property of PLA. MD allows the prediction of the time evolution for a system of interacting particles by solving a set of Newton equations of motion [100]:

$$\overrightarrow{F_i}(t) = m_i \frac{\mathrm{d}^2 \overrightarrow{r_i}}{\mathrm{d}t^2}$$

Where; $\overrightarrow{F_i}$ is the force acting on the i^{th} particle with a mass m_i and atomic position $\overrightarrow{r_i}$. The force can be obtained from the negative gradient of the interaction potential ($\overrightarrow{F_i} = -\nabla_i U$) after the calculation of U using a certain set of functions and parameters that are known as the force field. CHARMM (Chemistry at Harvard using Molecular Mechanics) [124] force field was used in the current study where the interaction function can be described as [125]:

$$U_{total} = U_{intramolecular} + U_{intermolecular}$$

$$U_{intramolecular} = \sum_{bonds} K_b(b - b_0)^2 + \sum_{angles} K_\theta(\theta - \theta_0)^2 + \sum_{torsions} K_\phi(1 + \cos(n\phi - \delta)) + \sum_{impropers} K_\varphi(\varphi - \varphi_0)^2 + \sum_{Urey-Bradley} K_{UB}(r_{1,3} - r_{1,3,0})^2$$

$$U_{intermolecular} = \sum_{electrostatics} \frac{q_i q_j}{r_{ij}} + \sum_{VDW} \varepsilon_{ij} \left[\left(\frac{R_{min,ij}}{r_{ij}} \right)^{12} - 2 \left(\frac{R_{min,ij}}{r_{ij}} \right)^{6} \right]$$

Where the equilibrium terms are: b_0 for bond lengths, θ_0: for angles,$r_{1,3,0}$: Urey-Bradley, ω_0: impropers, n_0: dihedral multiplicity, and δo: for dihedral phase. The force constants are: K_b: for bonds, K_θ: angles, K_{UB}: Urey-Bradley, Kω: impropers, and K_ϕ: for dihedral. The intermolecular terms are: ε: for Lennard-Jones well-depth, R_{min}: L-J radius ($R_{min}/2$ in CHARMM), and q_i: for partial atomic charge. The combining rules are: $R_{min\,i,j} = R_{min,i} + R_{min,j}$, and $\varepsilon_{i,j} = \sqrt{(\varepsilon_i * \varepsilon_j)}$.

To perform the simulation, an amorphous cell of the poly(L-lactide) was built including four chains with 20 repeat unites per chain. This creates a system with molecular mass of about 11990.7 g/mol. The cell was optimized and equilibrated at a temperature of 273 K and pressure of 1 atm using the isobaric-isothermal ensemble (NPT) for 0.1 ns simulation time. The density of the system in the cell was adjusted during this simulation to approach the experimental value for PLA. The integration of the equation of motion was performed using Verlet algorithm with 1 fs time step and the initial velocities of the atoms were assigned using a Maxwell-Boltzmann distribution at that temperature.

Simulated annealing procedure was then performed on the system by ramping up the temperature from 273 K to 500 K with a heating rate of 1 K/ns. During the heating cycle, the system was allowed to equilibrate for 0.1 ns at each temperature step. The molecular cell was then equilibrated at 500 K for 0.1 ns then cooled down to 273 K with -1 K/ns cooling rate. The particle mesh Ewald (PME) sum was used for calculating the long range electrostatic interactions in the periodic system.

The Langevin piston Nosé-Hoover method was used to control the pressure with oscillation time constant of 100 fs and a damping time of 50 fs for the Langevin piston. This

method is a combination of the Nose-Hoover constant pressure method [126] with Langevin dynamics method implementing piston fluctuation control [127]. Langvin dynamics was used to control the kinetic energy of the system which results in controlling both the temperature and pressure during the simulation [128]. NAMD software package [129] was used for all MD simulation and the results were analyzed using Tcl programming language within the consoles of VMD visualization software [130].

The above outlined procedure for simulated annealing was repeated on the system with different total simulation times. The initial simulation was performed by scaling that procedure to have a total time of 500 ps (0.5 ns). A second simulation was performed with a total time of about 45.6 ns then a third simulation (detailed in the previous paragraphs) was extended to about 456 ns (≈0.5 microseconds). The longer times are required to approach the limits of relaxation time of polymer chains which are in the millisecond range as reported in the literature.

3. Results and Discussion

3.1. Geometry optimization and energy calculations

The geometry of the lactide monomer was optimized at different levels of the theory using HF and DFT with different basis sets as described before. Geometries of the optimized structures were compared to the experimental geometry obtained from the X-ray single crystallography which is shown in Figure 29. The root mean square error (RMSE) was used as an indicator for the convergence or divergence of the optimized structures from the actual structure obtained from the experiments. The RMSE can be expressed as:

$$RMSE = \sqrt{\frac{\sum(\vec{r_i} - \vec{r_0})^2}{N}}$$

Where; $\vec{r_i}$ refers to the vector of optimized values for the measured property (i.e. bond, angle, or dihedral), $\vec{r_0}$ is the vector for the corresponding experimental values, and N is the number of readings for each property.

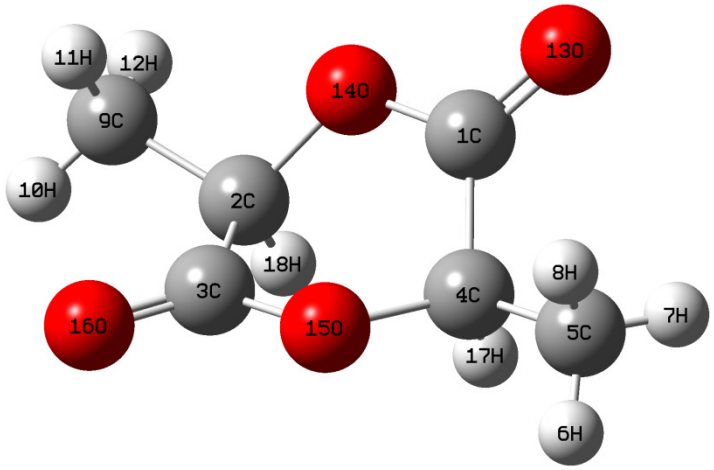

Figure 29. The structure of the lactide monomer as obtained from the X-ray single crystallography

The bond lengths, angles, and dihedrals for the experimental structure as well as the structures obtained from the different optimization methods are given in Table 9 in the form of Z-matrices. The RMSE value for each method is also given at the last two rows of the table.

Based on the results given in Table 9, it is noticed that the low level calculation using HF method is able to predict the geometry of the structure reasonably with accuracy higher than other methods. This high accuracy is indicated with the low RMSE for HF methods in bond lengths and dihedrals. The RMSE was generally high for dihedrals with all methods which can be attributed to the sign change in the dihedral angle for oxygen atom (number 14) and the hydrogen atom (number 6), although the HF calculation was able to predict the correct sign for the last atom. These results agree with the known ability of HF method to predict the geometry [118, 131] although HF may not be the best choice for calculating the energy of the molecule. The reason for HF to have a high deviation from the experimental value for the energy is the lack of calculating the electron-electron interaction during the calculation [118].

Table 9. Geometries of the experimental and the optimized lactide monomer

Atom#	Symbol	NA	NB	NC	Experimental (X-rays)			Predicted using HF			Predicted using DFT-1[a]		
					Bond (Å)	Angle (˚)	Dihedral (˚)	Bond (Å)	Angle (˚)	Dihedral (˚)	Bond (Å)	Angle (˚)	Dihedral (˚)
1	C												
2	C	1			2.39[*]			2.38			2.41		
3	C	2	1		1.50	88.28		1.52	89.58		1.53	89.53	
4	C	1	2	3	1.51	82.37	40.87	1.52	84.07	33.70	1.53	82.99	36.70
5	C	4	1	2	1.49	113.63	-167.36	1.51	112.77	-161.98	1.51	112.95	-164.06
6	H	5	4	1	0.96	109.56	177.26	1.08	109.38	179.91	1.09	109.84	-179.34
7	H	5	4	1	0.96	109.47	-62.72	1.08	109.97	-59.85	1.09	109.97	-59.03
8	H	5	4	1	0.96	109.52	57.20	1.08	110.30	60.07	1.09	110.47	60.46
9	C	2	1	4	1.51	136.35	162.43	1.51	136.19	157.17	1.51	136.59	160.67
10	H	9	2	1	0.96	109.45	-174.05	1.08	109.97	-175.07	1.09	109.97	-174.79
11	H	9	2	1	0.96	109.46	-54.10	1.08	110.30	-55.15	1.09	110.47	-55.30
12	H	9	2	1	0.96	109.51	65.94	1.08	109.38	64.69	1.09	109.84	64.90
13	O	1	4	5	1.20	124.76	13.31	1.18	123.70	24.15	1.20	124.18	19.95
14	O	1	13	4	1.34	120.24	177.80	1.33	121.52	-179.55	1.35	121.11	-179.78
15	O	3	2	1	1.34	115.64	-19.84	1.33	114.78	-15.05	1.35	114.70	-18.49
16	O	3	2	1	1.20	124.63	158.03	1.18	123.70	165.38	1.20	124.18	161.71
17	H	4	1	13	0.98	109.17	-108.76	1.09	107.63	-97.28	1.10	107.77	-101.74
18	H	2	1	13	0.98	97.69	110.17	1.09	97.12	95.19	1.10	96.37	101.67
RMSE					**0**	**0**	**0**	**0.08**	**0.94**	**92.51**	**0.09**	**0.83**	**130.45**
Energy of the molecule (Hartree)						**-534.432**			**-531.339**			**-534.497**	

[*] This value refers to the distance between atoms #1 and #2 while there is no bond between these atoms.

[a] Values as obtained from DFT calculation using 6-311G(d) basis set.

Continue to Table 9

Atom#	Symbol	NA	NB	NC	Predicted using DFT-2 [b]			Predicted using DFT-3 [c]		
					Bond (Å)	Angle (°)	Dihedral (°)	Bond (Å)	Angle (°)	Dihedral (°)
1	C									
2	C	1			2.41			2.41		
3	C	2	1		1.53	89.47		1.53	89.48	
4	C	1	2	3	1.53	83.18	36.40	1.53	83.23	36.24
5	C	4	1	2	1.51	113.07	-163.99	1.51	113.03	-163.84
6	H	5	4	1	1.09	109.70	-179.06	1.09	109.70	-179.09
7	H	5	4	1	1.09	109.73	-58.88	1.09	109.71	-58.91
8	H	5	4	1	1.09	110.49	60.61	1.09	110.46	60.57
9	C	2	1	4	1.51	136.68	160.55	1.51	136.64	160.30
10	H	9	2	1	1.09	109.73	-174.80	1.09	109.71	-174.73
11	H	9	2	1	1.09	110.49	-55.31	1.09	110.46	-55.26
12	H	9	2	1	1.09	109.70	65.02	1.09	109.70	65.08
13	O	1	4	5	1.20	124.18	20.23	1.20	124.24	20.36
14	O	1	13	4	1.35	120.92	-179.61	1.35	121.00	-179.58
15	O	3	2	1	1.35	114.89	-18.24	1.35	114.76	-18.21
16	O	3	2	1	1.20	124.18	162.13	1.20	124.24	162.18
17	H	4	1	13	1.10	107.50	-101.30	1.10	107.40	-101.05
18	H	2	1	13	1.10	96.43	101.31	1.10	96.62	101.31
RMSE					**0.09**	**0.82**	**130.38**	**0.09**	**0.82**	**130.38**
Energy of the molecule (Hartree)					**-534.534**			**-534.561**		

[b] Values as obtained from DFT calculation using 6-311+G(2d,p) basis set.

[c] Values as obtained from DFT calculation using 6-311++G(3df,3pd) basis set.

On the other hand, the molecular energy calculated with DFT methods show a reasonable agreement with the energy calculated for the structure obtained from the X-ray experiment. This result indicates that DFT is not sensitive to the level of geometry optimization and it is robust to calculate the energy of the molecule with little geometry inaccuracy. Results also show that computationally expensive methods are not usually the most accurate ones and an increase in the number of basis sets may not have the same weight in optimizing the geometry as it does in calculating the energy of the molecule.

Results of different calculation methods as well as the experiments show that an equatorial conformation of the pendent methyl groups was preferred in the lactide monomer. To verify this result a scan for the potential energy surface (PES) was performed by changing the angle of the pendent methyl groups from axial conformation to equatorial conformation. The DFT-1 calculation method was applied during this scan to optimize and calculate the energy of the molecule as it was found in the previous results to be an efficient method. Results for this scan are shown in Figure 30 which indicates a high energy of the molecule in the case of axial conformation (steps No. 1 to 4 in the figure) while this energy was decreased and the molecule became more stable after changing to the equatorial conformation (steps No. 6 and 7 on the graph). The lactide was also observed in the experimental results as well as the optimized structures to have the boat conformer as a stable conformation. This conformation is unlike the preferred chair conformer for other six member rings such as cyclohexane [132]. The reasons for the instability of chair over the boat conformation might be attributed to the larger deformations of valence angles and torsional strains in the case of lactide chair conformation [133].

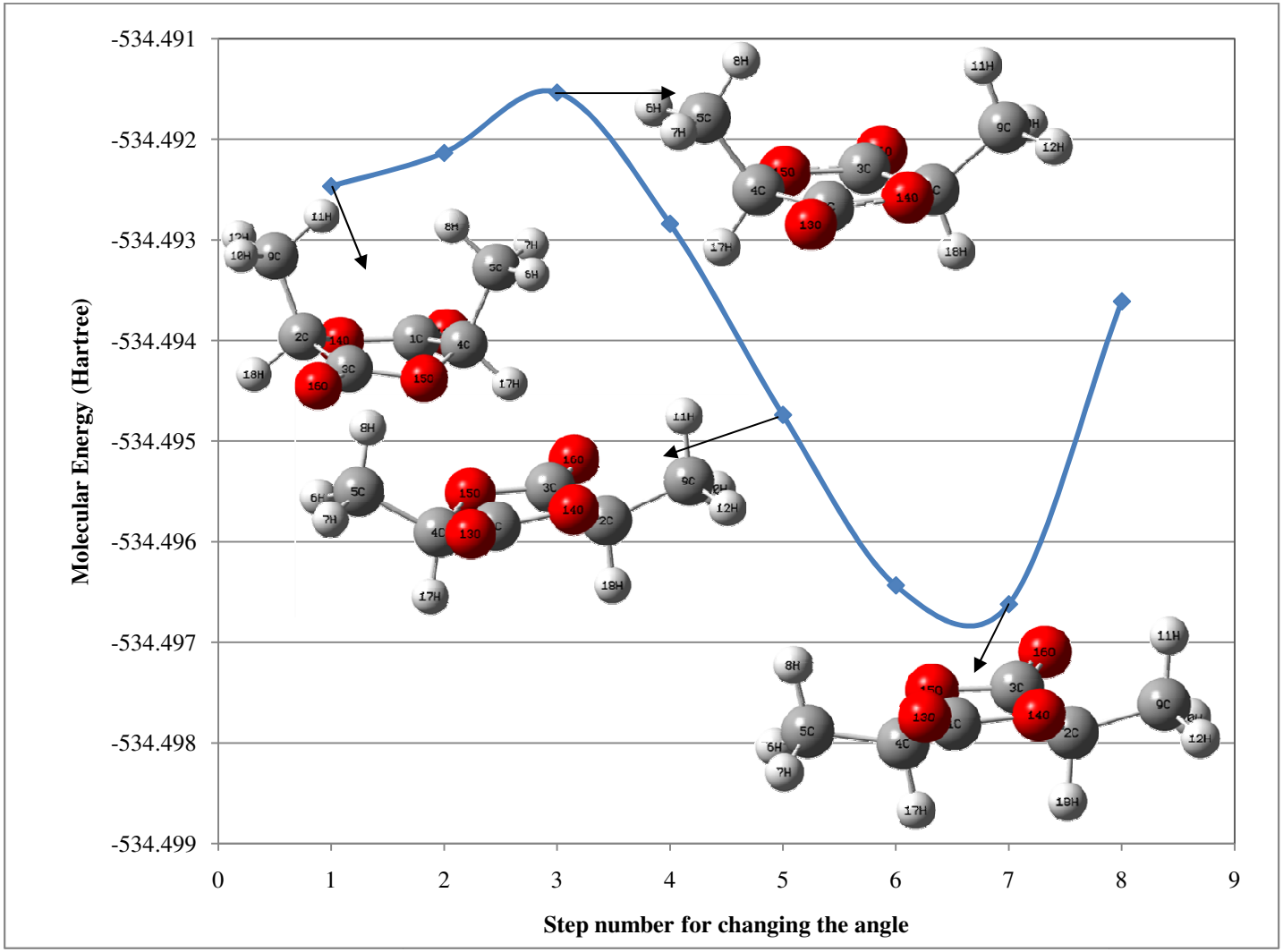

Figure 30. Potential energy surface (PES) scan for the change in the molecular energy with the change in the conformation of pendent methyl group from axial to equatorial

3.2. IR and NMR spectroscopy

The predicted IR vibrational spectrum for the lactide monomer is shown at the lower part of Figure 31 as compared to the experimental spectrum of the molecule shown at the top part of the figure. The given spectrum was calculated using DFT-3 calculation (with the highest basis sets) and it was the closest to the experiment even without the application of the correction factors. The other calculated spectra showed the same general trend of peaks but with shifting of the peak at *ca.* 1750 cm^{-1} toward higher values. These peak shifts may lie in an acceptable range from the experimental values after the application of the recommended correction factors [118]. The spectrum of the lactide oligomer is shown in the lower part of Figure 32 as calculated from DFT-2 method and compared to the experimental spectrum of PLA in the same figure. The calculated spectrum showed a doublet peak for the carbonyl group at *ca.* 1750 cm^{-1} which was also noticed in the results of the other calculation methods.

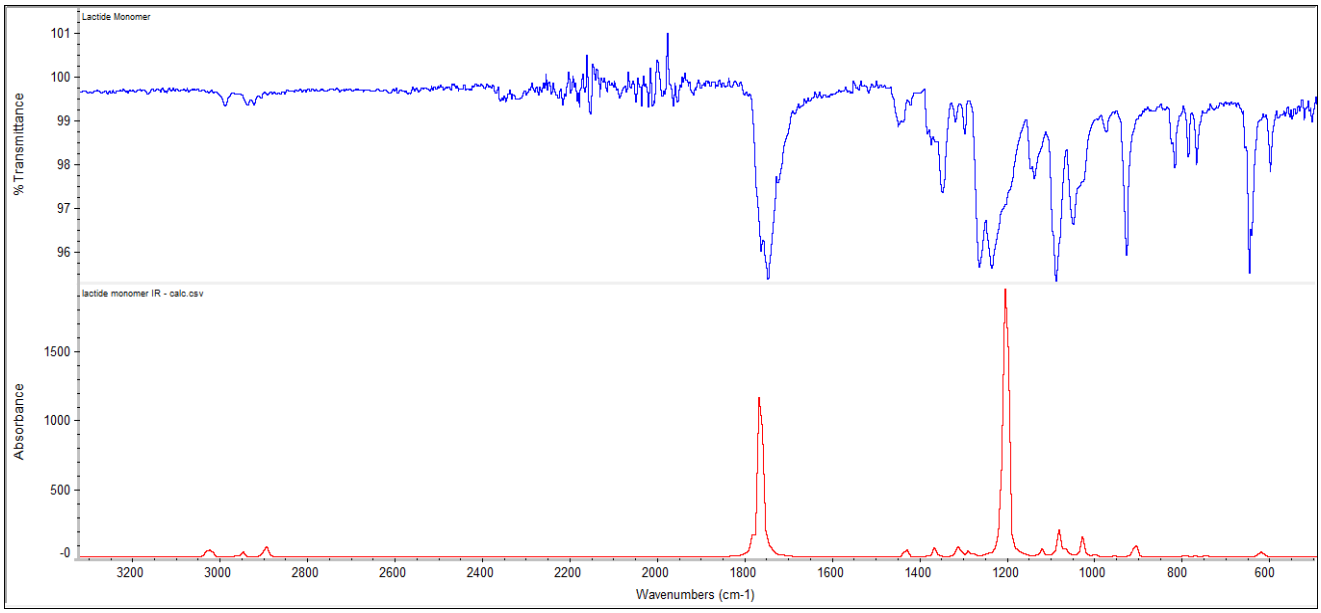

Figure 31. FTIR spectra for the lactide monomer as measured experimentally (top) and as predicted from DFT-3 calculations (bottom)

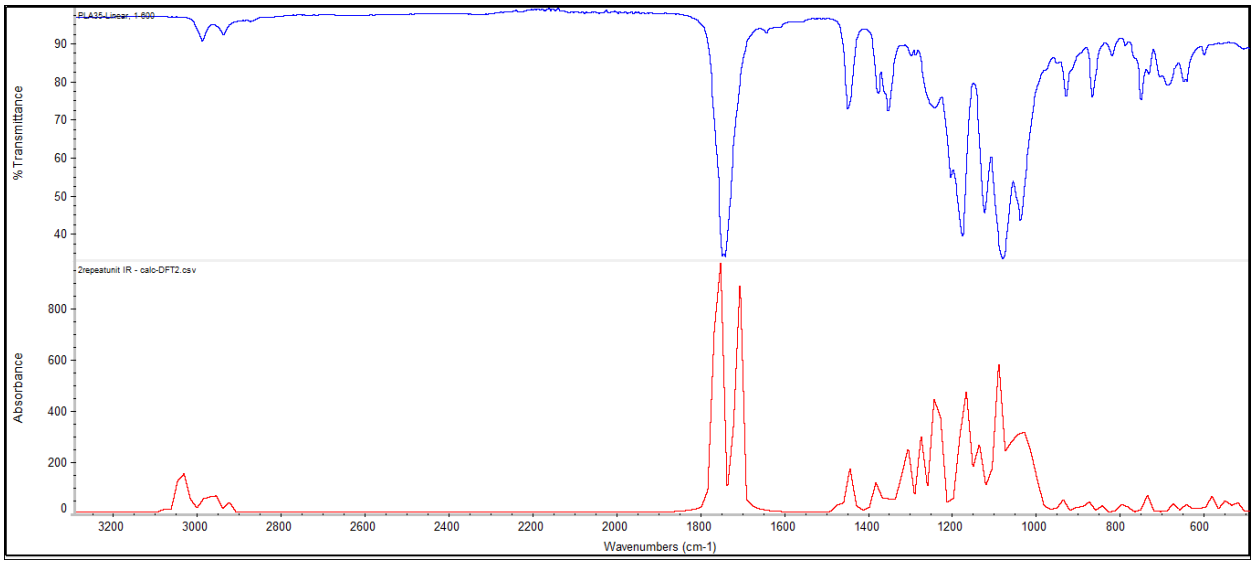

Figure 32. The measured FTIR spectrum for PLA (top) and the predicted spectrum of the PLA oligomer (bottom)

Investigating the double peak behavior in the calculated spectra indicates two vibrational modes for the carbonyl groups based on their position in the chain. Carbonyl groups that are located closer to the end of the chain showed different frequency than the groups located on the backbone of the chain which results of this double peak. Also, since the simulation was performed on a small molecule (oligomer) the peak strength was close for both modes especially when compared to the tested polymer which has a relatively higher molecular weight that weaken this effect.

The predicted proton nuclear magnetic resonance (^{1}H NMR) spectrum for lactide monomer is shown in Figure 33 which is reasonably comparable to the experimental spectrum of the molecule shown in Figure 34. The calculated spectra predicted the chemical shift $\delta \approx 1.8$ for the six protons on the two methyl groups, as shown by degeneracy value of 2 with three peaks. The chemical shift at $\delta \approx 5.1$ corresponds to the protons on the alpha carbons in the molecule.

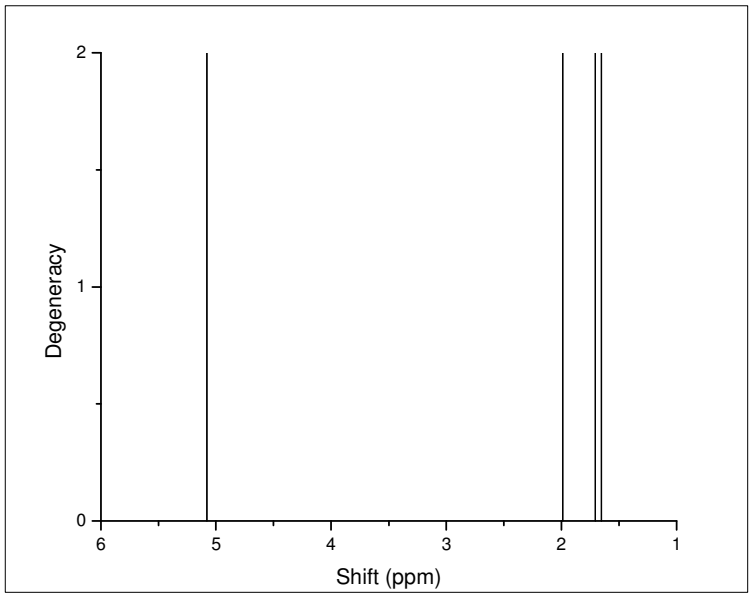

Figure 33. ^{1}H NMR spectrum for lactide monomer calculated using DFT-3

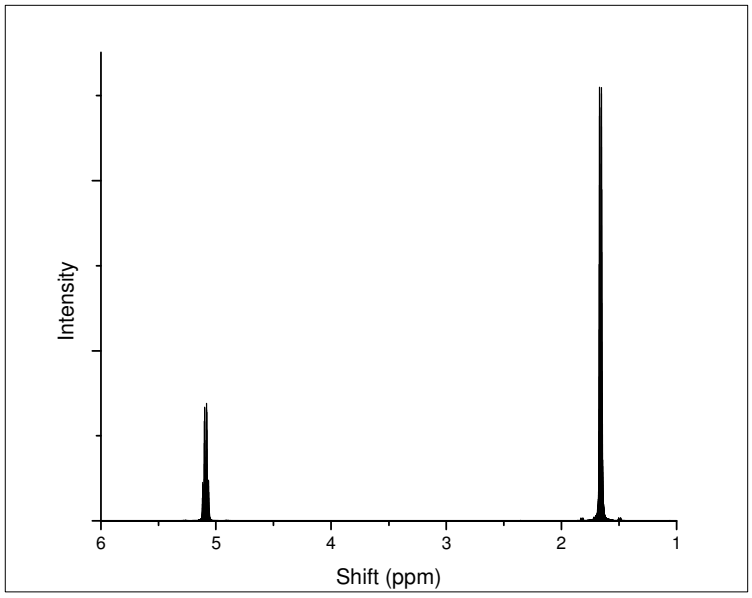

Figure 34. The measured ^{1}H NMR spectrum for the lactide monomer

The spectrum of the lactide oligomer as obtained from the simulation predicted peaks in a reasonably agreement with the chemical shift values obtained from the experiments. The small number of repeat units during the simulation (four repeat units), however, made it hard to show the comparison with the actual polymer with high molecular weight (more repeat units). Based on the obtained results, DFT calculation methods performed better than the HF method in predicting the IR and NMR spectra for the monomer as well as the oligomer and the accuracy increased with the size of the basis set giving a better match in the following order: DFT-3 > DFT-2 > DFT-1 > HF.

3.3. Reaction mechanism

Calculating the pathway of the reaction required the application of a search procedure to find the transition structure(s). Searching for TS was implemented by using a starting guess that was chosen based on the mechanism for ring opening polymerization suggested by Nederberg *et al* [67] as was described in the previous chapter of this work. A frequency calculation procedure was performed on all of the optimized structures (reactants, products, and TS) which helped on verifying the TS by checking its frequency levels. Transition structures are identified as first order saddle points that have one imaginary (negative) frequency. The absence of this condition may imply that the obtained structure is a stationary point which may be a minimum or saddle point of higher order [118]. Besides being helpful in verifying the TS, frequency calculations are required to determine the zero-point energy required for calculating the thermodynamics of the reaction and also to generate the force constant data needed during the intrinsic reaction coordinate (IRC) calculations.

The IRC calculations showed that the suggested product structure (structure No. 2 in Figure 35) may not be located on the correct reaction pathway as it has energy higher than the transition structure (structure No. 3 on Figure 35). A further optimization of the TS structure led to locating another structure which might be the product (structure No. 4 in Figure 35) as it has energy lower than that for the TS. The optimized product (structure No. 2) showed a tactic structure with pendent methyl groups aligned in the same direction while the found structure for the product (structure No. 4) showed an isotactic structure. It can be noticed that structure No.4 is very close to the TS (structure No. 3) where the only change can be found in the conformation of the end methyl group that turned from the eclipsed conformation in the TS to the staggered conformation in the product which helped to relief some of the torsional energy in the molecule.

Based on the given structures and the suggested reaction pathway the activation energy of the reaction can be calculated after considering the zero-point energy (ZPE) and the thermal energy corrections. The calculated activation energy was found to be 65.81 Kcal/mol as the difference between the energies of the reactants and the TS and found to be 3.41 Kcal/mol as the difference between the energies for the TS and the products. The relatively high activation energy of the reaction to go from reactants to the TS indicates the need of the catalyst in the reaction to proceed and explains some of the experimental observations for this reaction which only takes place at relatively high temperatures with organometallic catalyst (or organic catalyst) as described in chapter III of this work.

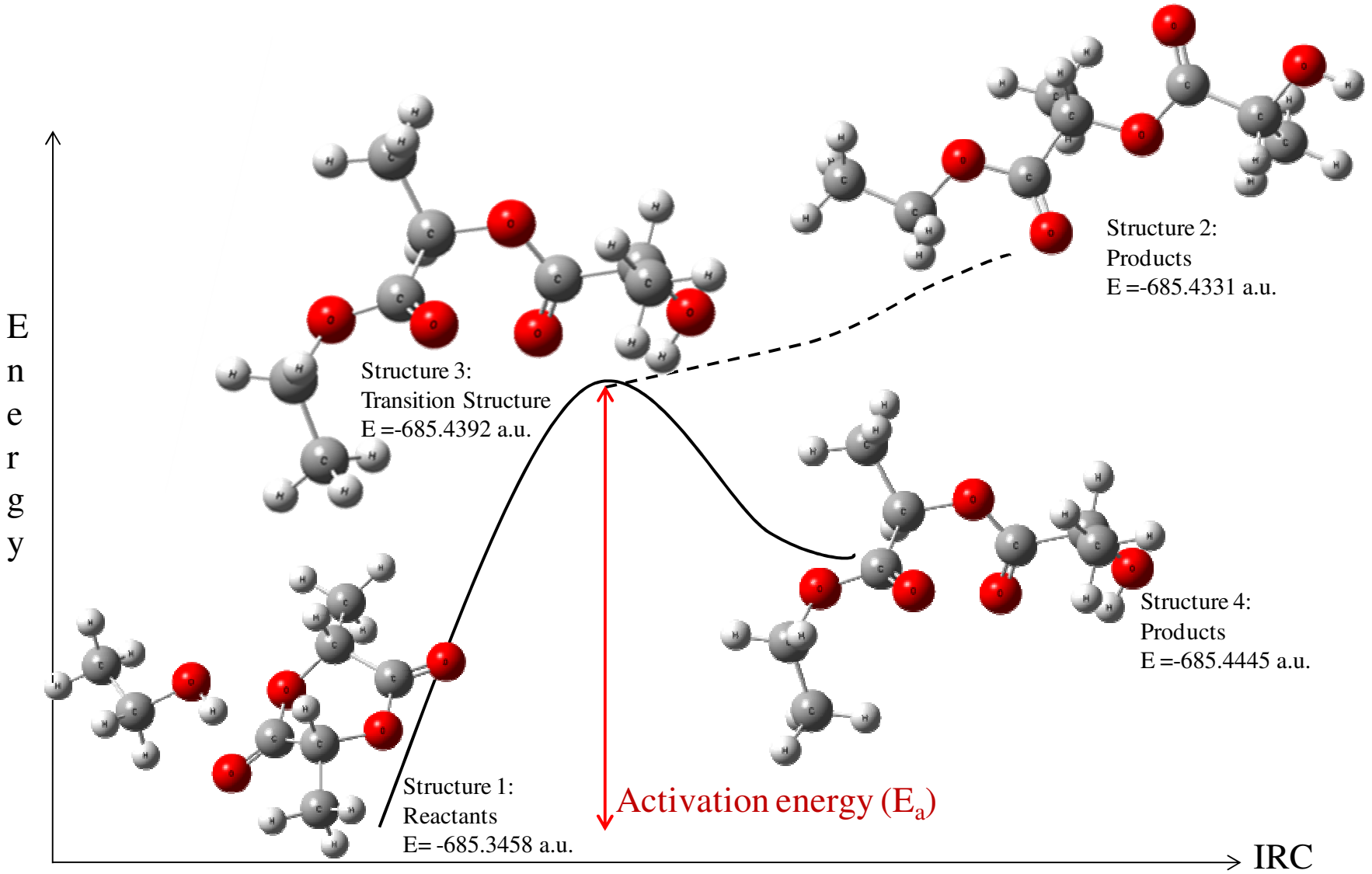

Figure 35. Energy vs. the IRC for the ROP reaction

3.4. Molecular dynamic simulation

The simulation was started by building an amorphous cell of PLA that was optimized and equilibrated using NPT ensemble, as shown in Figure 36, until the calculated density of the system became 1.25 g/cm^3. Approaching this density indicates a closer value from the experimental density for PLA [134] and it was considered as an indicator of how the simulation resembles the real system.

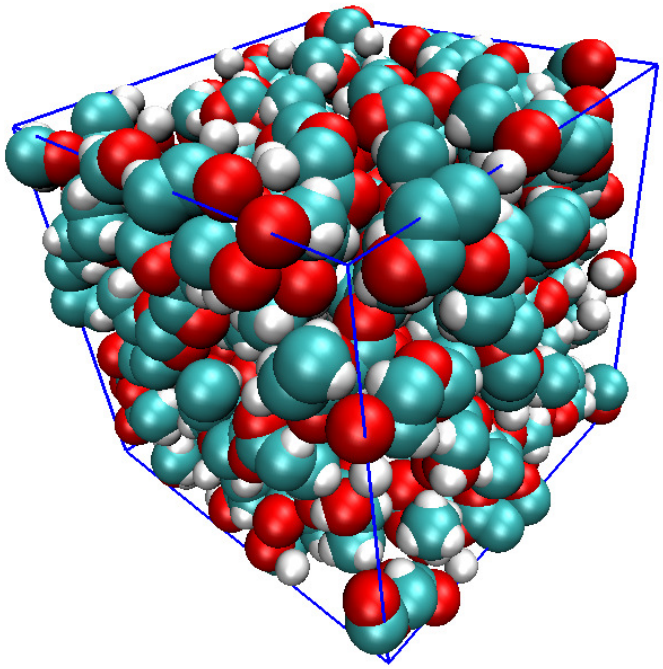

Figure 36. The periodic cell unit of PLA after NPT equilibration

The equilibrated cell was then exposed to a simulated annealing procedure by increasing the temperature of the system from 273 K to 500 K that is about 70 ˚C above the measured melting temperature of PLA, which is *ca.* 150 ˚C. This allows the polymer chains to simulate the melting conditions that provide the system with enough energy to flow and rearrange. The

system was then cooled down to 273 K to allow recrystallization and solidification of the polymer during which the chains go through transition states. The change of the temperature with time extended for about 0.5 microseconds and it is shown in Figure 37 for another short experiment with a run time of 0.5 ns to show the calculation method and to simplify the graph instead of the intense amount of points in the long simulation time.

The simulated annealing procedure was conducted in the NPT ensemble where the Langvin thermostat and barostat control the temperature and the pressure, respectively, and preserve their fluctuation within adjustable limit. The volume of the cell, however, can change in the NPT ensemble according to change in the temperature as shown in Figure 38. The change in the volume indicated in this figure is more random than the change in the temperature because of the use of Langvin thermostat during the simulation.

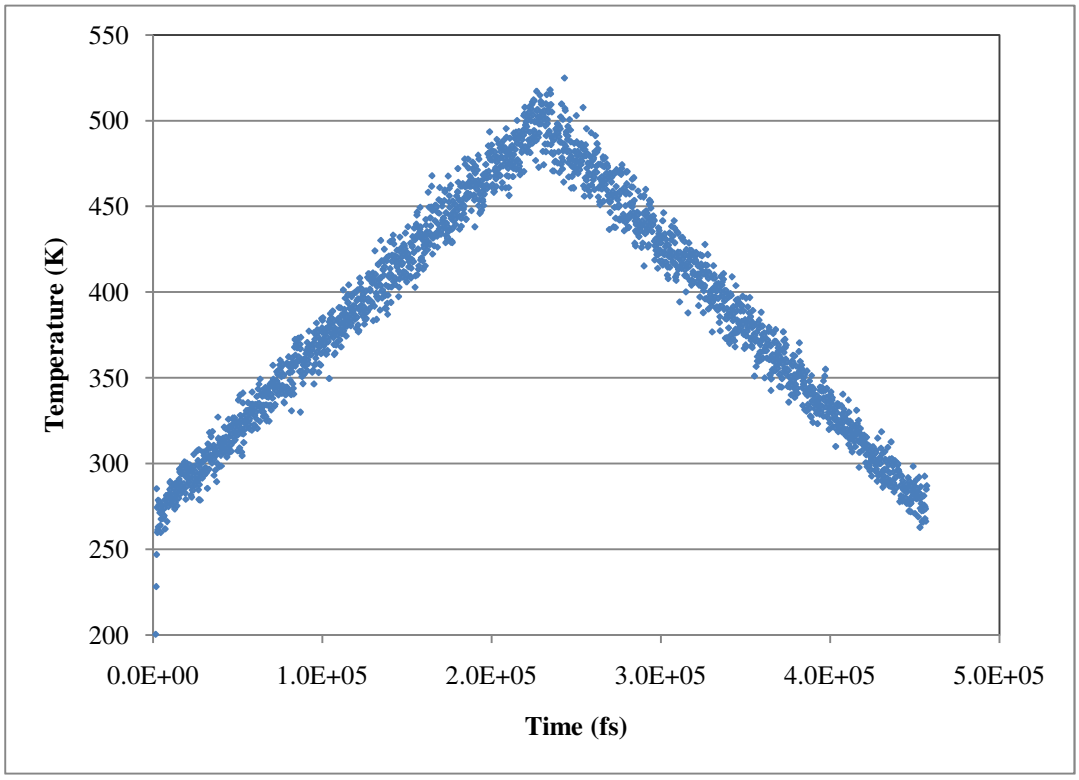

Figure 37. Temperature vs. Time during the simulated annealing procedure

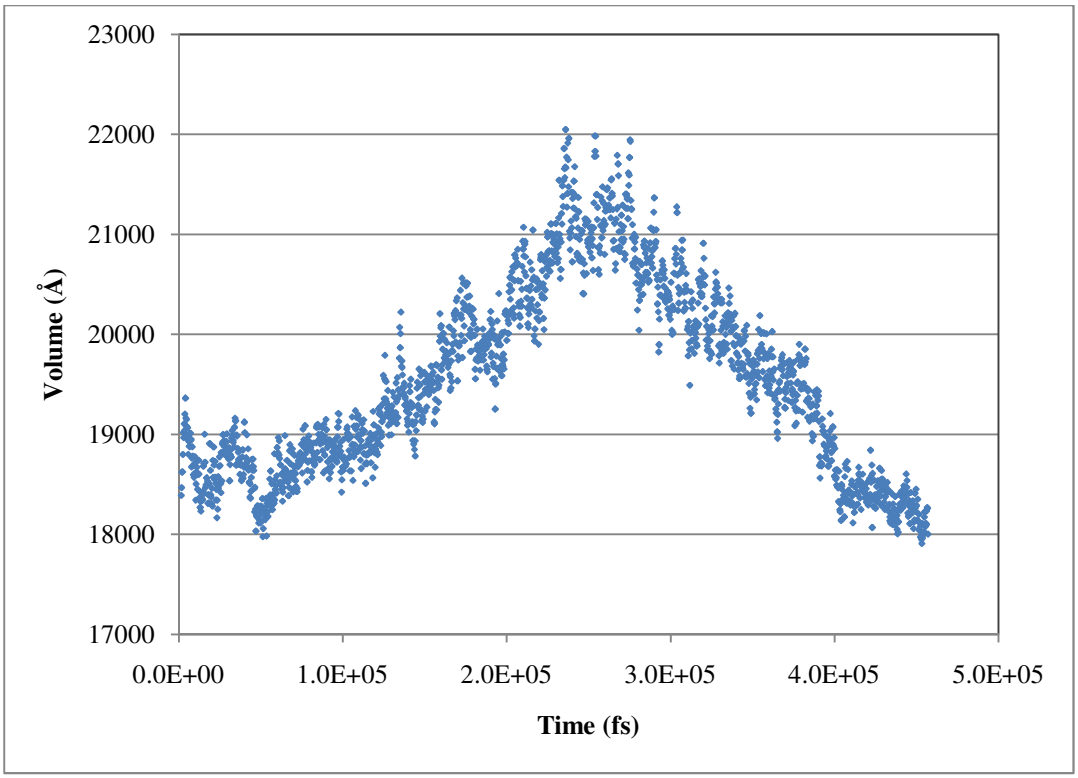

Figure 38. Volume change with time during the simulated annealing

The change in the specific volume of the polymer can then be used to determine the glass transition temperature of the polymer which appears as a kink on the curve of the volume with the temperature as shown in Figure 39 for the short run of 0.5 ns (to explain the calculations then longer simulations will be introduced later). These results were filtered and the volume was averaged at selected temperatures to construct another plot as shown in Figure 40. The relationship between the volume and the temperature has two slopes [135] and the data in the two regions of each slope was separately fitted (as illustrated with two colors) where the extensions of the fitting lines intersect to define the calculated glass transition. A value of *ca.* 340 K was obtained as the T_g of the polymer that is about 17 ˚C above the experimental glass transition for PLA, which is *ca.* 323 K.

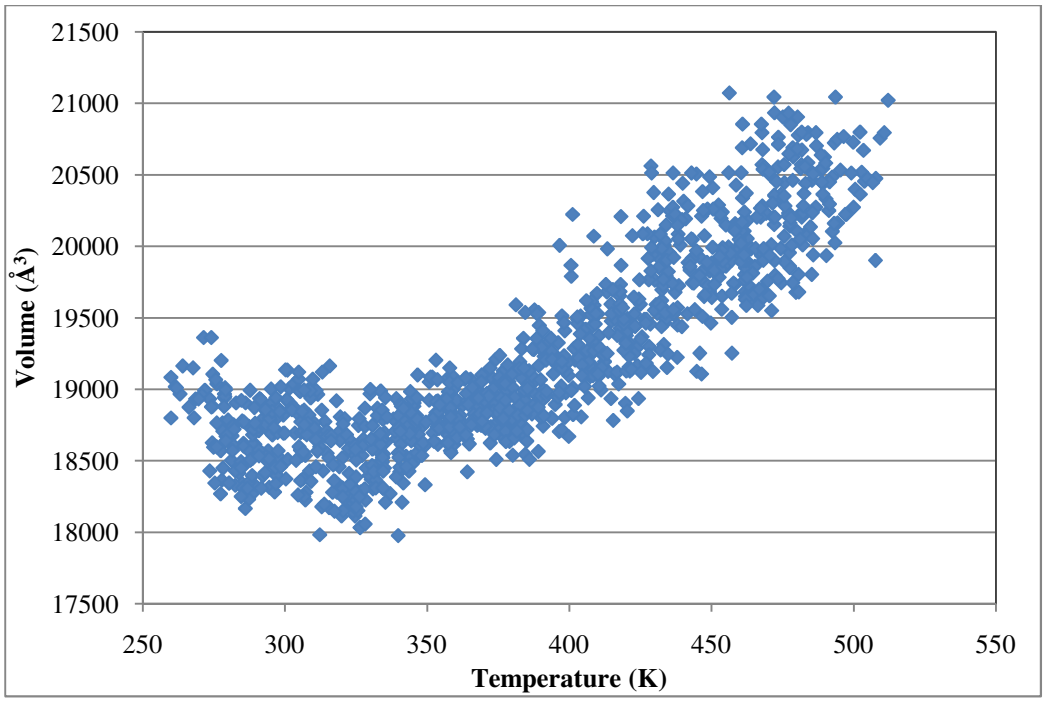

Figure 39. Volume change with temperature during the simulated annealing (0.5 ns simulation time)

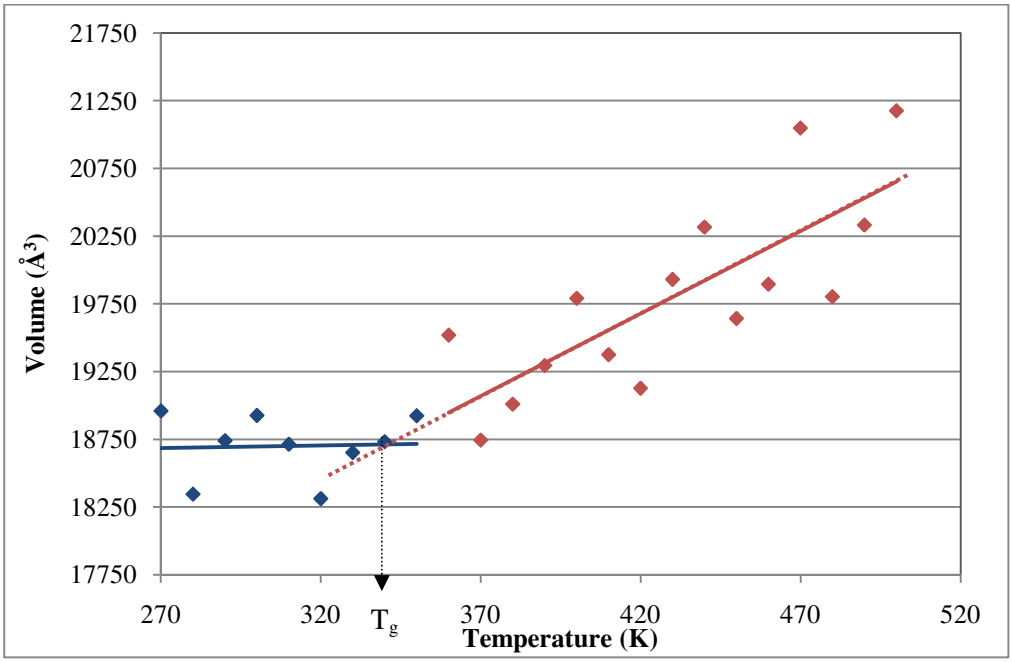

Figure 40. Glass transition temperature as calculated from a simulation with 0.5 ns simulation time

The deviation of the simulation results from the experimental data was reported in previous studies [95, 136] with higher predicted values which can be attributed to the relatively short simulation time (0.5 ns) compared to the chains relaxation times, especially at the relatively low temperatures of simulation [95]. The relaxation time for PLA was reported in the literature to be in the range of milliseconds or less [137] and it was calculated from the rheological results given by Lehermeier and Dorgan [138] to be less than *ca.* 60 ms. Hence, similar experiments were repeated with extended simulation times to verify this explanation for the shift in the calculated glass transition temperature.

By increasing the simulation time to about 46 ns, the calculated glass transition temperature was about 330 K, as indicated in Figure 41, which is closer to the experimental value for this polymer with about 7 ˚C difference. The decrease in the prediction error with the increase in the simulation time is encouraging to obtain better results with longer simulations of about 0.6 microseconds. This simulation time might be the closest that can be reached to the relaxation time due to the relatively expensive computation resources required with longer times. The results of this simulation are shown in Figure 42 where the calculated T_g is *ca.* 326 K which is about 3 ˚C higher than the measured glass transition. The calculated differences in the last two simulations, with relatively longer times, are reasonably acceptable since the measured glass transition was located in the range between 50 to 55 ˚C (323 to 329 K). This implies that molecular dynamic simulation is accurate enough to predict the macroscopic properties of PLA.

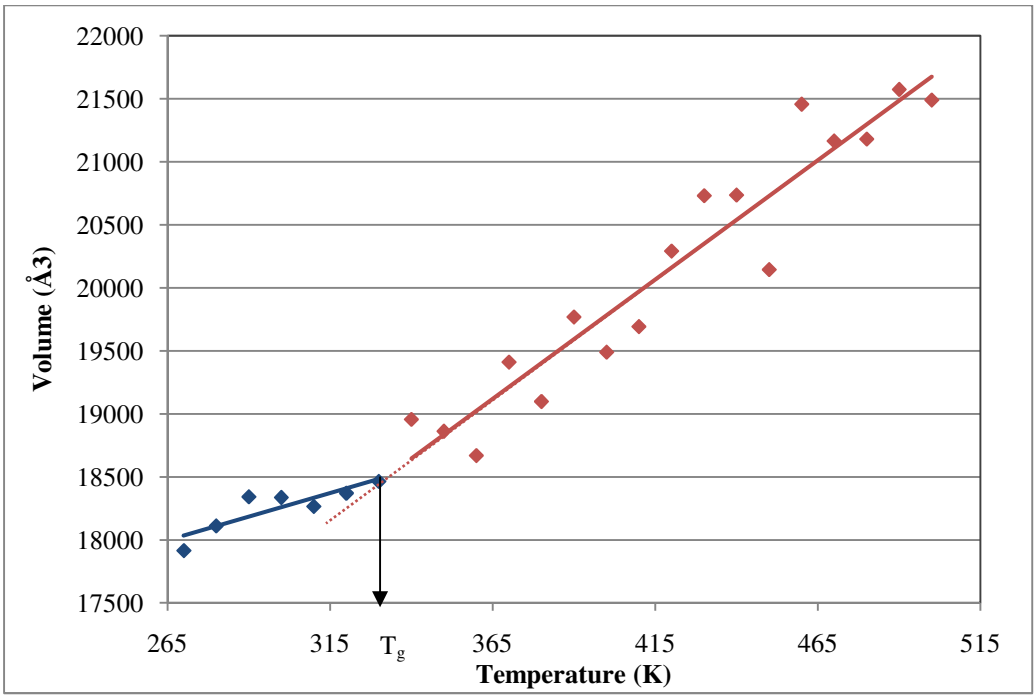

Figure 41. Volume change with temperature to determine the Tg of PLA with about 46 ns simulation time

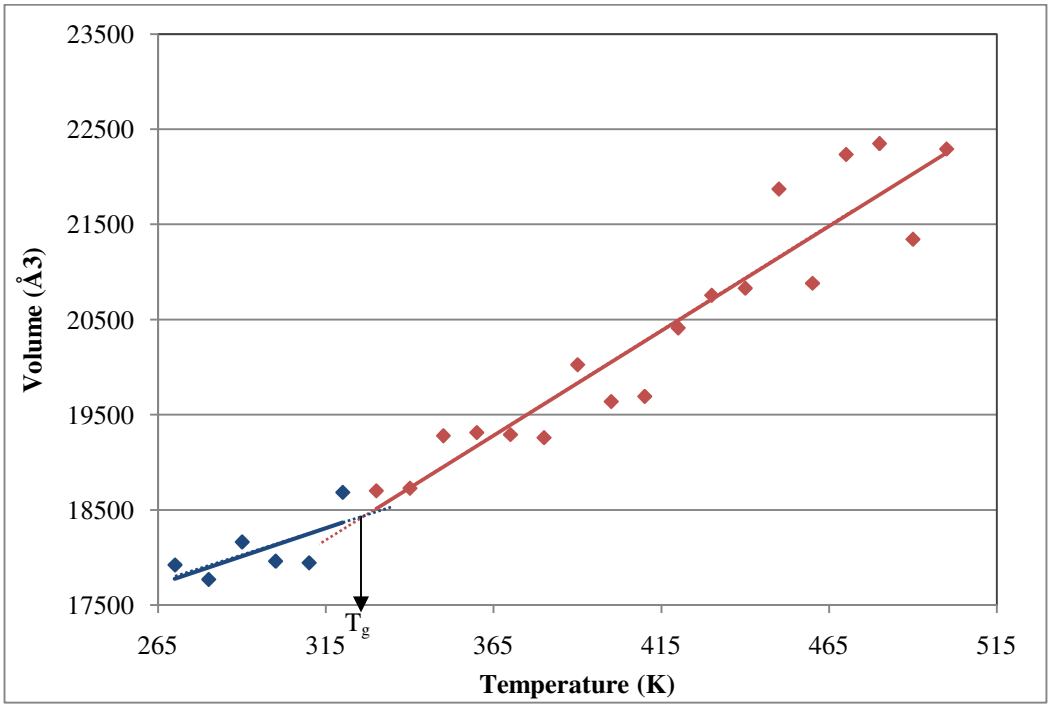

Figure 42. Volume change with temperature to determine the Tg of PLA with about 0.5 microseconds simulation time

4. Conclusion

Modeling of poly(L-lactide) was performed at the electronic as well as the atomistic scales and different properties were predicted from these simulations. Results of the geometrical and structural properties were compared to experimental measurements obtained from the X-ray single crystallography. It was found that the low level calculation using HF/6-31G(d) method was able to successfully simulate the correct geometry of the molecules with accuracy higher than that obtained from DFT methods. HF method, however, was not able to accurately calculate the energy of the molecule compared to DFT methods. It was also observed that DFT methods are insensitive to the accuracy of the geometry of the structure and the results of using low basis set size were as good as using high basis set size. Results also suggest that a B3LYP / 6-311+G(2d,p) method is sufficient to optimize the structure and to calculate its energy and its vibrational frequencies. Increasing the size of the basis set beyond that limit was not significantly effective in increasing the accuracy of the results. The lactide molecule was found to prefer the boat conformation which is more stable than chair conformation due to the high torsion strains and valence angles in the chair conformation. The electronic simulation methods were successful in predicting the IR and NMR spectra of the molecules and the DFT methods were able to resemble experimental spectra even without the application of correction factors. The path of the ROP reaction was studied and the calculated activation energy for the reaction was calculated.

Atomistic simulation using MD was implemented to determine the glass transition of PLA as a one of its macroscopic properties. The predicted T_g was found to be generally higher than the experimental values. The difference between the predicted and the experimental T_g was found to depend on the total simulation time where high difference (about 17 ˚C) was obtained at short simulation times (0.5 ns) and this difference was decreased to about 3 ˚C as the simulation

time was increased to about 0.5 microseconds. The reason for this difference can be attributed to the relatively longer relaxation time of the polymer chains which is located in the milliseconds range that will be relatively computationally expensive with the given resources. The relatively accurate results for the simulation methods introduced in this work indicate that these methods can be trusted to calculate many of the polymer properties using the computer (*in silico*). This will be beneficial in designing new products as it saves a lot of the laborious work associated with the production and testing of their polymeric materials.

References

[1] "Organ Procurement and Transplantation Network (OPTN) data," http://organdonor.gov/.

[2] L. G. Griffith and G. Naughton, "Tissue Engineering--Current Challenges and Expanding Opportunities," *Science,* vol. 295, pp. 1009-1014, 2002.

[3] P. X. Ma and J. H. Elisseeff, *Scaffolding in tissue engineering*. Boca Raton: Taylor&Francis, 2005.

[4] W. H. Dietmar, S. Thorsten, Z. Iwan, N. Kee Woei, T. Swee Hin, and T. Kim Cheng, "Mechanical properties and cell cultural response of polycaprolactone scaffolds designed and fabricated via fused deposition modeling," *Journal of Biomedical Materials Research,* vol. 55, pp. 203-216, 2001.

[5] D. W. Hutmacher, "Scaffolds in tissue engineering bone and cartilage," *Biomaterials,* vol. 21, pp. 2529-2543, 2000.

[6] L. E. Freed, G. Vunjak-Novakovic, R. J. Biron, D. B. Eagles, D. C. Lesnoy, S. K. Barlow, and R. Langer, "Biodegradable Polymer Scaffolds for Tissue Engineering," *Nature Biotechnology,* vol. 12, pp. 689-693, 1994.

[7] F. J. O'Brien, B. A. Harley, I. V. Yannas, and L. Gibson, "Influence of freezing rate on pore structure in freeze-dried collagen-GAG scaffolds," *Biomaterials,* vol. 25, pp. 1077-1086, 2004.

[8] N. J. Benevenga and K. P. Blemings, "Unique Aspects of Lysine Nutrition and Metabolism," *The Journal of Nutrition,* vol. 137, pp. 1610S-1615, 2007.

[9] M. R. Aguilar, A. G. C. Elvira, B. Vázquez, and J. S. Román, "Smart Polymers and Their Applications as Biomaterials," in *Topics in Tissue Engineering*, E-Book ed. vol. 3, N. Ashammakhi, R. Reis, and E. Chiellini, Eds.: EXPERTISSUES, 2007.

[10] R. A. Hule and D. J. Pochan, "Poly(L-lysine) and clay nanocomposite with desired matrix secondary structure: Effects of polypeptide molecular weight," *Journal of Polymer Science: Part B: Polymer Physics,* vol. 45, pp. 239-252, 2007.

[11] T. Sawai, S. Yamazaki, Y. Ishigami, Y. Ikariyama, and M. Aizawa, "Rapid redispersion of pH-sensitive microgel flocculation with poly(lysine)," *Macromolecules,* vol. 24, pp. 5801-5805, 1991.

[12] A. Harada and K. Kataoka, "Formation of Polyion Complex Micelles in an Aqueous Milieu from a Pair of Oppositely-Charged Block Copolymers with Poly (ethylene glycol) Segments," *Macromolecules,* vol. 28, pp. 5294-5299, 1995.

[13] Anne-Claude, Couffin-Hoarau, M. Boustta, and M. Vert, "Enlarging the library of poly-(L-lysine citramide) polyelectrolytic drug carriers," *Journal of Polymer Science: Part A: Polymer Chemistry,* vol. 39, pp. 3475-3484, 2001.

[14] A. Fissi, O. Pieroni, G. Ruggeri, and F. Ciardelli, "Photoresponsive Polymers. Photomodulation of the Macromolecular Structure in Poly(L-lysine) Containing Spiropyran Units," *Macromolecules,* vol. 28, pp. 302-309, 1995.

[15] A. Harada, S. Cammas, and K. Kataoka, "Stabilized alpha-Helix Structure of Poly(L-lysine)-block-poly(ethylene glycol) in Aqueous Medium through Supramolecular Assembly," *Macromolecules,* vol. 29, pp. 6183-6188, 1996.

[16] S. C. De Smedt, J. Demeester, and W. E. Hennink, "Cationic Polymer Based Gene Delivery Systems," *Pharmaceutical Research,* vol. 17, pp. 113-126, 2000.

[17] P. M. Quinton and C. W. Philpott, "A Role for Anionic Sites in Epithelial Architecture: Effects of Cationic Polymers on Cell Membrane Structure," *The Journal of Cell Biology,* vol. 56, pp. 787-796, 1973.

[18] S. Senel, G. Bayramoglu, and M. Y. Arica, "DNA adsorption on a poly-L-lysine-immobilized poly(2-hydroxyethyl methacrylate) membrane," *Polymer International,* vol. 52, pp. 1169-1174, 2003.

[19] J. A. Hubbell, "Bioactive biomaterials," *Current Opinion in Biotechnology,* vol. 10, pp. 123-129, 1999.

[20] C. Picart, P. Lavalle, P. Hubert, F. J. G. Cuisinier, G. Decher, P. Schaaf, and J. C. Voegel, "Buildup Mechanism for Poly(l-lysine)/Hyaluronic Acid Films onto a Solid Surface," *Langmuir,* vol. 17, pp. 7414-7424, 2001.

[21] G. B. Schneider, A. English, M. Abraham, R. Zaharias, C. Stanford, and J. Keller, "The effect of hydrogel charge density on cell attachment," *Biomaterials,* vol. 25, pp. 3023-3028, 2004.

[22] K. Akiyoshi, A. Ueminami, S. Kurumada, and Y. Nomura, "Self-Association of Cholesteryl-Bearing Poly(L-lysine) in Water and Control of Its Secondary Structure by Host-Guest Interaction with Cyclodextrin," *Macromolecules,* vol. 33, pp. 6752-6756, 2000.

[23] S. General and A. F. Thünemann, "pH-sensitive nanoparticles of poly(amino acid) dodecanoate complexes," *International Journal of Pharmaceutics,* vol. 230, pp. 11-24, 2001.

[24] S. Lecommandoux, M. F. Achard, J. F. Langenwalter, and H.-A. Klok, "Self-assembly of rod-coil diblock oligomers based on alpha- helical peptides," *Macromolecules,* vol. 34, pp. 9100-9111, 2001.

[25] N. Xu, F. S. Du, and Z. C. Li, "Synthesis of poly(L-lysine) graft polyesters through Michael addition and their self-assemblies in aqueous solutions," *Journal of Polymer Science: Part A: Polymer Chemistry,* vol. 45, pp. 1889-1898, 2007.

[26] M. X. Tang and F. C. Szoka, "The influence of polymer structure on the interactions of cationic polymers with DNA and morphology of the resulting complexes," *Gene Therapy,* vol. 4, p. 823, 1997.

[27] D. S. Terman, I. Stewart, J. Robinette, R. Carr, and R. Harbeck, "Specific removal of DNA antibodies in vivo with an extracorporeal immuno-adsorbent," *Clinical and Experimental Immunology,* vol. 24, p. 231, 1976.

[28] G. Orive, S. K. Tam, J. L. Pedraz, and J.-P. Hallé, "Biocompatibility of alginate-poly-l-lysine microcapsules for cell therapy," *Biomaterials,* vol. 27, pp. 3691-3700, 2006.

[29] B. L. Strand, L. Ryan, P. I. Veld, B. Kulseng, A. M. Rokstad, G. Skjak-Braek, and T. Espevik, "Poly-L-lysine induces fibrosis on alginate microcapsules via the induction of cytokines," *Cell Transplantation,* vol. 10, pp. 263-275, 2001.

[30] J. Varani, D. R. Inman, S. E. G. Fligiel, and W. J. Hillegas, "Use of recombinant and synthetic peptides as attachment factors for cells on microcarriers," *Cytotechnology,* vol. 13, pp. 89-98, 1993.

[31] D. C. Alonzo, S. H. Jeffrey, N. G. Nicholas, M. J. Ivette, B. P. Utpal, M. C. Scott, and L. Robert, "Characterization and development of RGD-peptide-modified poly(lactic acid-co-lysine) as an interactive, resorbable biomaterial," *Journal of Biomedical Materials Research,* vol. 35, pp. 513-523, 1997.

[32] U. Hersel, C. Dahmen, and H. Kessler, "RGD modified polymers: biomaterials for stimulated cell adhesion and beyond," *Biomaterials,* vol. 24, pp. 4385-4415, 2003.

[33] R. A. Quirk, W. C. Chan, M. C. Davies, S. J. B. Tendler, and K. M. Shakesheff, "Poly(-lysine)-GRGDS as a biomimetic surface modifier for poly(lactic acid)," *Biomaterials,* vol. 22, pp. 865-872, 2001.

[34] K. E. Crompton, J. D. Goud, R. V. Bellamkonda, T. R. Gengenbach, D. I. Finkelstein, M. K. Horne, and J. S. Forsythe, "Polylysine-functionalised thermoresponsive chitosan hydrogel for neural tissue engineering," *Biomaterials,* vol. 28, pp. 441-449, 2007.

[35] C. Mingyu, G. Kai, L. Jiamou, G. Yandao, Z. Nanming, and Z. Xiufang, "Surface Modification and Characterization of Chitosan Film Blended with Poly-L-Lysine," *Journal of Biomaterials Applications,* vol. 19, pp. 59-75, 2004.

[36] K. Vahik, K. Mary, C. Mary, N. Andrew, D. Timothy, and P. Darrin, "Polypeptide-based nanocomposite Structure and properties of poly(L-lysine)Na+-montmorillonite," *Journal of polymer science. Part B. Polymer physics,* vol. 40, pp. 2579-2586, 2002.

[37] Y. Zhang, J. Li, Y. Shen, M. Wang, and J. Li, "Poly-L-lysine Functionalization of Single-Walled Carbon Nanotubes," *The Journal of Physical Chemistry B,* vol. 108, pp. 15343-15346, 2004.

[38] J. Li, W.-D. He, L.-P. Yang, X.-L. Sun, and Q. Hua, "Preparation of multi-walled carbon nanotubes grafted with synthetic poly(l-lysine) through surface-initiated ring-opening polymerization," *Polymer,* vol. 48, pp. 4352-4360, 2007.

[39] Y. Ding, J. Liu, X. Jin, H. Lu, G. Shen, and R. Yu, "Poly-l-lysine/hydroxyapatite/carbon nanotube hybrid nanocomposite applied for piezoelectric immunoassay of carbohydrate antigen 19-9," *The Analyst,* vol. 133, pp. 184-190, 2008.

[40] X. Li and R. Pelton, "Enhancing Wet Cellulose Adhesion with Proteins," *Industrial & Engineering Chemistry Research,* vol. 44, pp. 7398-7404, 2005.

[41] S. Ichiro, N. Yasuhiko, and I. Taisuke, "Experimental determination of the elastic modulus of crystalline regions in oriented polymers," *Journal of Polymer Science,* vol. 57, pp. 651-660, 1962.

[42] D. J. Mooney, D. F. Baldwin, N. P. Suh, J. P. Vacanti, and R. Langer, "Novel approach to fabricate porous sponges of poly(-lactic-co-glycolic acid) without the use of organic solvents," *Biomaterials,* vol. 17, pp. 1417-1422, 1996.

[43] S. J. Hollister, "Porous scaffold design for tissue engineering," *Nature Materials,* vol. 4, pp. 518-524, 2005.

[44] N. E. Marcovich, M. L. Auad, N. E. Bellesi, S. R. Nutt, and M. I. Aranguren, "Cellulose micro/nanocrystals reinforced polyurethane," *Journal Of Materials Research,* vol. 21, pp. 870-881, 2006.

[45] X. M. Dong, J.-F. Revol, and D. G. Gray, "Effect of microcrystallite preparation conditions on the formation of colloid crystals of cellulose," *Cellulose,* vol. 5, pp. 19-32, 1998.

[46] J. Guan, K. L. Fujimoto, M. S. Sacks, and W. R. Wagner, "Preparation and characterization of highly porous, biodegradable polyurethane scaffolds for soft tissue applications," *Biomaterials,* vol. 26, pp. 3961-3971, 2005.

[47] "ASTM Standard Practice for Conditioning and Testing Textiles," *ASTM International,* vol. 7.01 D 1776 – 04, 2004.

[48] J. W. Severinghaus, M. Stupfel, and A. F. Bradley, "Accuracy of Blood ph and Pco2 Determinations," *J Appl Physiol,* vol. 9, pp. 189-196, 1956.

[49] H. Susi, S. N. Timasheff, and L. Stevens, "Infrared Spectra and Protein Conformations in Aqueous Solutions: I.The Amide I Band in H2O and D2O Solutions," *Journal of Biological Chemistry,* vol. 242, pp. 5460-5466, 1967.

[50] D. Wojciech, M. Takeshi, K. Minoru, and T. Yoshihiro, "Chain-length dependence of alpha-helix to beta-sheet transition in polylysine: Model of protein aggregation studied by temperature-tuned FTIR spectroscopy," *Biopolymers,* vol. 73, pp. 463-469, 2004.

[51] G. D. Rose and R. Wolfenden, "Hydrogen Bonding, Hydrophobicity, Packing, and Protein Folding," *Annual Review of Biophysics and Biomolecular Structure,* vol. 22, pp. 381-415, 1993.

[52] A. P. Mathew, K. Oksman, and M. Sain, "Mechanical properties of biodegradable composites from poly lactic acid (PLA) and microcrystalline cellulose (MCC)," *Journal of Applied Polymer Science,* vol. 97, pp. 2014-2025, 2005.

[53] O. Mishima and H. E. Stanley, "The relationship between liquid, supercooled and glassy water," *Nature,* vol. 396, pp. 329-335, 1998.

[54] A. C. Albertsson and I. K. Varma, "Recent Developments in Ring Opening Polymerization of Lactones for Biomedical Applications," *Biomacromolecules,* vol. 4, pp. 1466-1486, 2003.

[55] J. W. Leenslag, A. J. Pennings, R. R. M. Bos, F. R. Rozema, and G. Boering, "Resorbable materials of poly(l-lactide). VI. Plates and screws for internal fracture fixation," *Biomaterials,* vol. 8, pp. 70-73, 1987.

[56] R. S. Bezwada, D. D. Jamiolkowski, I.-Y. Lee, V. Agarwal, J. Persivale, S. Trenka-Benthin, M. Erneta, J. Suryadevara, A. Yang, and S. Liu, "Monocryl® suture, a new ultra-pliable absorbable monofilament suture," *Biomaterials,* vol. 16, pp. 1141-1148, 1995.

[57] G. Sylwester and J. P. Albert, "An artificial skin based on biodegradable mixtures of polylactides and polyurethanes for full-thickness skin wound covering," *Die Makromolekulare Chemie, Rapid Communications,* vol. 4, pp. 675-680, 1983.

[58] H. Tamai, K. Igaki, E. Kyo, K. Kosuga, A. Kawashima, S. Matsui, H. Komori, T. Tsuji, S. Motohara, and H. Uehata, "Initial and 6-Month Results of Biodegradable Poly-l-Lactic Acid Coronary Stents in Humans," *Circulation,* vol. 102, pp. 399-404, 2000.

[59] B. Buntner, M. Nowak, J. Kasperczyk, M. Ryba, P. Grieb, M. Walski, P. Dobrzyñski, and M. Bero, "The application of microspheres from the copolymers of lactide and [epsilon]-caprolactone to the controlled release of steroids," *Journal of Controlled Release,* vol. 56, pp. 159-167, 1998.

[60] L. I. Susan, M. C. Genevieve, J. M. Michael, W. Y. Alan, J. Y. Michael, and G. M. Antonios, "Bone formation by three-dimensional stromal osteoblast culture in biodegradable polymer scaffolds," *Journal of Biomedical Materials Research,* vol. 36, pp. 17-28, 1997.

[61] S. L. Ishaug-Riley, G. M. Crane-Kruger, M. J. Yaszemski, and A. G. Mikos, "Three-dimensional culture of rat calvarial osteoblasts in porous biodegradable polymers," *Biomaterials,* vol. 19, pp. 1405-1412, 1998.

[62] C. M. Agrawal, J. Best, J. D. Heckman, and B. D. Boyan, "Protein release kinetics of a biodegradable implant for fracture non-unions," *Biomaterials,* vol. 16, pp. 1255-1260, 1995.

[63] L. E. Freed, J. C. Marquis, A. Nohria, J. Emmanual, A. G. Mikos, and R. Langer, "Neocartilage formation in vitro and in vivo using cells cultured on synthetic biodegradable polymers," *Journal of Biomedical Materials Research,* vol. 27, pp. 11-23, 1993.

[64] R. Mehta, V. Kumar, H. Bhunia, and S. N. Upadhyay, "Synthesis of Poly(Lactic Acid): A Review," *Journal of Macromolecular Science: Polymer Reviews,* vol. 45, pp. 325-349, 2005.

[65] C. Jérôme and P. Lecomte, "Recent advances in the synthesis of aliphatic polyesters by ring-opening polymerization," *Advanced Drug Delivery Reviews,* vol. 60, pp. 1056-1076, 2008.

[66] G. G. Odian, *Principles of polymerization*, 4th ed. Hoboken, N.J.: John Wiley & Sons, Inc., 2004.

[67] F. Nederberg, E. F. Connor, M. Möller, T. Glauser, and J. L. Hedrick, "New Paradigms for Organic Catalysts: The First Organocatalytic Living Polymerization," *Angewandte Chemie International Edition,* vol. 40, pp. 2712-2715, 2001.

[68] O. Dechy-Cabaret, B. Martin-Vaca, and D. Bourissou, "Controlled Ring-Opening Polymerization of Lactide and Glycolide," *Chemical Reviews,* vol. 104, pp. 6147-6176, 2004.

[69] H. Tsuji, "Poly(lactide) Stereocomplexes: Formation, Structure, Properties, Degradation, and Applications," *Macromolecular Bioscience,* vol. 5, pp. 569-597, 2005.

[70] J. Kadota, D. PavlovicÌ , J.-P. Desvergne, B. Bibal, F. d. r. Peruch, and A. Deffieux, "Ring-Opening Polymerization of l-Lactide Catalyzed by an Organocatalytic System Combining Acidic and Basic Sites," *Macromolecules,* p. XXX, 2010.

[71] E. F. Connor, G. W. Nyce, M. Myers, A. Möck, and J. L. Hedrick, "First Example of N-Heterocyclic Carbenes as Catalysts for Living Polymerization: Organocatalytic Ring-Opening Polymerization of Cyclic Esters," *Journal of the American Chemical Society,* vol. 124, pp. 914-915, 2002.

[72] M. G. McKee, S. Unal, G. L. Wilkes, and T. E. Long, "Branched polyesters: recent advances in synthesis and performance," *Progress in Polymer Science,* vol. 30, pp. 507-539, 2005.

[73] I. Kazuhiko, Y. Midori, and I. Masatoshi, "Recyclable shape-memory polymer: Poly(lactic acid) crosslinked by a thermoreversible Diels-Alder reaction," *Journal of Applied Polymer Science,* vol. 112, pp. 876-885, 2009.

[74] R. M. Rasal, A. V. Janorkar, and D. E. Hirt, "Poly(lactic acid) modifications," *Progress in Polymer Science,* vol. 35, pp. 338-356, 2010.

[75] T. Biela, A. Duda, K. Rode, and H. Pasch, "Characterization of star-shaped poly(l-lactide)s by liquid chromatography at critical conditions," *Polymer,* vol. 44, pp. 1851-1860, 2003.

[76] F. Rodriguez, F. Rodriguez, and NetLibrary Inc., *Principles of polymer systems*, 5th ed. New York: Taylor & Francis, 2003.

[77] T. J. Tulig and M. Tirrell, "Molecular theory of the Trommsdorff effect," *Macromolecules,* vol. 14, pp. 1501-1511, 1981.

[78] R. Knischka, P. J. Lutz, A. Sunder, R. Mulhaupt, and H. Frey, "Functional Poly(ethylene oxide) Multiarm Star Polymers: Core-First Synthesis Using Hyperbranched Polyglycerol Initiators," *Macromolecules,* vol. 33, pp. 315-320, 1999.

[79] J. Li, J. Ren, Y. Cao, and W. Yuan, "Synthesis of biodegradable pentaarmed star-block copolymers via an asymmetric BIS-TRIS core by combination of ROP and RAFT: From star architectures to double responsive micelles," *Polymer,* vol. 51, pp. 1301-1310, 2010.

[80] J. Roovers, L. L. Zhou, P. M. Toporowski, M. van der Zwan, H. Iatrou, and N. Hadjichristidis, "Regular star polymers with 64 and 128 arms. Models for polymeric micelles," *Macromolecules,* vol. 26, pp. 4324-4331, 1993.

[81] J. L. Wang, L. Wang, and C. M. Dong, "Synthesis, crystallization, and morphology of star-shaped poly(ε-caprolactone)," *Journal of Polymer Science Part A: Polymer Chemistry,* vol. 43, pp. 5449-5457, 2005.

[82] A. O. Helminen, H. Korhonen, and J. V. Seppälä, "Structure modification and crosslinking of methacrylated polylactide oligomers," *Journal of Applied Polymer Science,* vol. 86, pp. 3616-3624, 2002.

[83] K. Numata, R. K. Srivastava, A. Finne-Wistrand, A.-C. Albertsson, Y. Doi, and H. Abe, "Branched Poly(lactide) Synthesized by Enzymatic Polymerization: Effects of Molecular Branches and Stereochemistry on Enzymatic Degradation and Alkaline Hydrolysis," *Biomacromolecules,* vol. 8, pp. 3115-3125, 2007.

[84] J. Clayden, *Organic chemistry*. Oxford ; New York: Oxford University Press, 2001.

[85] J. E. Mark, *Physical properties of polymers handbook*. Woodbury, N.Y.: AIP Press, 1996.

[86] F. Tasaka, H. Miyazaki, Y. Ohya, and T. Ouchi, "Synthesis of Comb-Type Biodegradable Polylactide through Depsipeptide -Lactide Copolymer Containing Serine Residues," *Macromolecules,* vol. 32, pp. 6386-6389, 1999.

[87] M. Baiardo, G. Frisoni, M. Scandola, M. Rimelen, D. Lips, K. Ruffieux, and E. Wintermantel, "Thermal and mechanical properties of plasticized poly(L-lactic acid)," *Journal of Applied Polymer Science,* vol. 90, pp. 1731-1738, 2003.

[88] S. Solarski, M. Ferreira, and E. Devaux, "Characterization of the thermal properties of PLA fibers by modulated differential scanning calorimetry," *Polymer,* vol. 46, pp. 11187-11192, 2005.

[89] C. Nakafuku and M. Sakoda, "Melting and Crystallization of Poly(L-lactic acid) and Poly(ethylene oxide) Binary Mixture," *Polymer Journal,* vol. 25, pp. 909-917, 1993.

[90] M. Yasuniwa, S. Tsubakihara, Y. Sugimoto, and C. Nakafuku, "Thermal analysis of the double-melting behavior of poly(L-lactic acid)," *Journal of Polymer Science Part B: Polymer Physics,* vol. 42, pp. 25-32, 2004.

[91] M. Yasuniwa, S. Tsubakihara, and T. Fujioka, "X-ray and DSC studies on the melt-recrystallization process of poly(butylene naphthalate)," *Thermochimica Acta,* vol. 396, pp. 75-78, 2003.

[92] L. H. Sperling, *Interpenetrating polymer networks and related materials*. New York: Plenum Press, 1981.

[93] M. J. Elwell, A. J. Ryan, H. J. M. Grunbauer, and H. C. Van Lieshout, "In-Situ Studies of Structure Development during the Reactive Processing of Model Flexible Polyurethane Foam Systems Using FT-IR Spectroscopy, Synchrotron SAXS, and Rheology," *Macromolecules,* vol. 29, pp. 2960-2968, 1996.

[94] L. Xu, C. Li, and K. Y. S. Ng, "In-Situ Monitoring of Urethane Formation by FTIR and Raman Spectroscopy," *The Journal of Physical Chemistry A,* vol. 104, pp. 3952-3957, 2000.

[95] J. Han, R. H. Gee, and R. H. Boyd, "Glass Transition Temperatures of Polymers from Molecular Dynamics Simulations," *Macromolecules,* vol. 27, pp. 7781-7784, 1994.

[96] A. A. Askadskiæi, *Computational materials science of polymers*. Cambridge, UK: Cambridge International Science Pub., 2003.

[97] S. Yip, *Handbook of materials modeling*. Dordrecht ; New York: Springer, 2005.

[98] M. Laso and E. A. Perpáete, *Multiscale modelling of polymer properties*. Amsterdam ; Boston: Elsevier, 2006.

[99] W. K. Liu, E. G. Karpov, and H. S. Park, *Nano mechanics and materials : theory, multiscale methods and applications*. Chichester, England ; Hoboken, NJ: John Wiley, 2006.

[100] Q. H. Zeng, A. B. Yu, and G. Q. Lu, "Multiscale modeling and simulation of polymer nanocomposites," *Progress in Polymer Science,* vol. 33, pp. 191-269, 2008.

[101] R. Raffaele, "Ab initio simulation of the properties of ferroelectric materials," *Modelling and Simulation in Materials Science and Engineering,* vol. 11, p. R69, 2003.

[102] R. M. Martin, *Electronic structure : basic theory and practical methods*. Cambridge ; New York: Cambridge University Press, 2004.

[103] A. E. Mattsson, P. A. Schultz, M. P. Desjarlais, T. R. Mattsson, and K. Leung, "Designing meaningful density functional theory calculations in materials science- a primer," *Modelling and Simulation in Materials Science and Engineering,* vol. 13, p. R1, 2005.

[104] V. A. Harmandaris, V. G. Mavrantzas, and D. N. Theodorou, "Atomistic Molecular Dynamics Simulation of Stress Relaxation upon Cessation of Steady-State Uniaxial Elongational Flow," *Macromolecules,* vol. 33, pp. 8062-8076, 2000.

[105] W. A. Curtin and R. E. Miller, "Atomistic/continuum coupling in computational materials science," *Modelling and Simulation in Materials Science and Engineering,* vol. 11, p. R33, 2003.

[106] J. Yanagimoto, "FE-based analysis for the prediction of inner microstructure in metal forming," *Modelling and Simulation in Materials Science and Engineering,* vol. 10, p. R111, 2002.

[107] M. L. Coote, "Quantum-Chemical Modeling of Free-Radical Polymerization," *Macromolecular Theory and Simulations,* vol. 18, pp. 388-400, 2009.

[108] S. Stolbov, M. A. Ortigoza, and T. S. Rahman, "Application of density functional theory to CO tolerance in fuel cells: a brief review," *Journal of Physics: Condensed Matter,* vol. 21, p. 474226, 2009.

[109] Y. W. Li, J. H. Yao, X. D. Zhu, C. J. Liu, J. Q. Jiang, and X. S. Deng, "Theoretical investigations on the geometric and electronic structures of polyacetylene molecule under the influence of external electric field," *eXPRESS Polymer Letters,* vol. 3, pp. 684–691, 2009.

[110] B. Derecskei and A. Derecskei-Kovacs, "Molecular modelling simulations to predict density and solubility parameters of ionic liquids," *Molecular Simulation,* vol. 34, pp. 1167 - 1175, 2008.

[111] V. G. Mavrantzas and D. N. Theodorou, "Atomistic Simulation of Polymer Melt Elasticity: Calculation of the Free Energy of an Oriented Polymer Melt," *Macromolecules,* vol. 31, pp. 6310-6332, 1998.

[112] N. C. Karayiannis, V. G. Mavrantzas, and D. N. Theodorou, "Detailed Atomistic Simulation of the Segmental Dynamics and Barrier Properties of Amorphous Poly(ethylene terephthalate) and Poly(ethylene isophthalate)," *Macromolecules,* vol. 37, pp. 2978-2995, 2004.

[113] N. W. Suek and M. H. Lamm, "Effect of Terminal Group Modification on the Solution Properties of Dendrimers: A Molecular Dynamics Simulation Study," *Macromolecules,* vol. 39, pp. 4247-4255, 2006.

[114] G. D. Smith, W. Paul, M. Monkenbusch, L. Willner, D. Richter, X. H. Qiu, and M. D. Ediger, "Molecular Dynamics of a 1,4-Polybutadiene Melt. Comparison of Experiment and Simulation," *Macromolecules,* vol. 32, pp. 8857-8865, 1999.

[115] J. Rottler, "Molecular dynamics simulations of glassy polymers: a molecular modeling perspective," *J. Phys.: Condens. Matter* vol. 21, p. 463101, 2009.

[116] I. N. Levine, *Quantum chemistry*, 5th ed. Upper Saddle River, N.J.: Prentice Hall, 2000.

[117] M. J. Frisch, G. W. Trucks, H. B. Schlegel, G. E. Scuseria, M. A. Robb, J. R. Cheeseman, G. Scalmani, V. Barone, B. Mennucci, G. A. Petersson, H. Nakatsuji, M. Caricato, X. Li, H. P. Hratchian, A. F. Izmaylov, J. Bloino, G. Zheng, J. L. Sonnenberg, M. Hada, M. Ehara, K. Toyota, R. Fukuda, J. Hasegawa, M. Ishida, T. Nakajima, Y. Honda, O. Kitao, H. Nakai, T. Vreven, J. J. A. Montgomery, J. E. Peralta, F. Ogliaro, M. Bearpark, J. J.

Heyd, E. Brothers, K. N. Kudin, V. N. Staroverov, R. Kobayashi, J. Normand, K. Raghavachari, A. Rendell, J. C. Burant, S. S. Iyengar, J. Tomasi, M. Cossi, N. Rega, J. M. Millam, M. Klene, J. E. Knox, J. B. Cross, V. Bakken, C. Adamo, J. Jaramillo, R. Gomperts, R. E. Stratmann, O. Yazyev, A. J. Austin, R. Cammi, C. Pomelli, J. W. Ochterski, R. L. Martin, K. Morokuma, V. G. Zakrzewski, G. A. Voth, P. Salvador, J. J. Dannenberg, S. Dapprich, A. D. Daniels, O. Farkas, J. B. Foresman, J. V. Ortiz, J. Cioslowski, and D. J. Fox, *Gaussian 09, Revision A.02*. Wallingford CT: Gaussian, Inc., 2009.

[118] J. B. Foresman, A. Frisch, and Gaussian Inc., *Exploring chemistry with electronic structure methods*, 2nd ed. Pittsburgh, PA: Gaussian, Inc., 1996.

[119] A. R. Leach, *Molecular modelling : principles and applications*, 2nd ed. Harlow, England ; New York: Prentice Hall, 2001.

[120] E. Lewars, *Computational chemistry : introduction to the theory and applications of molecular and quantum mechanics*. Boston: Kluwer Academic, 2003.

[121] W. Koch and M. C. Holthausen, *A chemist's guide to density functional theory*, 2nd ed. Weinheim ; New York: Wiley-VCH, 2001.

[122] W. Kohn and L. J. Sham, "Self-Consistent Equations Including Exchange and Correlation Effects," *Physical Review,* vol. 140, p. A1133, 1965.

[123] P. J. Stephens, F. J. Devlin, C. F. Chabalowski, and M. J. Frisch, "Ab Initio Calculation of Vibrational Absorption and Circular Dichroism Spectra Using Density Functional Force Fields," *The Journal of Physical Chemistry,* vol. 98, pp. 11623-11627, 1994.

[124] M. C. Nicklaus, "Conformational energies calculated by the molecular mechanics program CHARMm," *Journal of Computational Chemistry,* vol. 18, pp. 1056-1060, 1997.

[125] N. Foloppe and J. A. D. MacKerell, "All-atom empirical force field for nucleic acids: I. Parameter optimization based on small molecule and condensed phase macromolecular target data," *Journal of Computational Chemistry,* vol. 21, pp. 86-104, 2000.

[126] G. J. Martyna, D. J. Tobias, and M. L. Klein, "Constant pressure molecular dynamics algorithms," *The Journal of Chemical Physics,* vol. 101, pp. 4177-4189, 1994.

[127] S. E. Feller, Y. Zhang, R. W. Pastor, and B. R. Brooks, "Constant pressure molecular dynamics simulation: The Langevin piston method," *The Journal of Chemical Physics,* vol. 103, pp. 4613-4621, 1995.

[128] J. A. Izaguirre, D. P. Catarello, J. M. Wozniak, and R. D. Skeel, "Langevin stabilization of molecular dynamics," *The Journal of Chemical Physics,* vol. 114, pp. 2090-2098, 2001.

[129] J. C. Phillips, R. Braun, W. Wang, J. Gumbart, E. Tajkhorshid, E. Villa, C. Chipot, R. D. Skeel, L. Kalé, and K. Schulten, "Scalable molecular dynamics with NAMD," *Journal of Computational Chemistry,* vol. 26, pp. 1781-1802, 2005.

[130] W. Humphrey, A. Dalke, and K. Schulten, "VMD: Visual molecular dynamics," *Journal of Molecular Graphics,* vol. 14, pp. 33-38, 1996.

[131] E. Lewars, "Pyramidane: an ab initio study of the C5H4 potential energy surface," *Journal of Molecular Structure: THEOCHEM,* vol. 423, pp. 173-188, 1998.

[132] G. Gill, D. M. Pawar, and E. A. Noe, "Conformational Study of cis-1,4-Di-tert-butylcyclohexane by Dynamic NMR Spectroscopy and Computational Methods. Observation of Chair and Twist-Boat Conformations," *The Journal of Organic Chemistry,* vol. 70, pp. 10726-10731, 2005.

[133] V. Emel'yanenko, S. Verevkin, and A. Pimerzin, "The thermodynamic properties of DL- and L-lactides," *Russian Journal of Physical Chemistry A, Focus on Chemistry,* vol. 83, pp. 2013-2021, 2009.

[134] D. E. Henton, P. Gruber, J. Lunt, and J. Randall, "Polylactic Acid Technology," in *Natural fibers, biopolymers, and biocomposites*, A. K. Mohanty, M. Misra, and L. T. Drzal, Eds. Boca Raton, FL: Taylor & Francis/CRC Press, 2005, p. 875.

[135] D. Rigby and R.-J. Roe, "Molecular dynamics simulation of polymer liquid and glass. I. Glass transition," *The Journal of Chemical Physics,* vol. 87, pp. 7285-7292, 1987.

[136] J. Zhang, J. Yan, L. Uitenham, and J. Lou, "Study of the Molecular Weight Dependence of Glass Transition Temperature for Amorphous Poly(L-Lactide) by Molecular Dynamics Simulation," in *Proceedings of the 2007 National Conference on Environmental Science and Technology*, 2009, pp. 339-344.

[137] J. R. Dorgan, J. S. Williams, and D. N. Lewis, "Melt rheology of poly(lactic acid): Entanglement and chain architecture effects," *Journal of Rheology,* vol. 43, pp. 1141-1155, 1999.

[138] H. J. Lehermeier and J. R. Dorgan, "Melt rheology of poly(lactic acid): Consequences of blending chain architectures," *Polymer Engineering & Science,* vol. 41, pp. 2172-2184, 2001.